NUMERICAL MODELING OF PLANAR PERIODIC STRUCTURES IN ELECTROMAGNETICS

THÈSE N^{O} 3688 (2006)

PRÉSENTÉE LE 8 DÉCEMBRE 2006

À LA FACULTÉ DES SCIENCES ET TECHNIQUES DE L'INGÉNIEUR

Laboratoire d'électromagnétisme et acoustique

SECTION DE GÉNIE ÉLECTRIQUE ET ÉLECTRONIQUE

ÉCOLE POLYTECHNIQUE FÉDÉRALE DE LAUSANNE

POUR L'OBTENTION DU GRADE DE DOCTEUR ÈS SCIENCES

PAR

Katarina BLAGOVIĆ

Dipl.-Ing. EE, Université de Zagreb, Croatie
de nationalité croate

acceptée sur proposition du jury:

Prof. J. R. Mosig, président du jury
Prof. A. Skrivervik Favre, directrice de thèse
Prof. J. Bartolic, rapporteur
Prof. A. Freni, rapporteur
Dr F. Rachidi-Haeri, rapporteur

ÉCOLE POLYTECHNIQUE
FÉDÉRALE DE LAUSANNE

Lausanne, EPFL
2006

Look around and chose your own ground
For long you live and high you fly
And smiles you'll give and tears you'll cry
And all you touch and all you see
Is all your life will ever be

(Pink Floyd "Breathe")

Abstract

Periodic structures, such as frequency-selective surfaces (FSSs) and photonic band-gap (PBG) materials, exhibit total reflection in specific frequency bands while total transmission in other bands. They find numerous applications in a large field of the electromagnetic (EM) spectrum. For example, in the microwave region, they are used to increase the efficiency of reflector antennas. In the far-infrared region they are used in designing polarizers, beam splitters, mirrors for improving the pumping efficiency in molecular lasers, as components of infrared sensors, etc.

To set a solid basis for the analysis of periodic structures, we have first studied the most commonly used technique, the integral equation (IE) solved by the method of moments (MoM). IE-MoM is particularly well-suited for the analysis of printed planar structures. In any IE-MoM numerical implementation the efficient evaluation of the corresponding Green's functions (GFs) is of paramount importance. This is especially true for IE analysis of periodic structures whose GFs are slowly converging infinite sums. The systematic study of existing acceleration algorithms of general and specific types, used to accelerate the evaluation of periodic GFs, has been performed. We propose a new and efficient method for acceleration of multilayered periodic GFs that successfully combines the advantages of Shanks' and Ewald's transform.

In structures operating at higher frequencies (thin films in millimeter and submillimeter wave bands or with self supporting metallic plates) the thickness of metallic screens must be taken into account. The existing full-wave approaches for simulating these structures double the number of unknowns as compared to that one of the zero-thickness case. Moreover, the thick aperture problem asks for the computation of cavity Green's functions, which is a difficult and time-consuming task for apertures of arbitrary cross-sections. This thesis addresses the problem of scattering by periodic apertures in conducting screens of finite thickness by introducing an approximate and computationally efficient formulation. This formulation consists in treating the thick aperture as an infinitely thin one and in using the correction term in integral equation kernel that accounts for the screen thickness. The number of unknowns remains the same as in the zero-thickness screens and evaluation of complicated cavity Green's functions is obviated, which yields computationally efficient routines.

Key words: numerical modeling, electromagnetics, method of moments, integral equation, periodic structures, accelerating techniques, thick screens

Zusammenfassung

Periodische Strukturen wie z. B. frequenzselektive Flächen und Materialien mit photonischen Bandlücken haben als charakteristische Eigenschaft, daß sie in bestimmten Frequenzbändern eine einfallende Welle vollständig reflektieren während sie in anderen völlig durchsichtig sind. Sie finden sich in ein einem weiten Feld von elektromagnetischen Anwendungen. Im Mikrowellenbereich zum Beispiel werden sie eingesetzt, um den Wirkungsgrad von Reflektorantennen zu verbessern. Im infraroten Frequenzbereich finden sie sich in Polarisatoren, in Strahlenteilern, als Spiegel in molekularen Lasern, um deren Pumpleistung zu verbessern, in Sensoren, usw.

Zur Simulation von periodischen Strukturen eignet sich besonders ein Ansatz, der auf Integralgleichungen und der Momentenmethode basiert. Dieser Ansatz ist vor allem für gedruckte, planare Schaltungen geeignet und wurde deshalb in einer ersten Phase genauer betrachtet. Seine effiziente Anwendung hängt sehr stark von der Berechnung der involvierten Greenschen Funktionen ab. Deren rasche Berechnung ist um so wichtiger wenn es sich um periodische Strukturen handelt, da deren Darstellung als unendliche Summe besonders langsam konvergiert. Aus diesem Grund wurde im Rahmen dieser Arbeit eine tiefergehende Studie von Verfahren zur Konvergenzbeschleunigung durchgeführt. Dabei wurden sowohl allgemeine als auch problemspezifische Verfahren betrachtet. Aus dieser Studie resultiert eine neuer, effizienter Algorithmus zur Beschleunigung von Greenschen Funktionen wie sie in mehrschichtigen, periodischen Strukturen auftreten. Er beruht auf einer Kombination der Beschleunigungsverfahren von Shanks und Ewald.

Ein weiteres Problem, das im Zusammenhang mit periodischen Strukturen auftritt, ist die endliche Dicke von metallischen Flächen. Der Einfluß der endlichen Dicke macht sich verstärkt bemerkbar für höhere Frequenzen und ist im Milli- und Mikrowellenbereich nicht mehr vernachlässigbar. Die Berücksichtigung der endlichen Dicke geht meist einher mit einer größeren Anzahl von Unbekannten in der Modellierung im Vergleich zu einem Ansatz, bei dem die Metallisierung als unendlich dünn angenommen wird. Häufig verdoppelt sich dabei deren Anzahl. In dieser Arbeit wurde ein anderer Weg gewählt: Ausgehend von einer unendlich dünnen Metallisierung wurde die endliche Dicke durch einen Korrektionsterm berücksichtigt. Dies hat den Vorteil, daß die Anzahl der Unbekannten genauso groß ist, wie im Fall einer unendlich dünnen Metallisierung und dennoch der Einfluß der endlichen Dicke berücksichtigt werden kann. Dieser Ansatz zeichnet sich besonders dadurch aus, daß die Simulationszeit im Vergleich zum Fall einer unendlich dünnen Metallfläche nur unwesentlich erhöht wird.

Schlüsselwörter: Numerische Modellierung, Elektromagnetismus, Momentenmethode, Integralgleichungen, perdiodische Strukturen, Konvergenzbeschleunigung, Metallisierungen endlicher Dicke

Version abrégée

Les structures périodiques, telles que les surfaces sélectives en fréquences et les matériaux photoniques à bande interdite, assurent une réflexion ou une transmission totale des signaux dans certaines fréquences spécifiques. Elles trouvent de nombreuses applications dans une grande partie du spectre éléctromagnétique. Elles peuvent être utilises dans les micro-ondes pour augmenter l'efficacité des réflecteurs d'une part, et d'autre part dans l'infrarouge, pour la conception de polariseurs, comme miroirs pour améliorer l'efficacité du pompage dans les lasers moléculaires, comme composant des sondes à infrarouge, etc...

Afin d'établir une base solide pour l'analyse des structures périodiques une technique fréquemment utilisée (l'équation intégrale résolue par la méthode des moments) a d'abord été étudiée. Cette technique est particuliérement bien adaptée à l'analyse des structures planaires imprimées. L'évaluation efficace des fonctions de Green correspondantes à cette structure est d'une importance capitale dans toute implémentation numérique d'équation intégrale par méthode des moments. Cela est également valable pour l'analyse des structures périodiques dont les fonctions de Green sont des sommes infinies qui convergent très lentement. L'étude systématique des algorithmes d'accélération de types généraux et spécifiques, utilisés pour accélerer l'évaluation des fonctions de Green périodiques, a été effectuée. Nous proposons une méthode nouvelle et efficace pour l'accélération des fonctions de Green périodiques des structures multicouches qui combine avec succès les avantages des transformées de Shanks et de Ewald.

Pour les structures fonctionnant aux fréquences plus élevées (couches minces dans les bandes millimétriques et submillimétriques) l'épaisseur des écrans métalliques doit être prise en compte. Les techniques d'approches connues (full wave) pour simuler de telles structures doublent le nombre d'innconues par rapport au cas d'épaisseur nulle. D'autre part, la diffraction des structures d'épaisseur finie demande le calcul des fonctions de Green pour la cavité, qui est une tâche difficile et prend beaucoup de temps quand appliquée aux ouvertures de forme quelconque. Cette thèse traite le problème de diffraction/dispersion des ouvertures périodiques dans des écrans d'épaisseur finie en présentant une formulation approximative et efficace. Cette formulation consiste à traiter l'ouverture épaisse comme une ouverture infiniment mince en appliquant un terme de correction qui prend en compte l'épaisseur de l'écran dans le noyau de l'équation intégrale. Elle permet de garder le même nombre d'inconnues que dans le cas des écrans d'épaisseur nulle et d'éviter ainsi le calcul des fonctions de Green pour la cavité. Ceci nous a conduit à l'élaboration de techniques de calcul numériques efficaces.

Mots clés: modélisation numérique, électromagnétisme, méthode des moments, équation intégrale, structures périodiques, techniques d'accéleration, écrans d'épaisseur finie

Sažetak

Periodičke strukture, kao na primjer frekvencijski selektivne površine (FSS) i fotonički materijali sa zabranjenim pojasom (PBG), totalno reflektiraju elektromagnetske valove u odredjenom frekvencijskom području, dok ih u nekom drugom području propuštaju. Ovakve strukture nalaze raznovrsne primjene u širokom elektromagnetskom spektru. Na primjer, u mikrovalnom području se koriste za povećanje učinkovitosti reflektorskih antena. U dalekom infra-crvenom području koriste se za dizajniranje polarizatora, ogledala za unapredjivanje efikasnosti pumpanja kod molekularnih lasera, komponenti infracrvenih senzora, itd.

Jedna od najčešće korištenih metoda u analizi periodičkih struktura je primjena integralnih jednadžbi (IE) koje se numerički rješavaju metodom momenata (MoM). U svakoj numeričkoj implementaciji IE-MoM metode posebno je važno efikasno i točno izračunati Greenove funkcije odgovarajuće strukture. To je osobito značajno u slučaju periodičkih struktura čije su Greenove funkcije beskonačne sporo kovergirajuće sume. U tu su svrhu proučavani postojeći algoritmi općeg i specifičnog tipa za ubrzavanje računanja Greenovih funkcija. U ovom je radu predložena nova i uspješna metoda za ubrzavanje Greenovih funkcija periodičkih struktura tiskanih na višeslojnim dielektricima koja kombinira poznate metode kao što su Shanks-ova i Ewald-ova tehnika.

Konačna debljina metalnih ravnina u strukturama koje rade na visokim frekvencijama (kao npr. tanki filmovi u milimetarskom i sub-milimetarskom valnom području) mora biti uzeta u obzir u numeričkim simulacijama i formuliranju problema. Primjena postojećih punovalnih metoda za rješavanja takvih struktura udvostručava broj nepoznanica u usporedbi sa strukturama metalnih ravnina zanemarive debljine. Štoviše, problem raspršenja od otvora u takvim ravninama zahtjeva računanje Greenovih funkcija za šupljine, što u slučaju otvora proivoljnog poprečnog presjeka postaje jako teško i vremenski zahtjevno. U ovom radu predložena je aproksimativna ali učinkovita formulacija za rješavanje problema raspršenja elektromagnetskog vala od periodickih otvora u metalnim ravninama konačne debljine. U ovom pristupu metalna ravnina konačne debljine se aproksimira beskonačno tankom ravninom, dok se stvarna debljina pojavljuje kao korekcijski faktor u jezgri integralne jednadžbe. Broj nepoznanica ostaje isti kao u slučaju beskonačno tanke ravnine i time je izbjegnuto računanje kompliciranih Greenovih funkcija za šupljine, što rezultira računalno učinkovitim algoritmima.

Ključne riječi: numeričko modeliranje, elektromagnetizam, metoda momenata, integralne jednadžbe, periodičke strukture, akceleracijske tehnike, debele ploče

Acknowledgements

In the beginning, I had the idea of simply saying that I would like to deeply thank the colleagues, professors and many friends who, in one way or another, have made my thesis and my stay in Switzerland extremely enriching experience. However, I cannot not to remember so many 'souvenirs' that I am indebted to all this people for, and therefore needed to put them down on paper.

First and foremost to my thesis advisor, I would like to thank you Anja for your warm welcome in LEMA and giving me the opportunity to do a PhD. And "côté non scientifique" I am deeply grateful for all our discussions, and precious advices concerning many different topics.

My appreciation goes to the thesis committee members for having accepted to examine my work and having provided valuable suggestions to improve the quality of this thesis: Prof. Angelo Freni from University of Florence, Dr. Farhad Rachidi from EPFL, and Prof. Juraj Bartolić from University of Zagreb. Special mention to Prof. Bartolić for all his guidance and care.

To Juan, muchas gracias por todo, for having always time for my "just 5 minutes" in your tight agenda, for the corrections of articles and for letting us discover the beauty of "Le Tas de Merde".

Huge thank goes to Eulalia, my favorite syndicaliste: without you it wouldn't have been the same. Thank you for all your *petits coups de main* that were not at all in your *cahier des charges*. In addition I would like to extend my gratitude to Mrs Alix VIP Wend. Thank you both for creating the cheerful atmosphere in the lab and for your permanent assistance in many different ways.

Once I was told the working environment makes a great deal of the working experience and thanks to the LEMA members this turns out to be true. I would like to thank you here for all the funny moments that we have had together. Veliko hvala to Ivica and vielen Dank to Michael for all your benevolence, kindness, patience, energy, encouragement, discussions and your time that you have generously shared with me. And thanks to you both for rendering this thesis a comprehensible manuscript. Without you this thesis simply would not be. And without forgetting marathonian sessions of listening my long and never ending trial of a private defense.

A particular *obrigado* to Juliane, my office mate for the past few years, for supporting me in every sense (including my mountain equipment in the office) and being so good-hearted.

A special mention goes to the linguistic committee, in alphabetical order: Grégoire, Ivica, Michael, and Olivier for their precious help in preparing the Croatian, German, and French versions of the thesis abstract.

In addition, I would like to extend my gratitude to all former and current lab members with a special mention to Eulalia, Ivica, Eugenia, Michael, Juliane, Greg (le Grand Belge), Alix (les corrections de mon français in its painful beginning), Gabriela (thanks for all the Fridays panachés in Satellite), Pablo Polyathlète, Fran, Hervé, Pedro, Frédéric, Daniel, Olivier, Stefano, Ferdinando, Jean-François... A huge LA Neige Merci goes to Delphine, Pierre-Jean, and Thomas for all the mountain related chats and for a constant support in this 'end of thesis period'. And all the others that I have not mentioned by name here, thank you.

On a more personal basis, I am profoundly indebted to many great friends that I have been lucky to meet on my way, who offered me the countless number of memories, unforgettable time we spent together, and warm care.

Huge thank you in complete alphabetical disorder: Ivica - for your excellent prijateljstvo and for all the *uprights* that you have corrected in my thesis, for always having time to discuss some serious and not at all serious topics and the Christmas and Eastern chickens. Iva - for unconditional support in many practical and less practical issues, and Marko for your particular sense of humor. Sylvia pour tous les kilomètres à pied, en vélo, en ski et quelques mètres en natation et pour tout le reste. Branimir for making me laugh, and without forgetting for the eurovision song contest evenings. Mimi for "short" hikings always supported by a top "nothing can surprise us" equipment, and lots of kms by car. Thank you Hanne, Ronan, Camillo, Goran, Allison, Sébastian, Dušan, and Beatrijs (for our female Saturday coffees) for tons of fun we have had during our petites randonnées à pied et à ski. Edina and Olivier veliko merci for excellent weekends, and for organizing so many parties, and your friendship. Mia for being close by in very critical moments. Ana and Pablo for a great time in Nepal and making me feel at home. László for his care and all the apèros in nano group that I have participated. Eugenia Cabot and Maria Barja, as well, for all the "sorties cinéma" and for always having words of encouragement for your clumsy friend. Jelena for all the compassion during my knee accident and for all the rest. Beta for being an extra neighbor and for our late coffees. And my friends on the other side of the ocean: Silvija - hvala ti neizmjerno za sve i Slaven; Libero, super je imati takvog frenda and for all the meals you have prepared; Boris and Dušan - for being my friends more than a decade and for keeping me not to forget the Sarajevski humor.

To my friends in Croatia: thank you Anita for all your care, friendship and being my older sister in every sense of this word, FER chicks Ana, Ivana and Vlatka, spiritual guru Matilda, Sanja, Katijana, Anita, Dino and Antonija, Marta and Nikola, Kristina and Kristijan and Damjan. Veliko Hvala za sve divne trenutke i prijateljstvo koje ste mi darovali.

To my friends in Sarajevo: Lejla, Amela, Mija, s. Margareta and teta Darija - warm thank you for being there when I needed you the most. Hvala od srca!

Last but not least, I would like to express my deepest thanks to my dad: for your unconditional support and love, trust you had in me and for letting me chose my way, and all our discussions and our laughs... To you I dedicate this thesis.

Table of Contents

1 Introduction

1.1 Introduction

Numerical modeling is a discipline that shows how mathematical models can be applied to study real phenomena. Depending on the application field (civil, mechanical, or electrical engineering, life sciences, etc) and the problem concerned, we encounter different methods. The Finite Element Method (FEM) can be used for modeling 3-D structures [1, 2]. The Finite Difference Time Domain (FDTD) is often used when simulating complex environments, for example when nonlinear active devices (e.g. pacemaker) are included in the simulated structures (e.g. in this case human tissue) [3]. The Integral Equations (IE) solved by Method of Moments (MoM) are particularly suitable for analysis of planar circuits in micro- and millimeter wave range [1] and therefore the best choice for modeling planar periodic structures that are in the scope of our interest.

Planar periodic structures, in particular Frequency Selective Surfaces (FSSs), Photonic Bandgap Structures (PBG) are 1-D or 2-D arrays of periodically arranged identical elements, showing filter properties with respect to frequency. For the reason of their passband, stopband and bandgap properties they are widely used in micro- and millimeter wave applications (filter design, microstrip circuits, antenna reflectors just to mention a few). A very comprehensive study completed with various and numerous examples of practical FSSs is found in Munk's book [4]. A detailed overview of the techniques for analyzing FSSs is listed in [5].

Any integral equation (IE-MoM) implementation asks for the efficient evaluation of the corresponding GFs. This is especially true for periodic structures whose GFs are doubly infinite slowly converging sums. In order to speed up the evaluation of these series specially adapted acceleration algorithms are of utmost interest.

Many radiating structures including apertures are traditionally analyzed assuming zero-thickness screens. With the apparition of new technologies and the drive for higher frequencies the thickness of metallic screens must be taken into account. There exist a number of full-wave methods that can deal with very general aperture problems but they lack the simplicity and internal coherence of the straightforward IE model (the so-called 2.5-D model) that can be used in the case of zero thickness apertures. Therefore the development of efficient approximations that can accurately deal with finite thickness screens keeping the simplicity of zero thickness approach, is of chief relevance.

This thesis addresses both of the mentioned problems.

1.1.1 Thesis Objectives

The research presented in this thesis is done in the frame of the Swiss National Science Foundation (SNSF) project: "Analysis of periodic ground plane for microwave and millimeter

wave applications".

The first step in accomplishing the project and thesis objective was to find a suitable technique for modeling periodic structures. Studying the periodic problems already solved, in literature, it turned out that the most appropriate choice was Integral Equation (IE) solved by the Method of Moments (MoM). IE-MoM approach requires reliable and accurate associated Green's Functions (GFs). Having well defined GFs for periodic problems gives rise to another problem, slow convergence of periodic GFs. This motivated the study of existing accelerating techniques of general and specific types. A new method for accelerating the multilayered periodic GFs, in particular vector potential GFs, has been proposed. It uses advantages of Shanks' transform, as a general technique, and Ewald's transform, as a specific technique.

Scattering by apertures in metallic screens is a well-known problem in electromagnetics (EM). It is mostly studied as a zero-thickness case but toward higher frequencies and new trends in technology the thickness of the screen cannot be neglected anymore. This was another objective accomplished in this work. The new suitable and efficient way to incorporate finite thickness of the screen into algorithms/equations whose complexity is in the range of zero thickness case, without increasing much the complexity and CPU time, is found.

The approximate method proposed in [6] allows for the thick aperture to be modeled as an infinitely thin one, where the screen thickness appears only as a modification in the Green's function of the problem. The correction term is computed in two ways. One way is to neglect the aperture's side walls and use the parallel plate Green's functions, whereas another one uses Ewald's transform applied to cavity Green's functions. The gain in computational time and reducing the complexity of problem formulations for the case of correction term calculated using parallel plate Green's functions, is advantageous as it obviates the time consuming computation of the cavity Green's function. The number of unknowns is same as for zero-thickness case. When higher accuracy is desired, the correction term formulated using Ewald's transform and cavity Green's functions allows screen thickness to be accounted for reducing the complexity compared to classical full-wave analysis.

1.1.2 Thesis Outline

This section summarizes the contents of the chapters of the thesis. Each chapter gives a literature overview of the problem concerned and therefore the general literature overview in this introductory chapter is omitted.

Chapter 2 provides the basic survey of numerical tools needed for modeling of planar periodic structures. It gathers and presents in an organized way numerical issues like discretization, IE-MoM procedure, calculations of reflection and transmission coefficients for planar structures. It describes image and modal formulations of periodic Green's functions for both free-space and multilayered media.

Chapter 3 gives an exhaustive explanation of general and specific algorithms used in this work. It presents the results obtained for the acceleration of 1-D sums that are of the same nature as the GFs considered in this work. The results for 2-D periodic GFs for free-space and for multilayered case are shown.

Chapter 4 presents a new method for the acceleration of multilayered periodic GFs combining Shanks' and Ewald's transforms. The method focuses on the acceleration of the vector potential multilayered GFs. It explains how the periodic sum is divided in two parts, where the dynamic is accelerated using Shanks' transform and the static part evaluated by the means of Ewald's transform. Detailed discussion of results is given.

Chapter 5 examines the problem of scattering by periodic apertures in conducting screens of finite thickness. A new approach is proposed to efficiently treat periodically perforated conducting screen of finite thickness. First, it describes how the problem is divided into two problems that can be treated separately, outer (periodic) problem and inner problem of aperture volume. Then, it introduces the two means of calculating the correction term. One, using the parallel plate GFs and the other, using Ewald's transform applied to cavity potential GFs. Finally, the chapter is completed with the results obtained for the current distribution, radiation pattern, time study and reflection/transmission coefficients.

1.1.3 Original Contributions

The original contributions of this thesis are summarized in what follows.

Chapter 3 contains contributions in terms of acceleration techniques. It is an extensive survey of readily available general algorithms and the most popular specific ones. Some contributions are given as trial of accelerating the 2-D sums transforming them in 1-D sums, study of accelerating the modal and image sums by Shanks' transform as well as practical importance in calculating the current distribution for canonical FSS cases.

Chapter 4 proposes a new method for the acceleration of multilayered periodic GFs successfully combining Shanks' and Ewald's transforms.

Chapter 5 introduces a novel method for the efficient analysis of periodic apertures in conducting screens of finite thickness. It presents two possible ways of calculating the correction term that takes into account the finite thickness of the screen.

2 Numerical Modelling of Planar Periodic Structures

The sum of an infinite series whose
final term vanishes perhaps
is infinite, perhaps finite.

(Jakob Bernoulli (1654 - 1705))

2.1 Introduction

Periodic structures, such as frequency-selective surfaces (FSSs) and photonic band-gap (PBG) materials exhibit total reflection in specific frequency bands while total transmission in other bands. They find numerous applications in a large field of the electromagnetic (EM) spectrum. In the microwave region, they are used to increase efficiency of reflector antennas, and in radome design as well. In the far-infrared region they are used in designing polarizers, beam splitters, mirrors for improving the pumping efficiency in molecular lasers, as component of infrared sensors, etc. Furthermore, in the near-infrared and visible part of spectrum they are exploited as solar selective surfaces to aid in the collection of solar energy [5]. Recently, it has been shown that periodic structures built from nonmagnetic conducting sheets can exhibit negative real parts of permittivity and permeability [7, 8]. These materials, designated as left-handed metamaterials, open new application fields.

The scattering from doubly periodic arrays of PEC objects has been simulated using source-model [9] or time-domain [10] techniques. Fully 3-D modeling capabilities of periodic structures can be achieved using finite-element (FE) methods that can cope with complicated shapes and anisotropic materials. However, the radiation into unbounded regions asks for either absorbing boundary conditions (ABCs) or perfectly matched layers (PMLs) and special measures need to be taken when employing these conditions to the scattered field formulation [11]. Therefore, hybrid finite-element/boundary integral (FE/BI) techniques that are based on FE modeling of a unit cell and BI modeling of its top and bottom faces are introduced. In these methods, the BI fields are expanded using spectral-domain Floquet modes [12] or using space-domain Green's functions (GFs) accelerated applying the Ewald transformation [13, 14]. Periodic structures are advantageously analyzed with integral-equation (IE) techniques, usually formulated in the spectral domain, as shown for instance by the case of multilayered FSSs [5]. Two approaches can be employed. One is to compute a specific FSSs in its entirety [15] and the other is to cascade the generalized scattering matrices (GSMs) of the

constitutive building blocks [16]. Recently, the boundary integral-resonant mode expansion (BI-RME), used to compute the entire-domain basis functions in conjunction with method of moments (MoM), has been applied to analysis of FSSs [17]. The scope of these IE techniques is limited to planar metallic scatterers embedded in the planes of periodicity. Moreover, the involved EM quantities are expressed as Floquet sums with a slow convergence rate [14].

In this work, we will constrain to numerical modeling of planar periodic structures, in particular frequency selective surfaces (FSS). From the point of view of mathematical and numerical modeling, one of the most convenient (suitable) approaches, for this type of structures, is the Integral Equation model combined with the Method of Moments procedure (IE-MoM). This type of modeling involves the formation of an integral equation which has as its kernel a Green's function series that converges very slowly. In using the method of moments (MoM) to discretizate and to determine the scattering or radiation from an infinite periodic structure, repeated evaluations of the Green's function series are required to fill the impedance matrix of the structure being modelled. Consequently, the computer CPU time necessary to solve the problem by the MoM is dominated by the time needed to generate slowly converging elements of the impedance matrix.

As it is apparent from the previous lines, an efficient evaluation of periodic Green's functions is indispensable in planar structures modeling using an IE technique. Free-space Green's functions are required to model self-standing planar structures (e.g. periodically perforated metallic screens), while for the modeling of periodic metallizations deposited on a dielectric substrate, the multilayered Green's functions are needed. Periodic Green's functions are apart from frequency selective surfaces (FSSs), photonic band gap structures (PBG) and antenna arrays, used in Korringa-Kohn-Rostoker (KKR) method to compute the electronic structure of solids in solid-state physics [18]. In [19] to calculate the Coulomb interaction energy of a lattice of ions. The periodic Green function plays an important role in the homogenization of artificial materials, and in the characterization of the band structures of dielectric and metallic crystals [20]. Therefore, the understanding of periodic Green's function behavior is of utmost interest.

The slow convergence is in a simple way explained by the fact that the infinite series reaches the "exact value after summing a big number of terms, which in terms of practical feasibility, is not possible. Image (spatial formulation) converges slowly close to the boundary, whereas the modal (spectral) formulation converges slowly when the observation point is close to the source. Both sums demonstrate slower convergence when are source and observer on same plane since there is no exponential term that help convergence [20].

The problem of slow convergence is solved by implementing accelerating algorithms that yields the numerical solution, within reasonable bounds, in terms of CPU time, achieving desired accuracy and robustness. This way satisfactory results are provided.

In this chapter a compact theoretical basis needed to perform efficient numerical simulations of planar periodic structures is given. First the basic survey of a generic IE procedure with geometrical discretization is explained. Then, to accomplish the periodic structures analysis the reflection and transmission coefficients of FSS are commented in details. Finally, the explication of the infinite periodic Green's function accompanied by a description of Green's function kernel of the double infinite series is given.

2.2 Numerical Recipe

Numerical modeling comprises set of steps necessary to pass from an integral equation (IE) formulation into a computer convenient form. They can be summarized as follows:

1. Discretization
   - defining the unit cell geometry and meshing the structure
   - meshing/discretization is closely related to the choice of basis functions best suited for a given structure
2. Green's function part
   - defining the Green's function for a given unit cell of periodic structure and given boundary conditions
   - choice of appropriate accelerating technique
3. Numeric part
   - MoM matrix filling and calculations of coupling integrals related to corresponding matrix elements
   - definition of an excitation vector
   - solving matrix equation
   - recovering the parameters of interest (current distributions, radiation pattern, reflection/trans etc.)

All these issues are going to be discussed in detail in the following sections.

2.2.1 Discretization

The planar periodic structures (e.g. FSS, PBG) are in standard technologies formed of metallic surfaces or as metallic screens periodically perforated with an arbitrary shaped hole (dual structures). The method that offers very flexible approach to solve surface problems is the method of moments (MoM). This method is a powerful tool widely used in various engineering communities (electrical, mechanical and civil engineering). It has been introduced in electromagnetics by Harrington [21].

Initial step in simulating a concrete periodic structure by the MoM is to define a unit cell geometry. Then, the surface S of the unit cell geometry is divided into cells (subsections). For this purpose there exist a number of freely available and powerful generic meshers, see for instance [22] website, able to provide very fine mesh to any complicated shape. However, in practice (home-made software), modeling is mostly done with rectangular and triangular elements since they provide quite satisfying approximation of the real surface Fig. 2.1.
Once the structure is being discretized, single cells, adjacent cells or group of cells Fig. 2.2 are arranged together and associated with chosen basis functions. Then the currents can

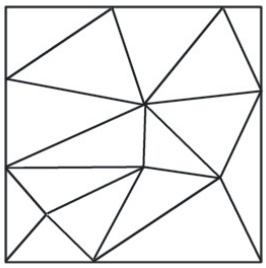

Figure 2.1: An example of meshing the square with triangular cells.

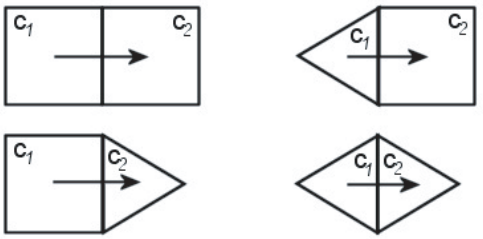

Figure 2.2: An example of joining cells for basis functions.

be approximated as a linear combination of basis functions, keeping continuity condition and locally constant charge distribution satisfied. When the currents are known, the other important parameters (reflection/transmission coefficients, radar cross section (RCS)) can be easily evaluated.

2.2.2 IE and MoM

The problem of determining the scattering or radiation from a periodic structure is expressed in terms of an IE

$$\mathcal{L}(\mathbf{a}) = \mathbf{v} \tag{2.1}$$

where the operator $\mathcal{L}$ denotes the integro-differential operations within the IE and relates the unknown surface currents $\mathbf{a}$ and the known excitation $\mathbf{v}$.

In the Method of Moments, the unknown currents are expanded as a linear combination of a set of N vector basis functions $\mathbf{f}_j$

$$\mathbf{a} = \sum_{i=1}^{N} \alpha_i \mathbf{f}_j \tag{2.2}$$

and the integral equations are tested, via an internal product, against a set of vector weight

functions $\mathbf{w}_i$. This way the integral equation (2.1) is transformed into discrete set of equations

$$\sum_{i=1}^{N} \alpha_i \langle \mathbf{w}_i, \mathcal{L}\mathbf{f}_j \rangle = \langle \mathbf{w}_i, \mathbf{v} \rangle \;\; j = 1, 2, ..., N \tag{2.3}$$

This system of linear equations (MoM system) can be written in more compact form as

$$\mathbf{ZI} = \mathbf{V} \tag{2.4}$$

where $\mathbf{Z} = [z_{ij}]_{N\times N}$ is the MoM matrix, $\mathbf{V} = [v_j]_{N\times 1}$ is the excitation vector, and $\mathbf{I} = [\alpha_i]_{N\times 1}$ denotes the unknown current coefficients.

Commonly used weight functions are Dirac delta functions ($\mathbf{w}_i = \delta(\rho - \rho_i)$) and Galerkin method ($\mathbf{w}_i = \mathbf{f}_i$) used in this work.

In case when source and observer i.e. basis and weight functions belong to the same type of sources (that is our case, since the combination of electric and magnetic currents is not used to model periodic structures), the potential Green's functions are preferred to the dyadic ones. The reason is a milder singularity of the order R^{-1} instead of R^{-3} for fields. There are two possible ways to treat singularity. It can be extracted and computed analytically [23] and added to the remaining regular part that can be computed using numerical integration. Or pass to polar coordinates, where the Jacobian of the transformation will cancel out the singularity, and the integral can be computed numerically [24, 25].

We consider a periodic structure with identical metallic objects of arbitrary shape periodically repeated in the xy plane Fig. 2.3. Let S designate the surface of the perfectly

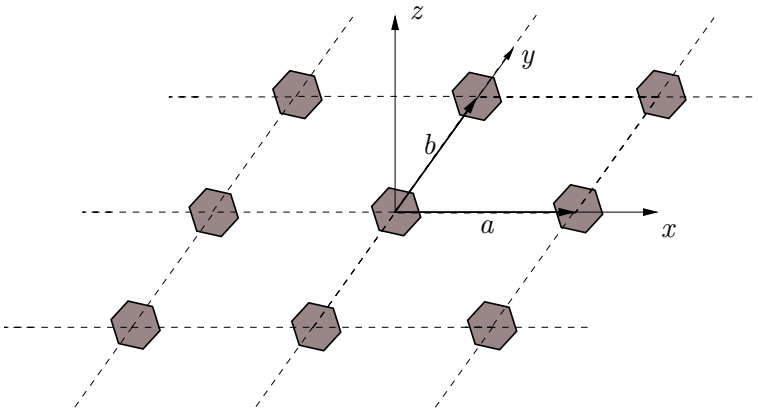

Figure 2.3: 2-D planar periodic structure with an arbitrary shaped patch as a unit cell. The periodicity in the x and y directions is given by a and b respectively.

conducting 2-D object within the structure's unit cell. The analysis is based on the solution of the following mixed potential IE (MPIE) [26]

$$-\hat{n} \times \mathbf{E}^{\mathrm{i}} = \hat{n} \times \left(-\mathrm{j}\omega \overleftrightarrow{\mathbf{G}}_A \otimes \mathbf{J} + \frac{1}{\mathrm{j}\omega} (\boldsymbol{\nabla} G_V) \otimes (\boldsymbol{\nabla}' \cdot \mathbf{J}) \right) \tag{2.5}$$

obtained by enforcing the boundary conditions (BCs) on the PEC surface S. In (2.5), $\mathbf{E}^{\mathrm{i}}$ is the incident electric field, $\hat{n}$ is the outside normal to S, $\mathbf{J}$ is the unknown current density on S, and $\overleftrightarrow{\mathbf{G}}_A$ and G_V are the vector and scalar potential GFs that take into account the periodicity of the problem. Finally, $\otimes$ is a shorthand notation [27] of the surface convolution integral

$$\overleftrightarrow{\mathbf{G}} \otimes \mathbf{J} = \int_{S'} \overleftrightarrow{\mathbf{G}}(\mathbf{r}|\mathbf{r}') \cdot \mathbf{J}(\mathbf{r}') \, \mathrm{d}S'$$

where primed and unprimed coordinates designate source and observer positions, respectively. Equation (2.5) is solved by applying the MoM in the Galerkin form. The unknown current density $\mathbf{J}$ is expanded using a set of N RWG [28] basis functions $\mathbf{f}_k$ defined on triangular subdomains S_k of the surface S

$$\mathbf{J} = \sum_{k=1}^{N} \alpha_{Ek} \mathbf{f}_k \tag{2.6}$$

where α_{Ek} are the unknown coefficients. By substituting (2.6) into (2.5) and testing the IEs by the same set of basis functions $\mathbf{f}_k$, for each frequency ω, the following system of linear equations is obtained

$$\sum_{k=1}^{N} (a_{i,k} + v_{i,k}) \alpha_{Ek} = e_k \tag{2.7}$$

where for $i, k = 1, \ldots, N$

$$e_k = \int_S \mathbf{E}^{\mathrm{i}}(\mathbf{r}) \cdot \mathbf{f}_k(\mathbf{r}) \, \mathrm{d}S = \left\langle \mathbf{E}^{\mathrm{i}}, \mathbf{f}_k \right\rangle,$$

$$a_{i,k} = \mathrm{j}\omega \left\langle \mathbf{f}_i, \overleftrightarrow{\mathbf{G}}_A \otimes \mathbf{f}_k \right\rangle, \; v_{i,k} = \frac{1}{\mathrm{j}\omega} \left\langle \boldsymbol{\nabla} \cdot \mathbf{f}_i, G_V \otimes (\boldsymbol{\nabla}' \cdot \mathbf{f}_k) \right\rangle.$$

2.3 Reflection and Transmission Coefficients of a Periodic Structure

A knowledge of the reflection/transmission coefficients of periodic structures (FSS, PBG) is of paramount importance for design of any kind of devices where this type of structures are involved.

In works of Chen [29–32], detailed explanations how to evaluate reflection coefficient of array of conducting plates, and transmission coefficient of complementary structures i.e. conducting screen periodically perforated with apertures Fig. 2.4, can be found.

The numerical procedure is to expand electromagnetic field distribution near the array of the conducting plates into a set of Floquet mode functions. By requiring the total electric field to vanish on the conducting plates, an integral equation for the unknown current on each plate is obtained. To solve this integral equation the unknown current is first expressed by a complete set of orthonormal mode functions and then its mode coefficients are determined by the MoM [31].

Infinitely thin screen, in practice means, a PEC with a thickness typically less than $\lambda/1000$.

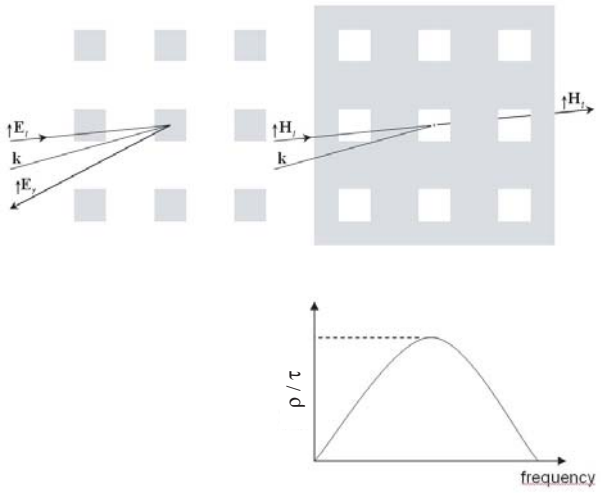

Figure 2.4: Reflection and transmission coefficients for a periodic structure.

For greater dimensions, thickness of the screen cannot be neglected. We will treat this problem in chapter where an efficient approximate technique for solving periodic slots of finite thickness will be introduced.

The components of the total EM field transverse to the propagation direction can be expanded in any plane z of the periodic structure using the transverse vector eigenfunctions, designated as Floquet modes ($\mathbf{e}_{tq}$, $\mathbf{h}_{tq}$) as [33, 34]

$$\mathbf{E} = \sum_q \left(a_q \mathrm{e}^{-\gamma_q z} + b_q \mathrm{e}^{\gamma_q z}\right) \sqrt{Z_q}\mathbf{e}_{tq} \tag{2.8a}$$

$$\mathbf{H} = \sum_q (a_q \mathrm{e}^{-\gamma_q z} - b_q \mathrm{e}^{\gamma_q z})/\sqrt{Z_q}\mathbf{h}_{tq} \tag{2.8b}$$

where q goes through all the $\mathrm{TE}_{m,n}$ and $\mathrm{TM}_{m,n}$ modes, a_q and b_q are the power coefficients of the modes propagating in the positive and negative z-directions, respectively, γ_q is the propagation constant, and Z_q the characteristic impedance of the qth mode given by

$$Z_q = \begin{cases} \frac{\mathrm{j}\omega\mu}{\gamma_q}, & \text{for TE mode} \\ \frac{\gamma_q}{\mathrm{j}\omega\varepsilon}, & \text{for TM mode} \end{cases}$$

In the case of oblique incidence ($\theta \neq 0$), an arbitrary polarized incident plane wave can be expressed as a combination of the two fundamental Floquet modes, namely TE_{00} and TM_{00}, while in the case of normal incidence ($\theta = 0$), the incident plane wave is the Floquet TEM mode [29].

Suppose that the incident plane wave impinging from below corresponds to the pth Floquet

mode, the transverse component of the electric field of this wave can be expressed as

$$\mathbf{E}^{\mathrm{i}} = a_p^{\mathrm{i}} \mathrm{e}^{-\gamma_p z} \sqrt{Z_p} \mathbf{e}_{\mathrm{t}p}. \tag{2.9}$$

Let S_{r} be a unit surface in the $z = z_{\mathrm{r}}$ plane for which the reflection coefficient is being computed, and let S_{t} be the surface in the $z = z_{\mathrm{t}} \geq z_{\mathrm{r}}$ plane for which the transmission coefficient is sought for. The total electric field in S_{r} consists of the incident field travelling in the positive z-direction and the field scattered from the metallic objects travelling in the negative z-direction, and its transverse component can be expressed as

$$\mathbf{E}(z = z_{\mathrm{r}}) = a_p^{\mathrm{i}} \mathrm{e}^{-\gamma_p z_{\mathrm{r}}} \sqrt{Z_p} \mathbf{e}_{\mathrm{t}p} + \mathbf{E}^{\mathrm{r}}. \tag{2.10}$$

This field can be expanded into Floquet modes using (2.8a)

$$\mathbf{E}(z = z_{\mathrm{r}}) = \sum_q \left(a_q \mathrm{e}^{-\gamma_q z_{\mathrm{r}}} + b_q \mathrm{e}^{\gamma_q z_{\mathrm{r}}} \right) \sqrt{Z_q} \mathbf{e}_{\mathrm{t}q}. \tag{2.11}$$

Multiplying both equations (2.10) and (2.11) by $\mathbf{e}_{\mathrm{t}p}^*$, integrating over the surface of the unit cell S_{r}, and using the orthonormal property of the Floquet modes $\int\limits_{S_{\mathrm{r}}} \mathbf{e}_{\mathrm{t}q} \cdot \mathbf{e}_{\mathrm{t}p}^* \, \mathrm{d}S = \delta_{pq}$, the reflection coefficient of the pth mode can be expressed in terms of the reflected field as follows:

$$\rho = \frac{b_p}{a_p^{\mathrm{i}}} = \frac{\mathrm{e}^{-\gamma_p z_{\mathrm{r}}}}{a_p^{\mathrm{i}} \sqrt{Z_p}} \int\limits_{S_{\mathrm{r}}} \mathbf{E}^{\mathrm{r}} \cdot \mathbf{e}_{\mathrm{t}p}^* \, \mathrm{d}S. \tag{2.12}$$

In the same manner we obtain the transmission coefficient. The total electric field in S_{t} consists of the incident electric field and the scattered field $\mathbf{E}^{\mathrm{t}}$ both propagating in the positive z-direction

$$\mathbf{E}(z = z_{\mathrm{t}}) = a_p^{\mathrm{i}} \mathrm{e}^{-\gamma_p z_{\mathrm{t}}} \sqrt{Z_p} \mathbf{e}_{\mathrm{t}p} + \mathbf{E}^{\mathrm{t}}. \tag{2.13}$$

In $z > z_{\mathrm{t}}$ there are only waves propagating in the positive z-direction, so the expansion of the total electric field can be expressed as

$$\mathbf{E}(z = z_{\mathrm{t}}) = \sum_q a_q \mathrm{e}^{-\gamma_q z_{\mathrm{t}}} \sqrt{Z_q} \mathbf{e}_{\mathrm{t}q}. \tag{2.14}$$

Multiplying equations (2.13) and (2.14) by $\mathbf{e}_{\mathrm{t}p}^*$, integrating over S_{t} and taking into account the orthonormality of the Floquet modes, for the transmission coefficient one obtains

$$\tau = \frac{a_p}{a_p^{\mathrm{i}}} = 1 + \frac{\mathrm{e}^{\gamma_p z_{\mathrm{t}}}}{a_p^{\mathrm{i}} \sqrt{Z_p}} \int\limits_{S_{\mathrm{t}}} \mathbf{E}^{\mathrm{t}} \cdot \mathbf{e}_{\mathrm{t}p}^* \, \mathrm{d}S. \tag{2.15}$$

The transverse component of the scattered electric field can be expressed as a convolution

integral of induced electric currents and the corresponding GF as:

$$\mathbf{E} = \int_{S'} \overleftrightarrow{\mathbf{G}}_{EE}(\mathbf{r}|\mathbf{r}') \cdot \mathbf{J}(\mathbf{r}')\,\mathrm{d}S'. \tag{2.16a}$$

The dyadic $\overleftrightarrow{\mathbf{G}}_{EE}$ relates the electric current density to the transverse electric field and is given by

$$\overleftrightarrow{\mathbf{G}}_{EE}(\mathbf{r}|\mathbf{r}') = \sum_q \widetilde{V}_q(z,z')\mathbf{e}_{\mathrm{t}q}(x,y) \cdot \mathbf{e}^*_{\mathrm{t}q}(x',y') \tag{2.16b}$$

The spectral domain quantity $\widetilde{V}_q$ represents the voltage at the point z along the equivalent transmission line for a unitary value of the current generator placed at $z = z'$:

$$\widetilde{V}_q(z,z') = \frac{Z_q}{2}\mathrm{e}^{-\gamma_q|z-z'|}. \tag{2.16c}$$

Finally, once the unknowns α_{Ek} have been computed by solving the MoM system of equations (2.7), using the orthonormality of the Floquet modes and equations (2.6) and (2.16), the reflection and transmission coefficients of any Floquet mode can be found as

$$\rho = \frac{\sqrt{Z_p}\mathrm{e}^{-\gamma_p z_{\mathrm{r}}}}{2a_p^{\mathrm{i}}} \times \sum_k \alpha_{Ek} \int_{S_k} \mathrm{e}^{-\gamma_p|z_{\mathrm{r}}-z'|}\mathbf{f}_k(x',y',z') \cdot \mathbf{e}^*_{\mathrm{t}p}(x',y')\,\mathrm{d}S' \tag{2.17a}$$

$$\tau = 1 + \frac{\sqrt{Z_p}\mathrm{e}^{\gamma_p z_{\mathrm{t}}}}{2a_p^{\mathrm{i}}} \times \sum_k \alpha_{Ek} \int_{S_k} \mathrm{e}^{-\gamma_p|z_{\mathrm{t}}-z'|}\mathbf{f}_k(x',y',z') \cdot \mathbf{e}^*_{\mathrm{t}p}(x',y')\,\mathrm{d}S'. \tag{2.17b}$$

In the case of a periodic structure with identical planar apertures of arbitrary shape periodically perforated in the $z = 0$ plane, the reflection and transmission coefficients are computed as shown in [35].

2.4 Green's function for 2-D periodic structures

Consider a planar structure of identical elements periodically repeated in a plane $z = \mathrm{const}$(see Fig. 2.3. Distances a and b between the centers of two neighboring cells, in x and y directions, respectively, define the periodicity lattice. Just to note that all the definitions and mathematical derivations that we perform is for orthogonal lattice.
Suppose that the unit cell of the structure located at the origin $(0,0)$, without loss of generality, is illuminated by an incident plane wave, impinging with the incident angles θ_{i} and φ_{i},

as depicted in Fig. 2.5. The plane wave propagation vector is defined as

$$\mathbf{k} = k\sin\theta_{\mathrm{i}}\cos\varphi_{\mathrm{i}}\hat{x} + k\sin\theta_{\mathrm{i}}\sin\varphi_{\mathrm{i}}\hat{y} + k\cos\theta_{\mathrm{i}}\hat{z} = k_x^{\mathrm{i}}\hat{x} + k_y^{\mathrm{i}}\hat{y} + k_z^{\mathrm{i}}\hat{z}.$$

Here $\mathbf{k}$ is as shown in Fig. 2.5 plane wave impinging from below. All the elements in the

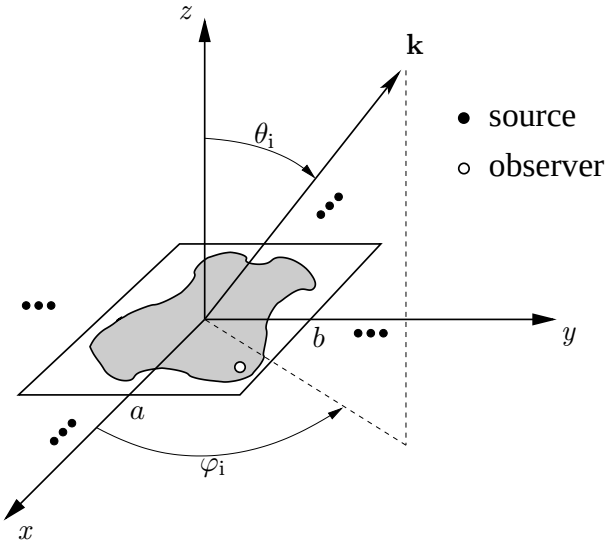

Figure 2.5: Unit cell of periodic structure; periodicity given by a and b; angles of incidence given by θ_{i} and φ_{i}.

periodic structure are equal (to the unit cell) and find themselves in the same environment. The plane wave impinging on them is the same save for the phase shift. This means that any EM quantity of interest (surface current distribution, radiated electric field,...) known for the unit cell and given by the function

$$f_0(x, y, z)$$

will be known over the entire plane as

$$f(x, y, z) = \sum_{m,n=-\infty}^{\infty} f_0(x - ma, y - nb, z)\mathrm{e}^{-\mathrm{j}k_x^{\mathrm{i}}ma}\mathrm{e}^{-\mathrm{j}k_y^{\mathrm{i}}nb}.$$

2.4.1 Image (Spatial) Formulation

Continuing the same reasoning, if $f_0(x, y, z)$ is assumed to be free-space Green's function or the Green's function in multilayered media without periodic boundary conditions, than the periodic Green's function is given by $f(x, y, z)$. This expression is a sum of images where the kernel of the series, Green's function, is given in spatial domain. In other terms, if $\mathbf{G}_0$ represents the free-space Green's function or the Green's function in multilayered media, the

Green's function of a periodic structure can be written as

$$G = G(x-x', y-y', z-z') = \sum_{m,n} G_0(x-x'-ma, y-y'-nb, z-z')\mathrm{e}^{-\mathrm{j}k_x^{\mathrm{i}}ma}\mathrm{e}^{-\mathrm{j}k_y^{\mathrm{i}}nb} \quad (2.18)$$

where in free-space the Green's function is given by

$$G_0 = \frac{1}{4\pi}\frac{\mathrm{e}^{-\mathrm{j}kR}}{R} \quad (2.19)$$

with

$$R = \sqrt{(x-x')^2 + (y-y')^2 + (z-z')^2}$$

and required Green's functions, in periodic structures modeling via Mixed Potential Integral Equation (MPIE), are $G_V = G_0/\varepsilon_0$ and $\overleftrightarrow{\mathbf{G}}_A = \mu_0 G_0 \overleftrightarrow{\mathbf{I}}$ for electric scalar and magnetic vector potentials, and $G_W = G_0/\mu_0$ and $\overleftrightarrow{\mathbf{G}}_F = \varepsilon_0 G_0 \overleftrightarrow{\mathbf{I}}$ for magnetic scalar and electric vector potentials, respectively, where $\overleftrightarrow{\mathbf{I}} = \hat{x}\hat{x} + \hat{y}\hat{y}$.

2.4.2 Modal (Spectral) Formulation

Use of Poisson 2-D summation formula [36] allows to transform the sum of images (2.19) into modal sums where the kernel of the series becomes the spectral Green's function:

$$\sum_{m,n} G(x-ma, y-nb) = \frac{1}{ab}\sum_{m,n} \widetilde{G}\left(\frac{2m\pi}{a}, \frac{2n\pi}{b}\right)\mathrm{e}^{\mathrm{j}\frac{2m\pi x}{a}}\mathrm{e}^{\mathrm{j}\frac{2n\pi y}{b}} \quad (2.20)$$

where $\widetilde{G}(k_x) = \mathcal{F}\{G(x)\}$, and taking into account Fourier transform properties

$$\mathcal{F}\left\{G(x)\mathrm{e}^{\mathrm{j}k_0 x}\right\} = \widetilde{G}(k_x - k_0) \quad (2.21)$$

(2.18) becomes

$$\begin{aligned} G &= \sum_{m,n} G_0(x-x'-ma, y-y'-nb, z-z')\mathrm{e}^{-\mathrm{j}k_x^{\mathrm{i}}ma}\mathrm{e}^{-\mathrm{j}k_y^{\mathrm{i}}nb} \\ &= \mathrm{e}^{-\mathrm{j}k_x^{\mathrm{i}}(x-x')}\mathrm{e}^{-\mathrm{j}k_y^{\mathrm{i}}(y-y')}\sum_{m,n} G_0(x-x'-ma, y-y'-nb, z-z')\mathrm{e}^{+\mathrm{j}k_x^{\mathrm{i}}(x-x'-ma)}\mathrm{e}^{+\mathrm{j}k_y^{\mathrm{i}}(y-y'-nb)} \\ &= \frac{1}{ab}\mathrm{e}^{-\mathrm{j}k_x^{\mathrm{i}}(x-x')}\mathrm{e}^{-\mathrm{j}k_y^{\mathrm{i}}(y-y')}\sum_{m,n} \widetilde{G}_0\left(\frac{2m\pi}{a} - k_x^{\mathrm{i}}, \frac{2n\pi}{b} - k_y^{\mathrm{i}}, z-z'\right)\mathrm{e}^{\mathrm{j}\frac{2m\pi}{a}(x-x')}\mathrm{e}^{\mathrm{j}\frac{2n\pi}{b}(y-y')} \end{aligned} \quad (2.22)$$

Therefore the modal sums can be written in following form

$$G = \frac{1}{ab}\sum_{m,n} \widetilde{G}_0(k_{xm}, k_{yn}, z-z')\mathrm{e}^{\mathrm{j}k_{xm}(x-x')}\mathrm{e}^{\mathrm{j}k_{yn}(y-y')} \quad (2.23)$$

where

$$k_{xm} = \frac{2m\pi}{a} - k_x^{\mathrm{i}}, \qquad k_{yn} = \frac{2n\pi}{b} - k_y^{\mathrm{i}} \tag{2.24}$$

and

$$\widetilde{G}(k_x, k_y, z - z') = \mathcal{F}\left\{G(x - x', y - y', z - z')\right\}$$

So finally, for the free-space scalar and vector potentials, the spectral Green's function is given by

$$\widetilde{\mathbf{G}}_0 = \frac{\mathrm{e}^{-\gamma|z-z'|}}{2\gamma} \tag{2.25}$$

where

$$\gamma = \sqrt{k_x^2 + k_y^2 - k^2}.$$

2.4.3 Green's Functions for Planar Multilayered Structures

The Green's function formulations explained in the two previous subsection will do for a free-space case, i.e. for any type of planar self-standing structures, periodically perforated ground planes etc.. It is often the case that the periodic metallizations are printed on a dielectric substrate and therefore it is required to replace the kernel of the series (2.18) and (2.23) by multilayered Green's functions in spatial and spectral domain, respectively.

The study of Green's functions associated to sources embedded in a planar multilayered media can be optimally done by solving an equivalent transmission line problem [27, 37](Fig. 2.6). The source becomes a lumped generator and every dielectric layer corresponds to a transmission line section. The terminal impedance walls bounding the planar multilayered medium correspond to loading impedances. Solutions of the equivalent transmission line model will provide the voltages and currents at any z-level and thus allow a full solution of the original electromagnetic problem. In particular, voltages and currents at the connection points between transmission line sections give the fields and the potentials at the interfaces of the layered medium. Table 2.1 summarize the expressions that relate spectral domain potential Green's function components with voltages and currents in the equivalent transmission line model. In this table, the primed variables designate the source, and the non-primed – the observer, k_z is the propagation constant in the z-direction, $k_\rho^2 = k_0^2\mu_r\varepsilon_r - k_z^2 = k_x^2 + k_y^2$ is the transverse spectral variable, and the characteristic impedances for the TE and TM modes are given by, respectively,

$$Z_{\mathrm{c}}^{\mathrm{TE}} = \frac{\omega\mu_0\mu_r}{k_z} \text{ and } Z_{\mathrm{c}}^{\mathrm{TM}} = \frac{k_z}{\omega\varepsilon_0\varepsilon_r}.$$

Note also that a transversal electric source J_ρ and a normal magnetic source correspond to the parallel current generator of $I_{\mathrm{g}} = 1/(2\pi)$, while a transversal magnetic source M_ρ and a normal electric source correspond to the series voltage generator with $V_{\mathrm{g}} = 1/(2\pi)$, for laterally unbounded planar multilayered structures, whereas for the case of periodic structures bounded media corresponding values are equal 1 [25]. The vector and scalar potential Green's function components, for electric and magnetic sources are given in (Table 2.1) [38, 39]. The spectral transform is a function of the spectral radial distance $k_\rho = \sqrt{k_x^2 + k_y^2}$ and is related to

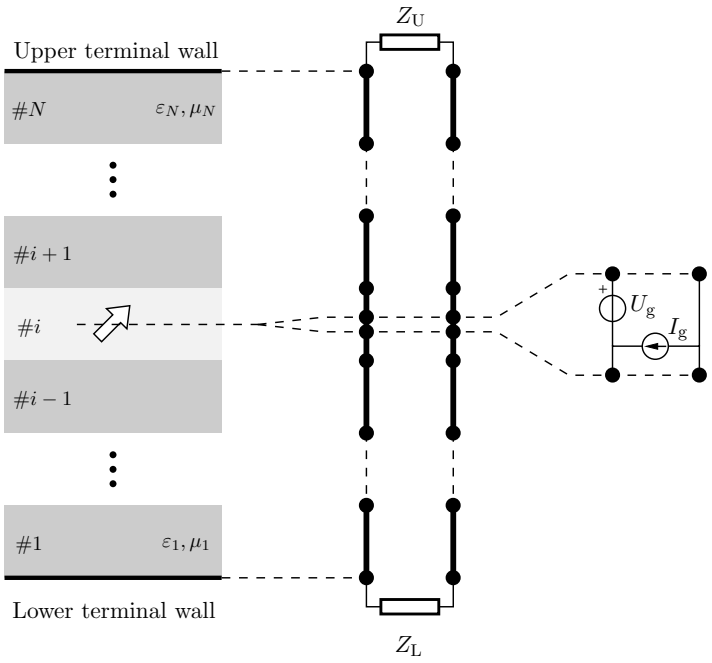

Figure 2.6: Equivalent transmission line model of the Green's function problem [37].

Electric Source	Magnetic Source
$\widetilde{G}_A^{xx} = \frac{1}{\mathrm{j}\omega} V_{J_\rho}^{\mathrm{TE}}$	$\widetilde{G}_F^{xx} = \frac{1}{\mathrm{j}\omega} I_{M_\rho}^{\mathrm{TM}}$
$\widetilde{G}_A^{yy} = \frac{1}{\mathrm{j}\omega} V_{J_\rho}^{\mathrm{TE}}$	$\widetilde{G}_F^{xx} = \frac{1}{\mathrm{j}\omega} I_{M_\rho}^{\mathrm{TM}}$
$\widetilde{G}_V = -\frac{\mathrm{j}\omega}{k_\rho^2}\left(V_{J_\rho}^{\mathrm{TE}} - V_{J_\rho}^{\mathrm{TM}}\right)$	$\widetilde{G}_W = \frac{\mathrm{j}\omega}{k_\rho^2}\left(I_{M_\rho}^{\mathrm{TE}} - I_{M_\rho}^{\mathrm{TM}}\right)$

Table 2.1: Analytical expressions of the potential Green's function components in a planar multi-layered medium in terms of currents and voltages in the equivalent transmission lines.

its spatial counter-part that is a function of a radial distance $\rho = \sqrt{(x-x')^2 + (y-y')^2}$ via 2-D Fourier transformation as a Hankel (Fourier-Bessel) transformation, also called Sommerfeld integral [27]

$$G(\rho, z, z') = \mathcal{S}_n\left\{\widetilde{G}(k_\rho, z, z')\right\} = \\ = \int_0^\infty J_n(k_\rho \rho) k_\rho^{n+1} \widetilde{G}(k_\rho, z, z')\,\mathrm{d}k_\rho \tag{2.26}$$

where J_n is the Bessel function of order n and $\widetilde{G}$ is a generic Green's function depending

on the variable $k_\rho = \sqrt{k_x^2 + k_y^2}$ and the vertical positions of the observer (z) and source (z') points. The numerical evaluation of Sommerfeld integrals can be efficiently performed using specially tailored algorithms [27].

2.5 Summary

In this introductory chapter, a brief outline of all the necessary steps to be performed in an IE-MoM analysis of planar periodic structures has been presented.

The chapter discusses all theoretical issues necessary to understand the periodic problems. The problems of the structure's discretizations are commented in addition to the numerical approach for the simulation of the periodic structures - the MoM. The theory of Green's functions for the free-space case and for the multilayered media is explained. The detailed calculations of the reflection and transmission coefficients for the periodic structures, important for the analysis and design of concrete devices are elaborated.

To summarize, the chapter gives a survey of the basis of tools that will be used in the chapters that follow to study and model planar periodic structures.

3 Acceleration techniques

3.1 Acceleration Techniques

3.1.1 Introduction

The integral equation (IE) approach asks for reliable and stable periodic Green's function. To keep the computation time within acceptable limits and provide accurate solutions one is ultimately bound to use of accelerating algorithms.

Since every series has its own nature, e.g. monotonic, oscillatory, alternating etc., it is obvious that there is no universal algorithm that can be efficiently applied to any type of series. Furthermore, that means that every concrete problem under consideration needs a special research to obtain the optimal result. The basic principle of accelerating algorithms is to transform a slowly converging series, by using a linear or nonlinear mapping, to a new, faster converging one [40]. A short, simplified explanation of the convergence problem principle will be stressed in the following lines.

Since the partial sums of an infinite series are used in most of the transformation methods, a short definition will be given. Let S_n be a partial sum of terms s_n, and let S be its limit when n tends to infinity.

$$S_n = \sum_{i=0}^{n} s_i \quad \text{and} \quad \lim_{n\to\infty} S_n = S \tag{3.1}$$

The main purpose of any accelerating technique is to try to predict what will be the partial sum S_n behavior, based on the knowledge of a few numbers of the first s_n terms [41]. That means that an extrapolation of the behavior of the partial sums to infinity must be found under the form of a limit S and some functions which take into account the behavior of S_n [42]. Let

$$S_n = S + b_1 \cdot g_1(n) + ... + b_k \cdot g_k(n). \tag{3.2}$$

If this representation is exact, the limit S of the partial sums S_n is independent of the set of S_n values used to compute it. If this is not true, the found limit depends on the set of S_n used values. In the case of divergent series, a limit S of the form of (3.2) can also be found by this way, i.e. can be proved that it has no limit. Evidentally, this limit does not represent the true limit of the series, because, indeed, this limit can be infinity if the series is unbounded, or the series can oscillate until infinity but still remain bounded. In this case, the value S found is called the anti-limit of the partial sums S_n. This concept of anti-limit allows us to compute some values of the infinite periodic Green's functions in the lossless case, such that the partial sums are not formally convergent in the sense that the sums have the true limit S. A determinant expression is usually used to find the limit or the anti-limit S [41].

In general, all the acceleration techniques may be divided into two main groups: general

algorithms and specific algorithms. The first group can be applied to any sequence (partial sum) which can be obtained from an infinite series or an infinite oscillatory integral, whereas the latter demands the analytical transform of the kernel of the series or of the integral to be performed. Both types of algorithms used in this work will be explained in details in the following sections.

By selecting the functions $g_i(n)$ we can find Shanks' transform, Levin's algorithm, the ϱ algorithm and numerous other algorithms of general type; while some others, e.g. Toeplitz-Chebyshev algorithm for instance, cannot be represented in the same way, since it belongs to a low-pass filter transformation more than to a real acceleration transform.

One of the most remarkable characteristics of general type of accelerating techniques, that are recursive algorithms as well, is that in every step the difference of two successive partial sums appears as denominator in fraction like in Shanks' algorithm [42], for example:

$$\varepsilon_{s+1}(S_n) = \varepsilon_{s-1}(S_{n+1}) + \frac{1}{\varepsilon_s(S_{n+1}) - \varepsilon_s(S_n)} \tag{3.3}$$

where

$$\varepsilon_0(S_n) = S_n \qquad \varepsilon_s(S_n) = \frac{1}{\varepsilon_0(S_{n+1}) - \varepsilon_0(S_n)} \qquad \text{for} \quad s = 1, 2, ... \tag{3.4}$$

This has as a consequence certain sensitivity of the listed algorithms to the numerical noise which is always present in the partial sums value obtained by a numerical process. This means that if some "noise" is already included in a unit cell's (single element) Green's function, the accelerating process will be significantly weakened. Indeed, summing up the noise up to ∞ will successively add its contributions result in a noisy approximation of the total sum. Or, in the worst case scenario, the algorithm can be so sensitive to the noise that the whole acceleration procedure breaks down.

One of common characteristics of accelerating algorithms is that the more the partial sums oscillate, the faster the convergence is. That is why some algorithms work very well for the alternating series that are met in waveguide theory, for example. Also there are some kind of series that cannot be accelerated by any means. Fortunately, the periodic Green's functions do not belong to this type of series.

In this chapter the different type of accelerating algorithms are examined, combined with different ways of summing. First the algorithms which belong to the general group are presented: Shanks', Chebyshev-Toeplitz, ρ, θ, Levin's t-transform. The second group belongs to the type of specific algorithms that cannot be applied to the sequence in a straightforward manner, but demand an analytical transform to be performed on the kernel of the series.

This chapter is organized as follows. In the first part, we give an overview of accelerating algorithms used to speed up Green's function evaluation - general and specific algorithms.

- General algorithms $\sim$ Shanks'transform, ρ algorithm, θ algorithm, Levin's t algorithm and Chebyshev-Toeplitz algorithm

- Specific algorithms $\sim$ Summation by Parts algorithm, Kummer's transformation, Poisson's summation formula and Ewald's transform

Next, we present these algorithms to evaluate both free-space GFs and multilayered GFs,

and compare their efficiency. Finally, the new method for accelerating the periodic GFs for multilayered case, based on the successful combination of Shanks' and Ewald's transform is presented.

3.1.2 General algorithms

Shanks' algorithm

Shanks' transform is among the best known sequence transformations that might be used to accelerate many series arising in practical physical problems. Based on the assumption that the partial sums S_n of a sequence can be treated as a mathematical transient, it gives an approximation of the base of the transient, which is the result of the infinite summation. It has been studied from the practical point of application in evaluations of periodic Green's function's [43], in addition to the mathematical point of interest [42]. The simplest form of the algorithm is Aitken's Δ^2 process that can be considered as the second order Shanks' transform. Its description is omitted since it was not implemented in any of study in this work and more details of it can be found in [25, 42]. We will present here the more elaborated form of the Shanks' algorithm designated as Wynn's ε algorithm [42]. Successive iterations are constructed with the rule given below:

$$\begin{aligned} &\varepsilon_{k+1}^{n} = \varepsilon_{k-1}^{n+1} + \tfrac{1}{\varepsilon_k^{n+1} - \varepsilon_k^n} && n,k = 0,1,2\ldots, \\ &\varepsilon_{-1}^{n} = 0,\ \varepsilon_0^n = S_n && n = 0,1,2\ldots, \\ &\varepsilon_k(S) = \varepsilon_{2k}^{(n)} \end{aligned} \tag{3.5}$$

Only the even-order terms $e_{2k}(S_n)$ are the true estimates of the infinite sum, while the odd-order terms $e_{2k-1}(S_n)$ are intermediate quantities and not used in sum's estimation. The advantage of Wynn's ε algorithm is that the evaluation of the determinant is reduced to a simple iterative equation [42, 44]. On the other hand, the algorithm has the drawback that it may suffer from round-off errors. In fact the values, $e_k(S_{n+1})$ and $e_k(S_n)$, that appear in two consecutive estimations are very similar and therefore as the transformation converges to the right sum, are the origin of cancelling errors. Note that this occurs in case when higher accuracy is desired. To improve numerical stability and precision step further is implementation of the cross rule of the ε algorithm also developed by Wynn [42]. The idea behind is to avoid the odd iterations, since they represent only intermediate quantities, and compute only the even-order terms. The derivation of the cross rule is simplified by using the following relation between the successive sum estimates [25]:

$$\left[\varepsilon_{2k+2}^{n} - \varepsilon_{2k}^{n+1}\right]^{-1} + \left[\varepsilon_{2k-2}^{n+2} - \varepsilon_{2k}^{n+1}\right]^{-1} = \left[\varepsilon_{2k}^{n+2} - \varepsilon_{2k}^{n+1}\right]^{-1} + \left[\varepsilon_{2k}^{n} - \varepsilon_{2k}^{n+1}\right]^{-1}. \tag{3.6}$$

After few simple algebraic transformations, the new form of the (3.6) can be written as:

$$\varepsilon_{2k+2}^{n} = \varepsilon_{2k}^{n+1} + \left\{[\varepsilon_{2k}^{n+2} - \varepsilon_{2k}^{n+1}]^{-1} + [\varepsilon_{2k}^{n} - \varepsilon_{2k}^{n+1}]^{-1} - [\varepsilon_{2k-2}^{n+2} - \varepsilon_{2k}^{n+1}]^{-1}\right\}^{-1},\ n,k = 0,1,2\ldots \tag{3.7}$$

with the following initial conditions

$$\varepsilon_0^{(n)} = S_n,\ \varepsilon_{-2}^{(n)} = \infty,\ n = 0, 1, \dots\ . \tag{3.8}$$

ρ algorithm

Let S_n be the partial sum of n terms of a series such that $S_n \longrightarrow S$ as $n \longrightarrow \infty$, where S is the sum of the series. The ρ algorithm can be computed as follows [45]:

$$\rho_k^{(n)} = \rho_{k-2}^{(n+1)} + \frac{k}{[\rho_{k-1}^{(n+1)} - \rho_{k-1}^{(n)}]},\ k = 1, 2, \dots\ , \tag{3.9}$$

where

$$\rho_{-1}^{(n)} = 0,\ \rho_0^{(n)} = S_n. \tag{3.10}$$

and k is the order of the algorithm. The even order terms, ρ_{2k}^n, give estimates of S whereas the odd order terms, ρ_{2k+1}^n, are only intermediate quantities.

θ algorithm

Let S_n be the partial sum of n terms of a series such that $S_n \longrightarrow S$ as $n \longrightarrow \infty$, where S is the sum of the series. The θ algorithm can be computed as follows with the even order terms given by [46]:

$$\theta_{2k+2}^{(n)} = \theta_{2k}^{(n+1)} + \frac{[\theta_{2k}^{(n+2)} - \theta_{2k}^{(n+1)}][\theta_{2k+1}^{(n+2)} - \theta_{2k+1}^{(n+1)}]}{[\theta_{2k+1}^{(n+2)} - 2\theta_{2k+1}^{(n+1)} + \theta_{2k+1}^{(n)}]},\ k = 0, 1, 2, \dots\ , \tag{3.11}$$

and the odd order terms by

$$\theta_{2k+1}^{(n)} = \theta_{2k-1}^{(n+1)} + \frac{1}{[\theta_{2k}^{(n+1)} - \theta_{2k}^{(n)}]},\ k = 0, 1, 2, \dots\ , \tag{3.12}$$

where

$$\theta_{-1}^{(n)} = 0,\ \theta_0^{(n)} = S_n\ . \tag{3.13}$$

The even order terms, $\theta_{2k+2}^{(n)}$, give estimates of S whereas the odd order terms, $\theta_{2k+1}^{(n)}$, are , as in ρ algorithm, only intermediate quantities.

Levin's t algorithm

Levin's t-transform may be computed as follows [47]:

$$t_k^{(n)} = \frac{\sum_{i=0}^{k} (-1)^i \binom{k}{i} \left(\frac{n+i}{n+k}\right)^{k-1} \left(\frac{S_{n+i}}{S_{n+i+1} - S_{n+i}}\right)}{\sum_{i=0}^{k} (-1)^i \binom{k}{i} \left(\frac{n+i}{n+k}\right)^{k-1} \left(\frac{1}{S_{n+i+1} - S_{n+i}}\right)},\ k = 0, 1, 2, \dots\ . \tag{3.14}$$

The k^{th} order transform, $t_k^{(n)}$ or $t_k(S_n)$, gives an estimate of the sum, S, of the series. An advantage of the transform is that the higher order iterates are computed from the partial sums, which means that the accuracy to which the partial sums are computed can be preserved in the transform computations. That keeps this transform immune to roundoff errors compared to Shanks' transform.

Chebyshev-Toeplitz algorithm

The algorithm is defined by the following equations [48]:

$$\begin{aligned}
&t_{-1}^{(n)} = 0,\ t_0^{(n)} = S_n,\ \sigma_0 = 1,\\
&t_1^{(n)} = t_0^n + 2t_0^{(n+1)},\ \sigma_1 = 3,\\
&t_{k+1}^{(n)} = 2t_k^{(n)} + 4t_k^{(n+1)} - t_{k-1}^{(n)},\ k = 1, 2, \dots\ ,\\
&\sigma_{k+1} = 6\sigma_k - \sigma_{k-1},\ k = 1, 2, \dots\ ,\\
&T_k^{(n)} = t_k^{(n)}/\sigma_k,\ k = 0, 1, 2, \dots\ .
\end{aligned} \tag{3.15}$$

The n^{th} iterate of the Chebyshev-Toeplitz algorithm is designated by $T_k^{(n)}$, which gives an estimate of the sum of the series.

3.1.3 Specific algorithms

Summation by Parts algorithm

The idea behind this technique is to represent Green's function of the problem in terms of a very slowly convergent modal series of the form [25, 49]

$$S_\infty = \sum_{n=0}^{\infty} \tilde{G}_n f_n = S_{N-1} + R_N\ , \tag{3.16}$$

where $\tilde{G}_n$ represents the slow varying part of the Green's function, and f_n is a fast varying function. For the original series, partial sums and reminders are defined as follows:

$$\begin{aligned}
S_{N-1} &= \sum_{n=0}^{N-1} \tilde{G}_n f_n\ ,\\
R_N &= \sum_{n=N}^{\infty} \tilde{G}_n f_n\ .
\end{aligned} \tag{3.17}$$

Since the partial sums are calculated up to $N-1$, the infinite reminder must be considered. After applying simple arithmetic transformations, the reminder R_N can be rewritten as follows:

$$R_N = \sum_{n=N}^{\infty} \tilde{G}_n^{(0)} f_n^{(0)} = \sum_{i=1}^{\infty} \tilde{G}_N^{(1-i)} f_{N-1}^{(+i)}\ , \tag{3.18}$$

where the succesive sums of f_n and differences of $\tilde{G}_n$ have the following form:

$$\begin{aligned} &\tilde{G}_n^{(0)} = \tilde{G}_n \ , \\ &\tilde{G}_n^{(-i)} = \tilde{G}_{n+1}^{(-i)} - \tilde{G}_n^{(1-i)} \ , \\ &f_n^{(0)} = f_n \ , \\ &f_n^{(+i)} = \sum_{k=n+1}^{\infty} f_k^{(i-1)} \qquad \text{for all} \ \ i = 1, 2, 3 \ldots \ . \end{aligned} \tag{3.19}$$

In our case, the summation by parts is applied to the one-dimensional sum that has the following form:

$$\Gamma_{\text{spatial}}(x) = \sum_{m=-\infty}^{\infty} \mathrm{e}^{\,-\mathrm{j}k_x^i ma} \frac{\mathrm{e}^{\,-\mathrm{j}k_0(x-x'+ma)}}{4\pi(x-x'+ma)} \ , \tag{3.20}$$

that is of the same nature as sum of images i.e. periodic Green's functions in space domain. (3.20) is represented in terms of a slow varying part $\tilde{G}_n$ and a fast varying part f_n. After some algebraic calculations the closed formulas for both, slow and fast varying part, are obtained:

$$\begin{aligned} &\tilde{G}_n^{(i)} = \textstyle\sum_{\pm} \mathrm{e}^{\,\pm\mathrm{j}k_o x} \sum_{k=1}^{i} \frac{(i-1)!}{(k-1)!(i-k)!} \frac{1}{\pm x + [n+(i-k)]d} \ , \\ &f_n^{(i)} = \textstyle\sum_{\pm} \left(\frac{1}{\mathrm{e}^{\,\mathrm{j}d(k_o \pm k_x)} - 1} \right)^{i-1} \mathrm{e}^{\,-\mathrm{j}n(k_0 \pm k_x)d} \ . \end{aligned} \tag{3.21}$$

Poisson's summation formula

To briefly summarize the Poisson transformation [36], we introduce the so-called "comb" function defined as

$$\mathrm{comb}(x) = \sum_{n=-\infty}^{+\infty} \delta(x-n) \tag{3.22}$$

and its Fourier transform,

$$\mathrm{comb}(x)\left(\frac{\nu}{2\pi}\right) = \int_{-\infty}^{+\infty} \mathrm{comb}(x)\mathrm{e}^{\,-\mathrm{j}x\nu} = 2\pi \sum_{n=-\infty}^{+\infty} \delta(\nu - 2n\pi) \tag{3.23}$$

which is also a comb function. S in (3.29) can be written in terms of the comb function as

$$S = \int_{-\infty}^{+\infty} f_{\mathrm{e}}(x)\mathrm{comb}(x)dx \tag{3.24}$$

where f_{e} is an extended function having the property that

$$f_{\mathrm{e}}(n) = f(n) \quad n = 0, \pm 1, \pm 2, ... \tag{3.25}$$

From power's theorem (3.24) becomes

$$S = \int_{-\infty}^{+\infty} f_{\mathrm{e}}(x)\mathrm{comb}(x)dx = \frac{1}{2\pi}\int_{-\infty}^{+\infty} F(\nu)\mathrm{comb}\left(\frac{\nu}{2\pi}\right)\mathrm{d}\nu \tag{3.26}$$

where $F(\nu)$ is the Fourier transform of $f_{\mathrm{e}}(x)$. That is,

$$F(\nu) = \int_{-\infty}^{+\infty} f_{\mathrm{e}}(x)\mathrm{e}^{-\mathrm{j}x\nu}dx \tag{3.27}$$

Substitution of (3.23) into (3.26) yields finally

$$S = \sum_{n=-\infty}^{+\infty} F(2n\pi) \tag{3.28}$$

which is the Poisson transformation of the series in (3.29).
The motivation for using the Poisson transformation is clear if we consider the reciprocal spreading property of the Fourier transform. If $f_{\mathrm{e}}(x)$ is a smooth function which approaches zero gradually as $x \to \infty$, then its Fourier transform $F(\nu)$ is highly localized and the corresponding sum over $\nu = 2n\pi$ converges rapidly. However, $f_{\mathrm{e}}(x)$ should be such that its Fourier transform $F(\nu)$ can be easily computed. Although not necessary, it is usually simpler to define the extended function $f_{\mathrm{e}}(x)$ as $f(x)$. That is, the discrete parameter n is simply replaced by the real variable x.

Kummer's transformation

Contrary to other algorithms explained in this chapter that are non-linear transform it should be noted that Kummer's transform is a linear transform. Since double sums may be evaluated by repeated evaluation of single sums, the Kummer's transform is applied to a single sum of the form [50]

$$S = \sum_{n=-\infty}^{+\infty} f(n) \tag{3.29}$$

The rate of convergence of the series is governed by the asymptotic behavior of $f(n)$ as $n \longrightarrow \infty$. Assume that $f(n)$ is asymptotic to a function $f_1(n)$:

$$f(n) \quad \underline{n \to \infty} \quad f_1(n). \tag{3.30}$$

If $f_1(n)$ is defined for all integers n, then Kummer's transformation gives

$$\sum_{n=-\infty}^{+\infty} f(n) = \sum_{n=-\infty}^{+\infty} [f(n) - f_1(n)] + \sum_{n=-\infty}^{+\infty} f_1(n). \tag{3.31}$$

Generally, f_1 is chosen such that the last series in (3.31) has a known closed-form sum. It is sufficient, however, to transform it into a highly convergent series. For example, it is often

the case that the Poisson transformation of the last series on the right-hand side of (3.31) is used to obtain

$$\sum_{n=-\infty}^{+\infty} f(n) = \sum_{n=-\infty}^{+\infty} [f(n) - f_1(n)] + \sum_{n=-\infty}^{+\infty} F_1(2n\pi) \tag{3.32}$$

where the function F_1 is the Fourier transform of $f_1(n)$. With the appropriate choice of f_1, the slowly converging series on the left-hand side of (3.32) is thus transformed into the sum of two rapidly convergent series on the right hand side.

Ewald's transform

Among the different techniques to speed up the evaluation of GFs [40], the Ewald transformation has clearly demonstrated its suitability for periodic problems, combining efficiently the spectral and the spatial formulations of the GFs. It has been successfully used in the efficient GF computation of 2-D free-space periodic structures with rectangular lattices [51–53] and multilayered planar periodic structures [54], where the approach involves the approximation of spectral domain GFs by the Generalized Pencil-of-Function (GPOF) method [55]. In [20], a new acceleration technique with exponential convergence rate has been presented, that is easier to implement numerically and can perform better than Ewald transformation for moderate accuracies. However, the Ewald transformation remains better for higher accuracy, the only inconvenience being in the computation of the complementary error functions with complex arguments [14].

Potential Green's functions of a periodic structure with rectangular lattice of dimensions a and b in the x and y-directions, respectively, are given by the following space domain form [see (2.18)]

$$\Psi = \frac{1}{4\pi} \sum_{m,n} \frac{\mathrm{e}^{-\mathrm{j}kR_{mn}}}{R_{mn}} \mathrm{e}^{-\mathrm{j}mk_x^{\mathrm{i}}a} \mathrm{e}^{-\mathrm{j}nk_y^{\mathrm{i}}b} \tag{3.33}$$

where

$$R_{mn} = \sqrt{(x - x' - ma)^2 + (y - y' - nb)^2 + (z - z')^2}.$$

Following the results of Ewald [19, 51], we use the identity

$$\frac{\mathrm{e}^{-\mathrm{j}kR}}{R} = \frac{2}{\sqrt{\pi}} \int_0^{\infty} \mathrm{e}^{-R^2 s^2 + \frac{k^2}{4s^2}} \, \mathrm{d}s \tag{3.34}$$

where s is a complex variable and the path of integration is chosen such that the integrand remains bounded as $s \to 0$ and decays as $s \to \infty$. Splitting the path of integration at E in (3.34), we can write

$$\Psi = \Psi_1 + \Psi_2, \tag{3.35a}$$

where

$$\Psi_1 = \frac{1}{4\pi} \sum_{m,n} \mathrm{e}^{-\mathrm{j}mk_x^{\mathrm{i}}a} \mathrm{e}^{-\mathrm{j}nk_y^{\mathrm{i}}b} \frac{2}{\sqrt{\pi}} \int_0^{E} \mathrm{e}^{-R^2 s^2 + \frac{k^2}{4s^2}} \, \mathrm{d}s \tag{3.35b}$$

and

$$\Psi_2 = \frac{1}{4\pi}\sum_{m,n} \mathrm{e}^{-\mathrm{j}mk_x^{\mathrm{i}}a}\mathrm{e}^{-\mathrm{j}nk_y^{\mathrm{i}}b}\frac{2}{\sqrt{\pi}}\int_E^{\infty}\mathrm{e}^{-R^2s^2+\frac{k^2}{4s^2}}\mathrm{d}s \tag{3.35c}$$

If we take into account the identity [56]

$$\frac{2}{\sqrt{\pi}}\int_r^{\infty}\mathrm{e}^{-p^2s^2+\frac{q^2}{4s^2}}\,\mathrm{d}s = \frac{1}{2p}\left(\mathrm{e}^{-\mathrm{j}pq}\mathrm{erfc}(pr-\mathrm{j}\frac{q}{2r}) + \mathrm{e}^{\mathrm{j}pq}\mathrm{erfc}(pr+\mathrm{j}\frac{q}{2r})\right), \tag{3.36}$$

which is valid for $\mathrm{Re}\{p^2\} > 0$ when $s \to \infty$, and we let $p = R_{mn} > 0$, $q = k$, $r = E$, (3.35c) becomes

$$\Psi_2 = \frac{1}{8\pi}\sum_{m,n}\frac{\mathrm{e}^{-\mathrm{j}mk_x^{\mathrm{i}}a}\mathrm{e}^{-\mathrm{j}nk_y^{\mathrm{i}}b}}{R_{mn}}\left[\mathrm{e}^{-\mathrm{j}kR_{mn}}\mathrm{erfc}(R_{mn}E-\frac{\mathrm{j}k}{2E}) + \mathrm{e}^{+\mathrm{j}kR_{mn}}\mathrm{erfc}(R_{mn}E+\frac{\mathrm{j}k}{2E})\right] \tag{3.37}$$

Computation of Ψ_1 is less straightforward and will be shown in what follows [57]. First we rewrite (3.35b)

$$\Psi_1 = \frac{1}{4\pi}\sum_{m,n}\mathrm{e}^{-\mathrm{j}mk_x^{\mathrm{i}}a}\mathrm{e}^{-\mathrm{j}nk_y^{\mathrm{i}}b}\frac{2}{\sqrt{\pi}}\int_0^{E}\mathrm{e}^{-R^2s^2+\frac{k^2}{4s^2}}\mathrm{d}s = \frac{1}{4\pi}\int_0^{E}\frac{2}{\sqrt{\pi}}\mathrm{e}^{\frac{k^2}{4s^2}}\,\mathrm{d}s\sum_{m,n}\mathrm{e}^{-R^2s^2-\mathrm{j}mk_x^{\mathrm{i}}a-\mathrm{j}nk_y^{\mathrm{i}}b} \tag{3.38}$$

Using the 2-D Poisson transformation (3.28), we can write the sum in (3.38) as

$$\begin{aligned}
&\sum_{m,n}\mathrm{e}^{-R_{mn}^2s^2}\mathrm{e}^{-\mathrm{j}mk_x^{\mathrm{i}}a}\mathrm{e}^{-\mathrm{j}nk_y^{\mathrm{i}}b} = \sum_{m,n} f(x-x'-ma, y-y'-nb, z-z')\mathrm{e}^{-\mathrm{j}mk_x^{\mathrm{i}}a}\mathrm{e}^{-\mathrm{j}nk_y^{\mathrm{i}}b}\\
&= \mathrm{e}^{-\mathrm{j}k_x^{\mathrm{i}}(x-x')}\mathrm{e}^{-\mathrm{j}k_y^{\mathrm{i}}(y-y')}\sum_{m,n} f(x-x'-ma, y-y'-nb, z-z')\mathrm{e}^{\mathrm{j}k_x^{\mathrm{i}}(x-x'-ma)}\mathrm{e}^{\mathrm{j}k_y^{\mathrm{i}}(y-y'-nb)}\\
&= \frac{1}{ab}\mathrm{e}^{-\mathrm{j}k_x^{\mathrm{i}}(x-x')}\mathrm{e}^{-\mathrm{j}k_y^{\mathrm{i}}(y-y')}\sum_{m,n}\widetilde{f}\left(\frac{2m\pi}{a}-k_x^{\mathrm{i}}, \frac{2n\pi}{b}-k_y^{\mathrm{i}}, z-z'\right)\mathrm{e}^{\mathrm{j}\frac{2m\pi}{a}(x-x')}\mathrm{e}^{\mathrm{j}\frac{2n\pi}{b}(y-y')}\\
&= \frac{1}{ab}\sum_{m,n}\widetilde{f}(k_{xm}, k_{yn})\mathrm{e}^{\mathrm{j}k_{xm}(x-x')}\mathrm{e}^{\mathrm{j}k_{yn}(y-y')}
\end{aligned} \tag{3.39}$$

where k_{xm} and k_{yn} are defined as in (2.24), and

$$f(\xi,\eta,\zeta) = \mathrm{e}^{-s^2(\xi^2+\eta^2+\zeta^2)}$$

Using

$$\mathcal{F}\left\{\mathrm{e}^{-s^2\xi^2}\right\} = \frac{\sqrt{\pi}}{s}\mathrm{e}^{-\frac{k_x^2}{4s^2}}$$
$$\mathcal{F}\left\{\mathrm{e}^{-s^2\eta^2}\right\} = \frac{\sqrt{\pi}}{s}\mathrm{e}^{-\frac{k_y^2}{4s^2}} \tag{3.40}$$

one obtains

$$\widetilde{f}(k_x,k_y) = \frac{\sqrt{\pi}}{s}\frac{\sqrt{\pi}}{s}\mathrm{e}^{-\frac{k_x^2+k_y^2}{4s^2}}\mathrm{e}^{-s^2(z-z')^2}.$$

and (3.38) becomes

$$\Psi_1 = \frac{1}{2\sqrt{\pi}ab}\sum_{m,n}\mathrm{e}^{\mathrm{j}k_{xm}(x-x')}\mathrm{e}^{\mathrm{j}k_{yn}(y-y')}\int_0^E \mathrm{e}^{-\frac{k_{xm}^2+k_{yn}^2-k^2}{4s^2}}\mathrm{e}^{-s^2(z-z')^2}\frac{\mathrm{d}s}{s^2} \tag{3.41}$$

Using the identity (3.36), we obtain

$$\begin{aligned}\frac{2}{\sqrt{\pi}}\int_{1/E}^{\infty}\mathrm{e}^{-\left(p^2s^2+\frac{\zeta^2}{4s^2}\right)}\mathrm{d}s &= \int_{1/E}^{\infty}\mathrm{e}^{-p^2s^2+\frac{(\mathrm{j}\zeta)^2}{4s^2}}\mathrm{d}s \\ &= \frac{1}{2p}\left[\mathrm{e}^{-\mathrm{j}(\mathrm{j}\zeta)p}\mathrm{erfc}\left(p\frac{1}{E}-\mathrm{j}\frac{\mathrm{j}\zeta}{2/E}\right)+\mathrm{e}^{\mathrm{j}(\mathrm{j}\zeta)p}\mathrm{erfc}\left(p\frac{1}{E}+\mathrm{j}\frac{\mathrm{j}\zeta}{2/E}\right)\right] \\ &= \frac{1}{2p}\left[\mathrm{e}^{\zeta p}\mathrm{erfc}\left(\frac{p}{E}+\frac{\zeta E}{2}\right)+\mathrm{e}^{-\zeta p}\mathrm{erfc}\left(\frac{p}{E}-\frac{\zeta E}{2}\right)\right]\end{aligned} \tag{3.42}$$

Substituting s with $1/s$, the integral in (3.41) becomes

$$\int_0^E \mathrm{e}^{-\frac{k_{xm}^2+k_{yn}^2-k^2}{4s^2}}\mathrm{e}^{-s^2(z-z')^2}\frac{\mathrm{d}s}{s^2} = \int_{1/E}^{\infty}\mathrm{e}^{-\frac{k_{xm}^2+k_{yn}^2-k^2}{4}s^2-\frac{(z-z')^2}{s^2}}\mathrm{d}s = \int_{1/E}^{\infty}\mathrm{e}^{-\alpha_{mn}^2s^2-\frac{(s(z-z'))}{4s^2}}\mathrm{d}s =$$
$$\frac{\sqrt{\pi}}{2}\frac{1}{2\alpha_{mn}}\left[\mathrm{e}^{2\alpha_{mn}(z-z')}\mathrm{erfc}\left(\frac{\alpha_{mn}}{E}+(z-z')E\right)+\mathrm{e}^{-2\alpha_{mn}(z-z')}\mathrm{erfc}\left(\frac{\alpha_{mn}}{E}-(z-z')E\right)\right] \tag{3.43}$$

where we substituted $p=\alpha_{mn}$ and $\zeta = 2(z-z')$ in (3.42). Finally, for Ψ_1, one has the following formula

$$\Psi_1 = \frac{1}{8ab}\sum_{m,n}\frac{\mathrm{e}^{\mathrm{j}k_{xm}(x-x')}\mathrm{e}^{\mathrm{j}k_{yn}(y-y')}}{\alpha_{mn}}\sum_{\pm}\mathrm{e}^{\pm 2\alpha_{mn}(z-z')}\mathrm{erfc}\left(\frac{\alpha_{mn}}{E}\pm(z-z')E\right) \tag{3.44}$$

where $\sum_{\pm}$ designates the sum of the terms with + and − signs, and

$$\alpha_{mn}^2 = \frac{1}{4}\left(k_{xm}^2 + k_{yn}^2 - k^2\right)$$

Splitting Parameter E and GFs Convergence

Both infinite sums in (2.18) and (2.23) are slowly convergent. The image sum is converging faster when the observer point is in the source point region, since the singularity is perfectly included in the expression. However, close to the lateral periodic walls, the convergence is deteriorated as the periodic boundary conditions (BCs) are going to be satisfied only for an infinite number of images taken into account. Each term of the modal sum, on the other hand, satisfies the BCs at the lateral walls and, hence, the convergence of this sum is faster close to the walls. However, taking into account the singularity at the source point would require infinite number of modes leading therefore to the slow convergence of the modal sum in the source point region [14]. The Ewald method successfully combines both modal and image formulations into a fast converging series.

The complementary error function which appears in both series Ψ_1 and Ψ_2 makes these series converge rapidly. The best choice for the splitting parameter E is the one that balances the rate of decay of the two series, making Ψ_1 and Ψ_2 contribute an equal number of terms to the final value Ψ. The approximation to the optimal value of E for 2-D *orthogonal* lattices is given by $E = \sqrt{\pi/(ab)}$ [51].

For high frequencies, or equivalently, large periodic spacings, the complementary error functions in the first terms ($m = n = 0$) of both Ψ_1 and Ψ_2 will take large imaginary arguments and behave as $\exp(k^2/(4E^2))$. These two terms will have very large values that are approximately equal in amplitude but of opposite signs and summing them up will lead to a severe loss of accuracy due to a finite machine precision. This problem can be remedied by requiring that $k^2/(4E^2)$ be smaller than a maximum permitted exponent H^2. In that case the value of the parameter E has to be chosen as

$$E = \max\left(\sqrt{\frac{\pi}{ab}}, \frac{k}{2H}\right). \tag{3.45}$$

For more exhaustive study of the choice of optimum parameter E see [14].

3.2 Results

Section 3.1 gives a detailed overview of the accelerating techniques we intend to apply to 2-D periodic Green's functions.

In general, to accelerate the convergence of a slowly converging series, one needs to transform it into another series that converges faster to the same limit as the original series. Our goal is to first explore general algorithms that are suited for 1-D series and are easy to implement. In numerical computation one wants to show how the accelerating technique is favorable in terms of CPU time and simple to apply. Then, generality is of importance, i.e. one wants accelerating technique to be as much as possible independent from input parameters (cell

size i.e. periodicity, incidence angles) values. Moreover, it is important to have an algorithm valid for a wide class of problems, e.g. free-standing ground planes, periodically repeated metallic patches deposited on a dielectric substrate, periodically perforated ground plane of finite thickness, etc.

In this section, we initially treat accelerating techniques applied to 1-D sums. Then we choose the most appropriate one that is to be extended to the 2-D periodic Green's function in both, the free-space and the multilayered case.

3.2.1 1-D periodic sums

The objective of this subsection is to make a qualitative study of the existing 1-D general algorithms in order to find one that will perform in an optimal way for any set of relevant periodic structure's parameters. To evidence the problem, we can say that it is impossible for a single transform/algorithm to accelerate a wide class of series, for example, the ρ algorithm works better on series where the partial sums show a monotonic behavior than on those with oscillatory sequences. On the other hand, Wynn - ϵ (Shanks) algorithm used here for 1-D sums, would encounter, very fast, instabilities with monotonic sequences, even when small accuracies are required, due to accumulation of round-off errors.Therefore, providing stable results and good convergence for the different unit cell's sizes, different angles of incidence and for arbitrary source - observer distances is not so apparent. Moreover, comparing the most popular algorithms readily available would provide us with the information which algorithm is the most robust and reliable, and for that reason chosen to proceed to the real 2-D structures. The compared algorithms are Shanks', Chebyschev - Toeplitz, θ - algorithm, ρ - algorithm and Levin's transform, (see 3.1.2). Let us define:

$$\Gamma_{\text{spatial}}(x) = \sum_{m=-\infty}^{\infty} \mathrm{e}^{-\mathrm{j}k_x^i ma} \frac{\mathrm{e}^{-\mathrm{j}k_0(x-x'+ma)}}{4\pi(x-x'+ma)} \tag{3.46}$$

$$\Gamma_{\text{spectral}}(x) = \sum_{m=-\infty}^{\infty} \frac{1}{\mathrm{j}2a\gamma} \mathrm{e}^{-\mathrm{j}k_{xm}(x-x')}. \tag{3.47}$$

First, we study 1-D infinite sums (3.20) and (3.47) that are of same nature as 2-D infinite periodic Green's functions. Without loss of generality, the source is fixed at the origin $x = 0$ and the observer is placed at different locations in the unit cell or "line segment" of size a. For the sake of simplicity of notation in this subsection, further on we will name $R = |x - x'|$ source-observer distance.

For each case, the series in (3.20) or in (3.47) are summed up with sufficiently large number of terms to achieve a desired accuracy. The resulting sum is then employed in computing a relative error defined as

$$\zeta_r = \Big|\frac{\tilde{S} - S}{S}\Big| \tag{3.48}$$

where S and $\tilde{S}$ are the values obtained from the direct sum calculated up to desired precision and from a transformation method, respectively. The slow convergence rate of the sums (3.20) and (3.47) can be simply demonstrated with a small numerical calculation e.g. even after

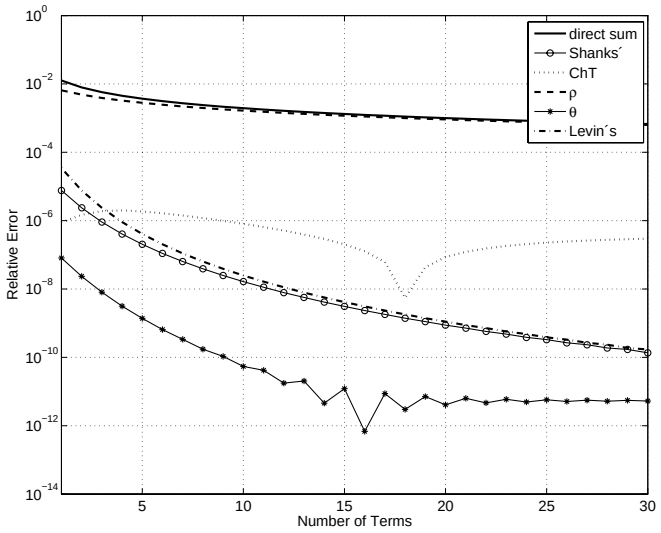

Figure 3.1: Relative error as function of the number of terms for image formulation: $a = 0.5\lambda$; $R = 0.01\lambda$; $\theta_\mathrm{i} = \phi_\mathrm{i} = 0$.

summing 200000 terms of (3.20) in a straightforward manner i.e. direct sum, two adjacent partial sums still differ in 6^{th} digit which means that even after taking 100001 partial sums it is not possible to obtain higher precision than in first 6 significant digits.

First, we consider the image sum of a 1-D periodic structure with periodicity given by a. Fig. 3.1 and Fig. 3.2 show the convergence rate of the image sum (3.20) for direct sum and different acceleration algorithms applied to speed up its evaluation. For periodicity $a = 0.5\lambda$ and normal plane wave incidence, for both $R = 0.01\lambda$ and $R = 0.24\lambda$, we observe that the convergence is the best for θ and Shanks' algorithm respectively, and smaller relative error is observed when source and observer are close, $R = 0.01\lambda$. The worst convergence rate is obtained by ρ algorithm that is almost as slow as direct sum. Next, the results are shown for the same periodicity $a = 0.5\lambda$ and $R = 0.01\lambda$ but for angles of incidence $\theta_\mathrm{i} = \varphi_\mathrm{i} = \pi/4$, Fig. 3.3. It is obvious that the only algorithm giving a good convergence rate is Shanks' transform. While the results of Chebyschev-Toeplitz can be acceptable, if no high accuracy is needed, all the other algorithms show a quite oscillatory behavior. For a periodicity $a = \lambda$, source-observer distance $R = 0.011\lambda$ and normal plane wave incidence, results are presented in Fig. 3.4. In the case of real 2-D periodic Green's function this set of input parameters would lead to "blind spot" phenomena (see [58]). In case of 1-D image sum (3.20) save for the Shanks' algorithm, all the others break down. In the following, the results of convergence study for modal sums (3.47) are presented. We consider the same 1-D periodic array of point sources with periodicity a i.e. reciprocal lattice k_{xm} defined in (2.24). For a normal plane wave incidence, periodicity $a = 0.5\lambda$ and source-observer distance $R = 0.24\lambda$ the results are presented in Fig. 3.5. The relative error versus number of terms is decreasing

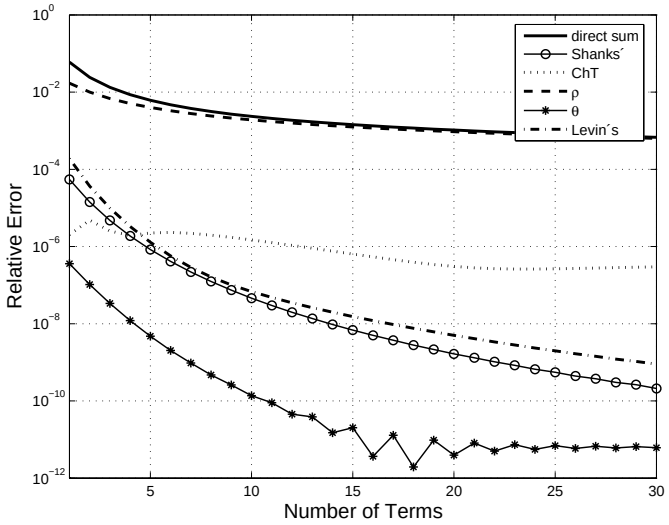

Figure 3.2: Relative error as function of the number of terms for image formulation: $a = 0.5\lambda$; $|x - x'| = 0.24\lambda$; $\theta_\mathrm{i} = \phi_\mathrm{i} = 0$.

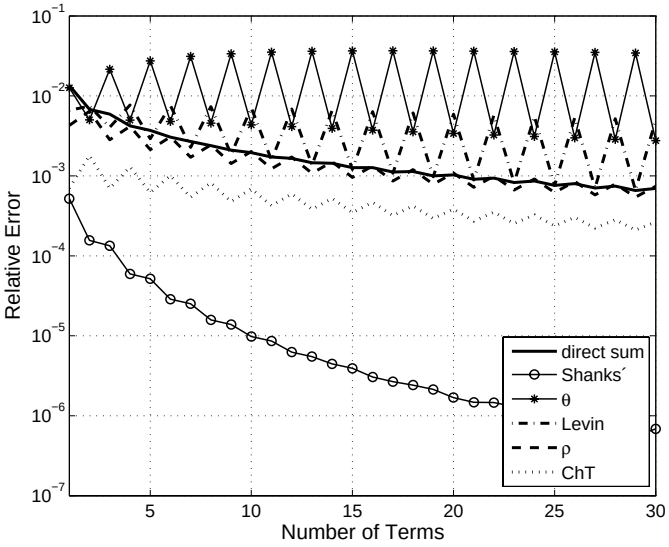

Figure 3.3: Relative error as function of the number of terms for image formulation: $a = 0.5\lambda$; $|x - x'| = 0.01\lambda$; $\theta_\mathrm{i} = \phi_\mathrm{i} = \pi/4$.

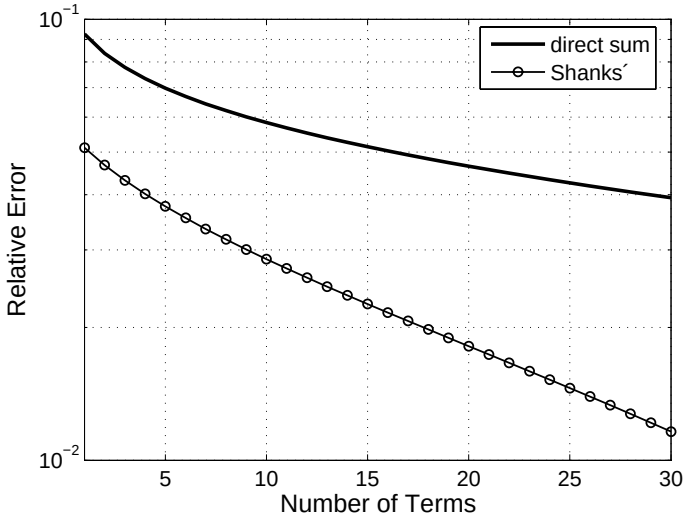

Figure 3.4: Relative error as function of the number of terms for image formulation: $a = \lambda$; $|x - x'| = 0.01\lambda$; $\theta_{\mathrm{i}} = \phi_{\mathrm{i}} = 0$.

only in the case of Shanks' transform while the convergence obtained by the others algorithms cannot be considered as satisfactory. Then, in Fig. 3.6 and Fig. 3.7, the results are shown for direct sum, θ-algorithm and Shanks' transform. For periodicity $a = 0.98\lambda$ and source-observer distance $R = 0.48\lambda$, the results obtained by Shanks' transform are shown to be more favorable compared to those obtained by θ-algorithm (see Fig. 3.6). For normal plane wave incidence, periodicity $a = 0.99\lambda$, and source-observer distance $R = 0.49\lambda$, the convergence rate presented in Fig. 3.7 is better for θ-algorithm than for Shanks, although both results are acceptable. To sum up, for image sum (3.20), normal plane wave incidences, and different values of source-observer distance R, the best convergence is obtained for θ and Shanks' transform. Slightly better results are obtained for smaller R, i.e. for the observer closer to the source. That is as expected, since the image sum converges faster when the observer is close to the source and encounters problems when fulfilling boundary conditions. However, in case of plane incidence different from normal one, and for conditions similar to those of a blind spot for the real 2-D periodic Green's function, the best relative error is achieved with Shanks' transform. For modal sums (3.47) for an arbitrary phase shift, the best results are obtained with Shanks' transform.

From the numerical experiments we can conclude that for 1-D sums, (3.20) and (3.47), only Shanks' transform and θ-algorithm give satisfactory convergence rate. More precisely, very good convergence but not always very stable results are obtained with θ-algorithm, while the Shanks' transform gives fast convergence and stable results for any incidence, periodicity or source-observer distance. For that reasons, the Shanks' algorithm was opted as a definitive choice to proceed to the treatment of 2-D planar structures.

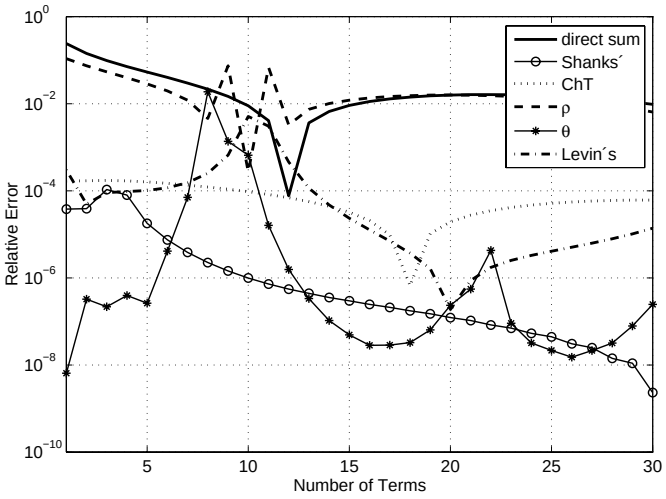

Figure 3.5: Relative error as function of the number of terms for modal formulation: $a = 0.5\lambda$; $R = 0.24\lambda$; $\theta_\mathrm{i} = \phi_\mathrm{i} = 0$.

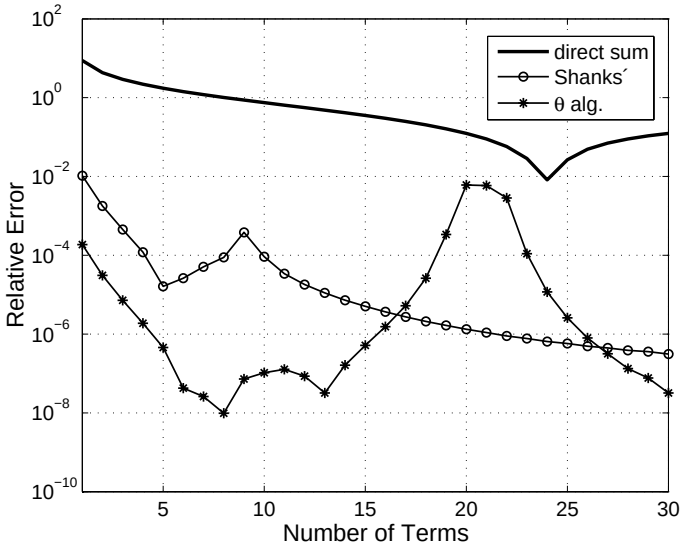

Figure 3.6: Relative error as function of the number of terms for modal formulation: $a = 0.98\lambda$; $R = 0.48\lambda$; $\theta_\mathrm{i} = \phi_\mathrm{i} = \pi/4$.

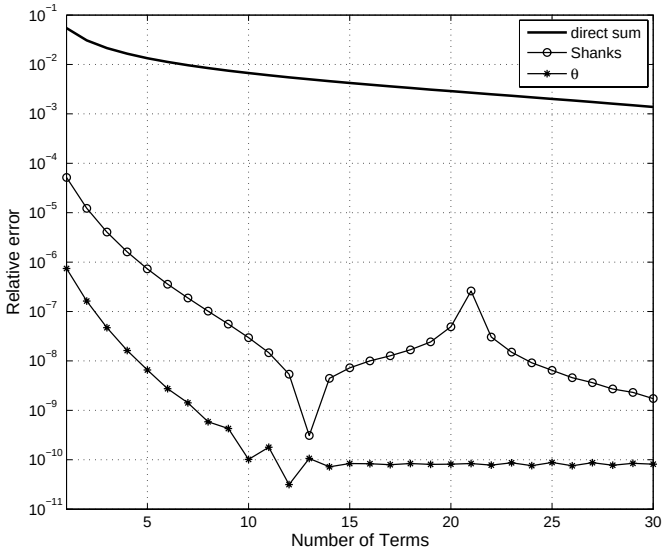

Figure 3.7: Relative error as function of the number of terms for modal formulation: $a = 0.99\lambda$; $R = 0.49\lambda$; $\theta_\mathrm{i} = \phi_\mathrm{i} = 0$.

3.2.2 2-D periodic free-space Green's function

Shanks' transform was found to be the most robust and reliable technique for acceleration of 1-D periodic sums. Therefore in this section we extend it to the case of 2-D periodic problems. The function to be accelerated in this section is 2-D free-space periodic Green's function explained in 2.4. The response at (x, y, z) to each point source must be summed to obtain the value of the double infinite series. The incident field is a plane wave given by wave vector $\mathbf{k}$. Both formulations, modal and image, are used to test the 2-D expansion of the Shanks' transform. Both formulations, image and modal sums are given by (2.18) and (2.20) in 2.4.1 and 2.4.2 respectively.

Both series (2.18) and (2.20) converge rapidly when source and observer are not on the same plane $z \neq z'$ as the exponential factor aids in convergence. For that reason we consider the most difficult case - the source and the observer on the same plane of the structure, $z = z'$.

Shanks' algorithm in 2-D

After a brief overview of the double infinite sums to be accelerated, the explanation of the way Shanks' transform is implemented will be given in this subsection. The algorithm is applied in following manner. For each m (x index)we define 1-D series and sum them up in n (y index). Each "m" sum is accelerated by Shanks' transform. In this way, a new 1-D infinite array is obtained, where each term is the approximation of the sum in y-direction. Once more, the Shanks' algorithm, more precisely Wynn's ε algorithm, is applied to the new array of partial sums and approximative value of 2-D infinite sum found. The validity of the sums'

approximations obtained by Shanks' algorithm was compared to the values approximated by Ewald's transform which is known to converge fast [59]. The reason that we have opted for Shanks' algorithm was the simplicity of accelerating any type of series without any analytical transform on the series' kernel that is the main drawback of the Ewald's transform. In order to give an insight how the approximations of the free space periodic Green's functions evaluated by two different means agree, the results are summarized in Table 3.1. It is shown that the approximations of the periodic free-space Green's function obtained with Ewald's transform and Shanks' 2-D transform agree in first 8 to 10 digits depending on the domain where the transformations are performed and the choice of parameters (periodicity, cell size, incidence angles). In the case of Shanks' transform the total number of terms is $(2 \cdot 250 + 1)^2 = 251001$ while for Ewald's transform only $(2 \cdot 2 + 1)^2 = 25$ terms in each of the two sums were needed. Without loss of generality, source is always placed at the origin. In Fig. 3.8 results are shown for both domains, for periodicity $a = b = 0.5\lambda$ and a normal plane wave incidence, source-observer distance $0.01\sqrt{2}\lambda$. In Fig. 3.9, the relative error in the case of the Ewald's transform for the same situation is given. Next, in Fig. 3.10 the presented results correspond to the case where the source-observer distance is $0.24\sqrt{2}\lambda$ and the other parameters kept the same as in the previous case, followed by the Fig. 3.11 where the relative error is presented for the same case by the means of Ewald's transform. The oscillations in the modal sum do appear in the range when the numerical precision of the machine is achieved. The results for the periodicity $a = b = 0.5\lambda$, source-observer position $0.01\sqrt{2}\lambda$ and angles of incidence $\theta_\mathrm{i} = \varphi_\mathrm{i} = \pi/4$ are presented in Fig. 3.12.

d,x,θ,ϕ	Shanks'	Ewald
(a)	5.18768391331903 - 0.31830989511007i	5.18768390867757 - 0.31830988618379i
(b)	-0.32482245142574 - 0.31830988681800i	-0.32482245196704 - 0.31830988618379i
(c)	5.25210692710614 - 0.42416940676606i	5.18799712354631 - 0.31883049513217i
(d)	-1.99817123125621 - 0.07690576526595i	-1.99773146869776 - 0.08119321655540i

Table 3.1: Approximation of the double infinite periodic Green's function obtained with Shanks' 2D algorithm and Ewald's transform, (a) $d = h = 0.5\lambda$, $x = y = 0.01\lambda$, $\theta_\mathrm{i} = \phi_\mathrm{i} = 0$; (b) $d = h = 0.5\lambda$, $x = y = 0.24\lambda$, $\theta_\mathrm{i} = \phi_\mathrm{i} = 0$; (c) $d = h = 0.5\lambda$, $x = y = 0.01\lambda$, $\theta_\mathrm{i} = \phi_\mathrm{i} = \pi/4$; (d) $d = h = 0.99\lambda$, $x = y = 0.49\lambda$, $\theta_\mathrm{i} = \phi_\mathrm{i} = 0$.

Shanks' algorithm "spiral"

In this part, another technique of accelerating the double infinite periodic Green's functions using Shanks' algorithm is elaborated. An idea that seemed logical to explore was to transform the 2-D double sum into a 1-D infinite sum and accelerate the latter with the Shanks's transform. In a 2-D array of point sources displaced in the orthogonal rectangular grid the terms are taken in a spiral way starting from the unit cell source as shows Fig. 3.13. That means the terms with the most important contribution are taken first. After the 1-D array is obtained, the cross-rule of Shanks' algorithm (3.7) is applied to accelerate the sum. The standard Wynn's ϵ algorithm is impossible to apply because of round-off errors. The new sums are extremely irregularly oscillating series and the relative error are quite large. On the

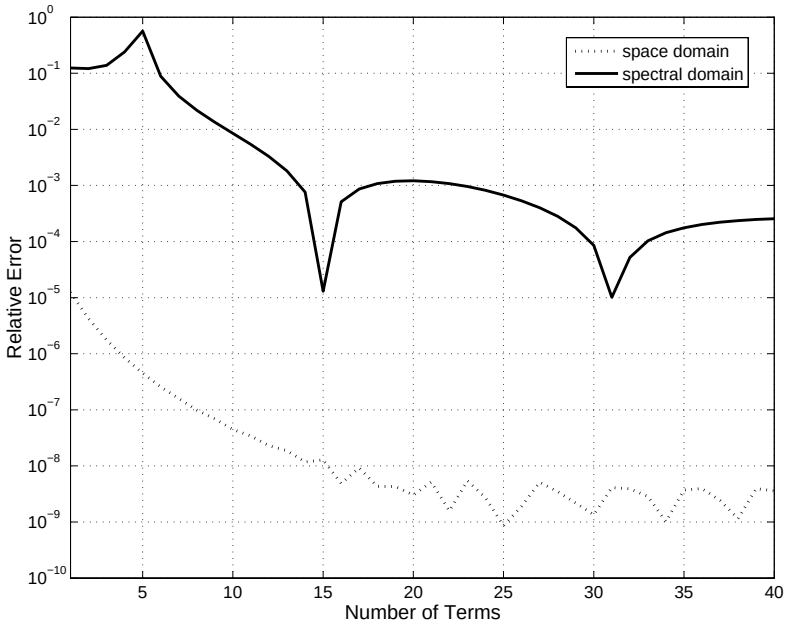

Figure 3.8: Relative error as a function of the number of terms for Shanks' transform: $a = b = 0.5\lambda$; $R = 0.01\sqrt{2}\lambda$; $\theta_{\mathrm{i}} = \phi_{\mathrm{i}} = 0$.

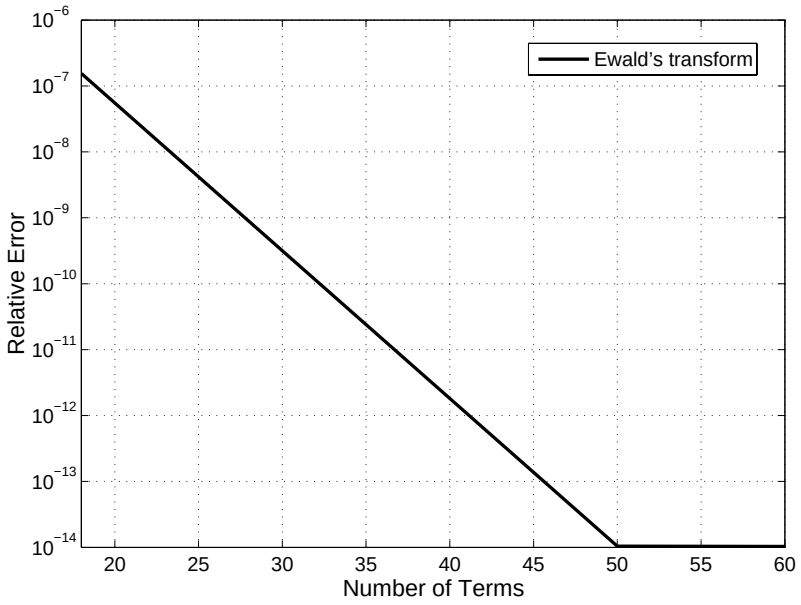

Figure 3.9: Relative error as a function of the number of terms for Ewald's transform transform: $a = b = 0.5\lambda$; $R = 0.01\sqrt{2}\lambda$; $\theta_{\mathrm{i}} = \phi_{\mathrm{i}} = 0$.

other hand, the good results are expected since the series is accelerated effectively twice, once summing the most important terms first and the second time applying the general accelerating algorithm. The results are shown in Fig. 3.14–Fig. 3.2.2. This trial of accelerating the 2-D infinite periodic Green's function by transforming it into the one dimensional sum and applying Shank's transform does not give satisfactory error. This can be explained by the very irregular oscillatory behavior of the series.

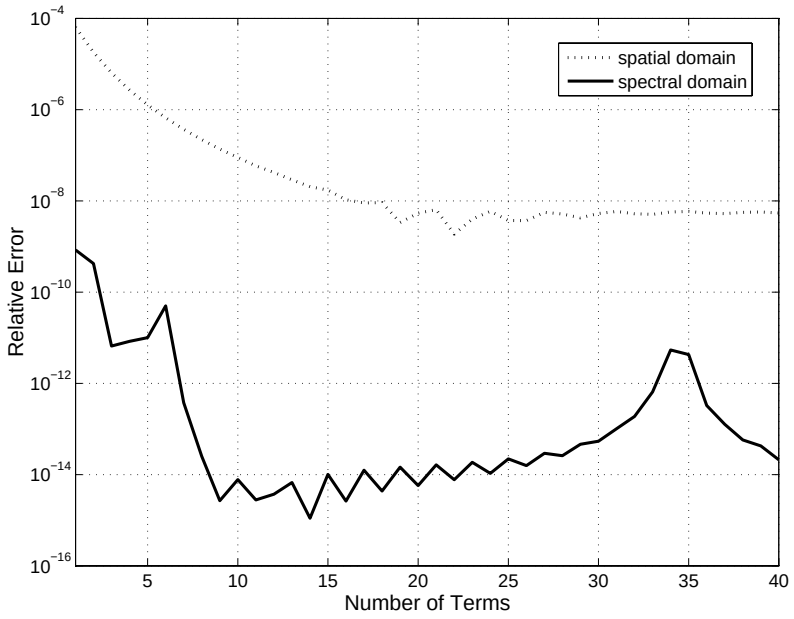

Figure 3.10: Relative error as a function of the number of terms for Shanks' transform: $a = b = 0.5\lambda$; $R = 0.24\sqrt{2}\lambda$; $\theta_{\mathrm{i}} = \phi_{\mathrm{i}} = 0$.

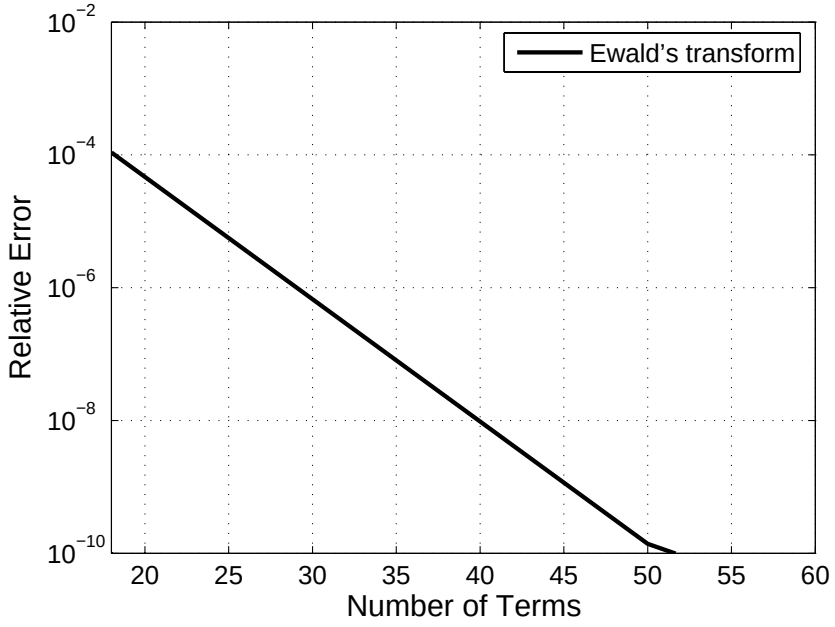

Figure 3.11: Relative error as a function of the number of terms for Ewald's transform: $a = b = 0.5\lambda$; $R = 0.24\sqrt{2}\lambda$; $\theta_{\mathrm{i}} = \phi_{\mathrm{i}} = 0$.

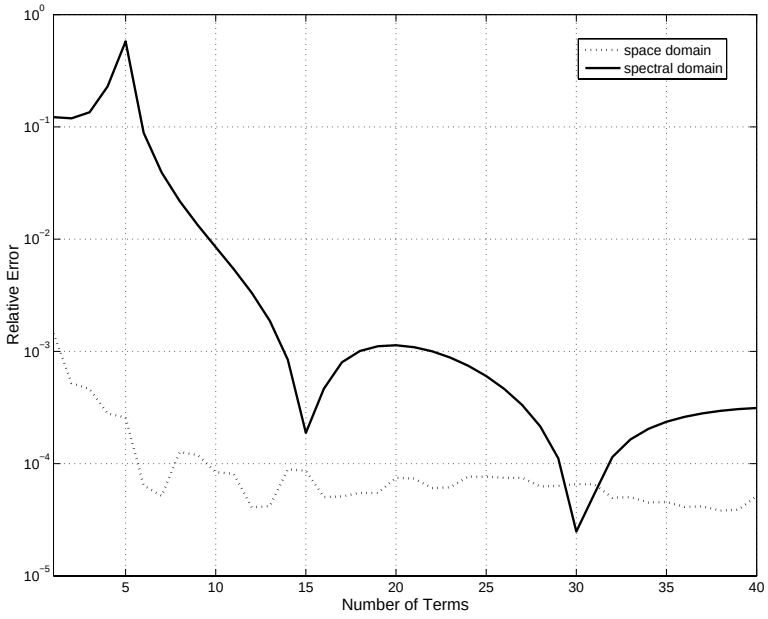

Figure 3.12: Relative error as a function of the number of terms for Shanks' transform: $a = b = 0.5\lambda$; $R = 0.01\sqrt{2}\lambda$; $\theta_\mathrm{i} = \phi_\mathrm{i} = \pi/4$.

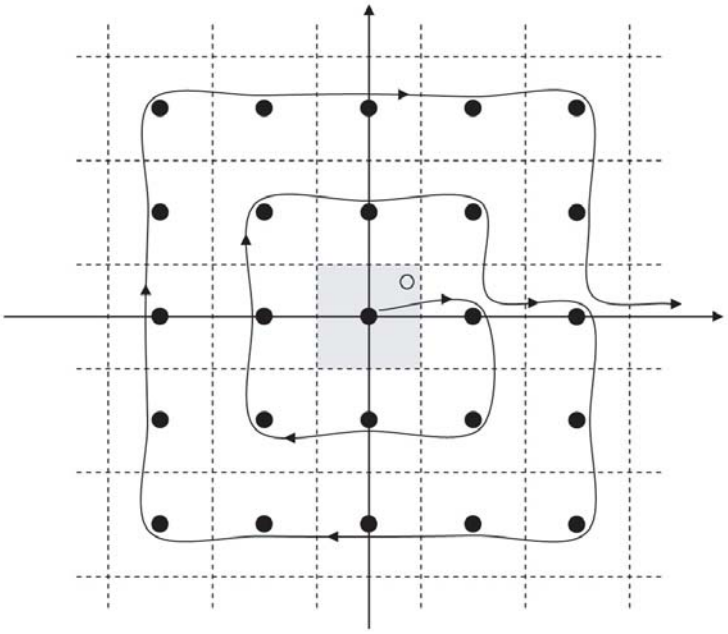

Figure 3.13: 2-D array of sources.

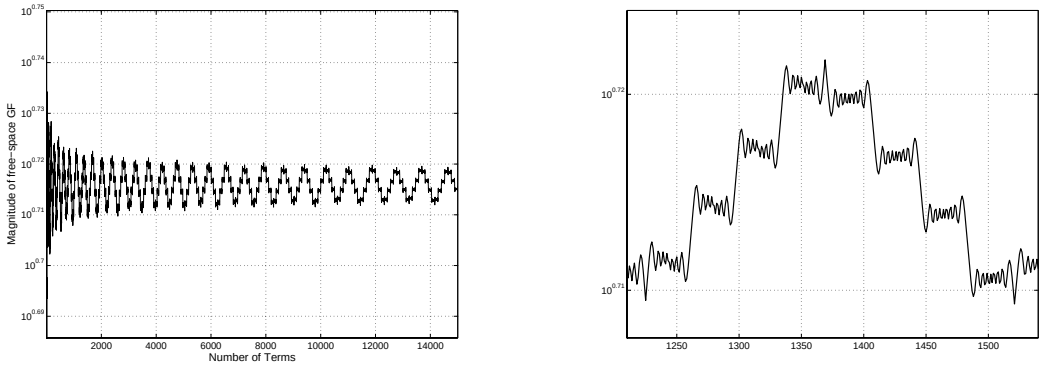

(a) Partial sums for $a = b = 0.5\lambda$; $R = 0.01\sqrt{2}\lambda$; $\theta_{\mathrm{i}} = \phi_{\mathrm{i}} = 0$.

(b) Small sequence of the series.

Figure 3.14: Partial sums and a small sequence of the spiral array representing 2-D infinite periodic Green's function-direct image sum.

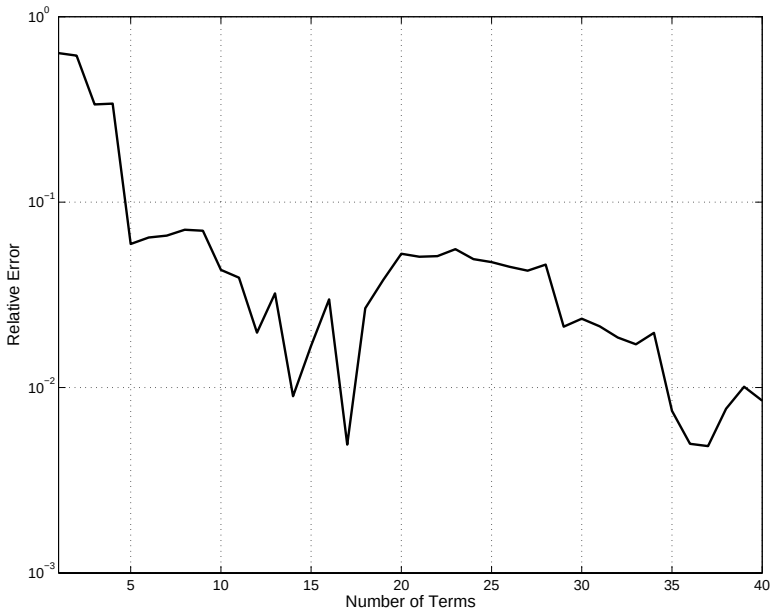

Figure 3.15: Relative error for image sum as a function of the number of terms using Shanks' for $a = b = 0.5\lambda$; $R = 0.01\sqrt{2}\lambda$; $\theta_{\mathrm{i}} = \phi_{\mathrm{i}} = 0$.

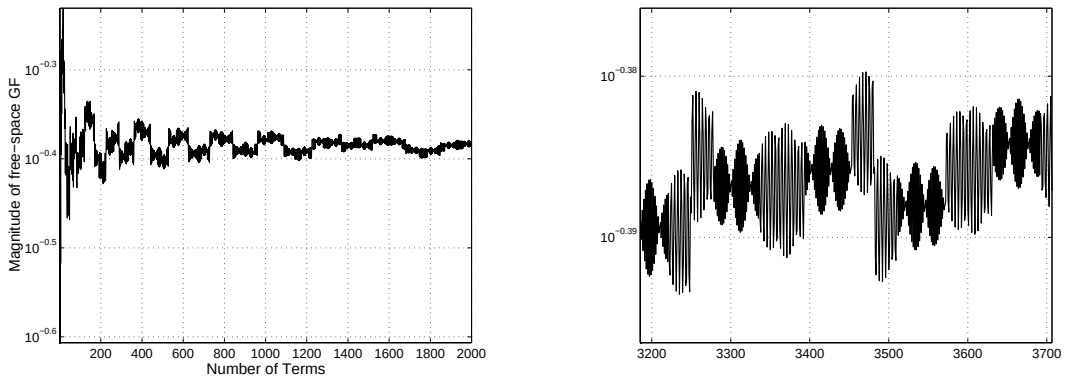

(a) Partial sums for $a = b = 0.5\lambda$; $R = 0.24\sqrt{2}\lambda$; $\theta_{\mathrm{i}} = \phi_{\mathrm{i}} = 0$.

(b) Small sequence of the series.

Figure 3.16: Partial sums and a small sequence of the spiral array representing 2-D infinite periodic Green's function-direct modal sum.

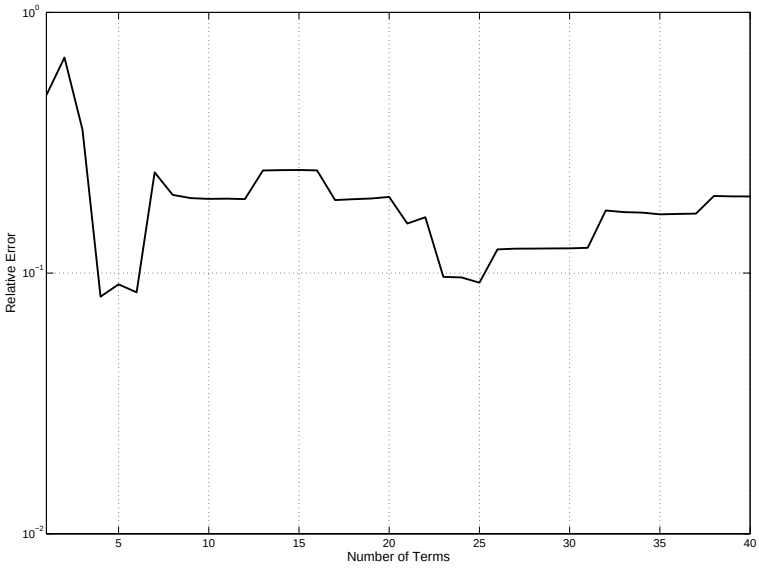

Figure 3.17: Relative error as a function of the number of terms using Shanks' for $a = b = 0.5\lambda$; $R = 0.24\sqrt{2}\lambda$; $\theta_\mathrm{i} = \phi_\mathrm{i} = 0$.

3.3 Green's function for multilayered structures

The configuration to be studied is made of metallic structures embedded in laterally unbounded large dielectric slabs with or without the ground plane below as sketched in Fig. 3.18. For the sake of simplicity the structure studied here will be a single layered dielectric slab with

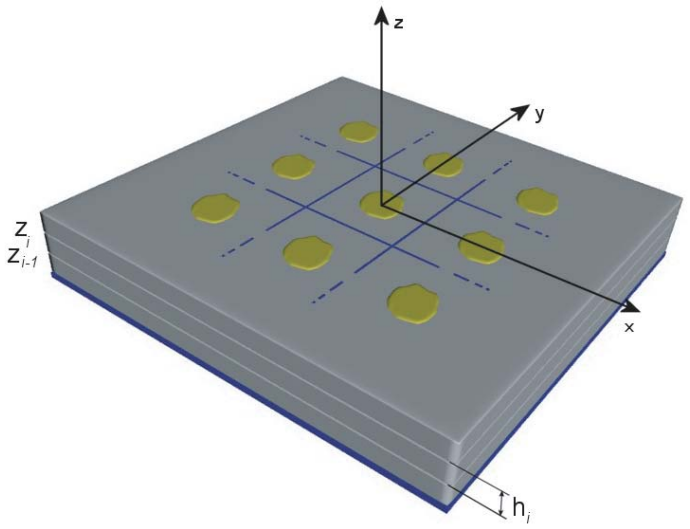

Figure 3.18: 2-D periodic structure of metallic patches printed on dielectric slabs.

the ground plane below. The general form of multilayered Green's functions is presented in details in Chapter 2. For a given slab of thickness h, identical elements of an arbitrary shape are evenly distributed along both planar axes with periodicities of a and b. The thickness of these conductors is assumed to be negligible. The stratified structure is illuminated by a plane wave with the incidence angle specified by θ_{in} and φ_{in}. The periodic Green's functions are defined in the form of modal sums or the sum of images i.e. in "spectral" and "spatial" formulation respectively as

$$G_p = \frac{1}{S} \sum_{m=-\infty}^{\infty} \sum_{n=-\infty}^{\infty} \tilde{G}_{mn}(k_{xm}, k_{yn}) \mathrm{e}^{-\mathrm{j}k_{xm}(x-x')} \mathrm{e}^{-\mathrm{j}k_{yn}(y-y')} \tag{3.49}$$

$$G_p = \sum_{m=-\infty}^{\infty} \sum_{n=-\infty}^{\infty} G_{mn}(x, y) \mathrm{e}^{\mathrm{j}k_x^{\mathrm{i}} ma} \mathrm{e}^{\mathrm{j}k_y^{\mathrm{i}} nb} \tag{3.50}$$

3.3.1 Shanks' algorithm

Calculations are made for "on-plane" case where the series (3.49), as well as the series (3.50), have the slowest convergence, i.e., $z = z' = 0$. The structure under consideration is 2-D infinite

array of patches evenly distributed in $x-y$ plane printed on a single dielectric slab Fig. 3.19. The periodicity is given by $a = b = 1.1\lambda_0$, frequency equal $f = 30$GHz and normal plane wave incidence. Without any loss of generality, a source is placed at $x' = y' = 0$ and the observer is taken to be at different locations ρ where $\rho = \sqrt{x^2 + y^2}$ with $x = y$, i.e. the observer moves along the unit cell's diagonal.

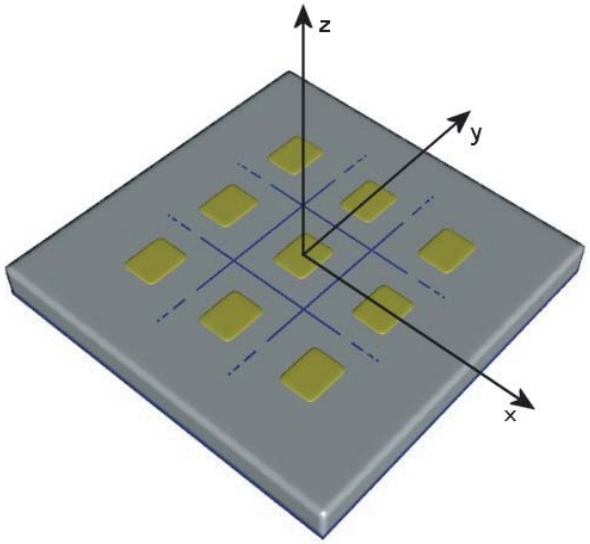

Figure 3.19: 2-D periodic structure printed on a single layered dielectric slab.

Spatial domain

The spatial Green's function for open microstrip structures, that is a case in our problem here, is generally represented by oscillatory Sommerfeld integrals. In this subsection we will show the results for the convergence study of image sum accelerated by Shanks' transform. The results were verified with those obtained by Ewald's transform.

The simulations are performed for the substrate thickness $h/\lambda_0 = 0.04$ and the number of partial sums given by 36, that makes in overall a total number of terms 5329. The relative permittivity taken to be 1 facilitates the results check-up, since the GFs calculated using Sommerfeld integrals, being easy to compare with the Ewald's transform. In Fig. 3.20 the real and the imaginary parts of the scalar potential Green's function vs. normalized transverse distance are presented for the source position $(x_0, y_0) = (0.005a, 0.005b)$. It is evident that still not enough terms are taken to achieve a smooth curve, but the problem lies, besides the Shank's algorithm, in the way the spatial Green's function is evaluated, that will be explained later. In Fig. 3.21 the real and the imaginary parts of the vector potential Green's function vs. normalized transverse distance are presented for the source position $(x_0, y_0) = (0.5a, 0.5b)$. The function's approximations obtained by Shanks' and Ewald's transform show good agreement. Next, in the Fig. 3.22 only the source position being changed $(x_0, y_0) =$

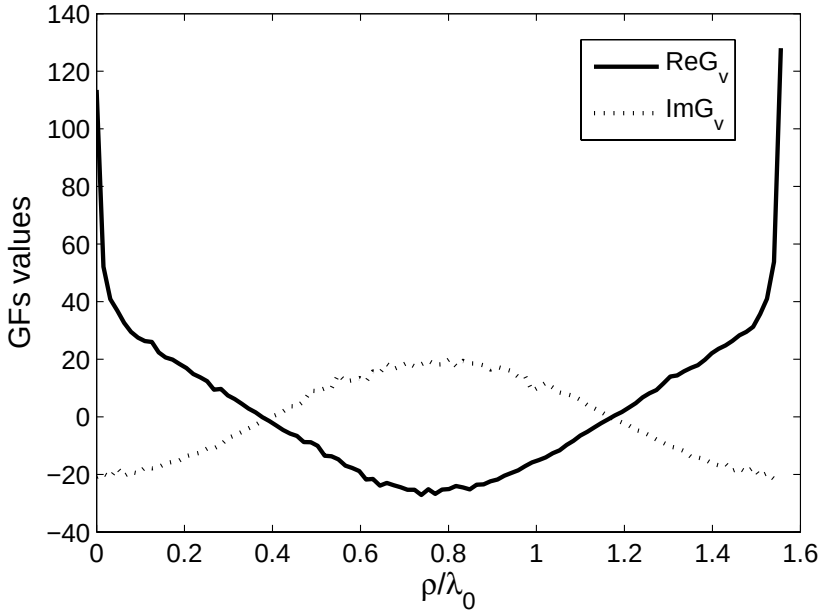

Figure 3.20: Real and imaginary part of image sum - periodic Green's function for the scalar potential vs. the normalized transverse source-observer distance ρ/λ_0.

$(0.25a, 0.75b)$ and the results shown for both, the Shanks' and the Ewald's transform. It is clear that those obtained by Ewald's transform give a better approximation of the Green's function.

Spectral domain

As a numerical example, the sum formula (3.49) accelerated by the ameliorated version of the cross-rule Shanks' transform is used to evaluate the periodic Green's function of a 2-D structure of x-directed point dipole sources printed on a grounded substrate of thickness h and relative permittivity ε_r. The function evaluated here is the scalar potential of a point charge.

Fig. 3.23 shows the magnitude of the periodic Green's function of the scalar potential calculated using the Shanks' transform vs. normalized transverse distance ρ/λ_0 for the periodic structure printed on a substrate $\varepsilon_\mathrm{r} = 9.8$ and for the different substrate thickness, $h/\lambda = 0.02, 0.04, 0.06$. The results obtained for the same structure but for the different $\varepsilon_\mathrm{r} = 2.55$ are presented in Fig. 3.24. For the value of the substrate thickness $h/\lambda_0 = 0.04$ results agree well with the results obtained by Shubair et al. [60]. It is observed in both, Fig. 3.23 and Fig. 3.24, along the diagonal line of the unit cell, that the scalar potential periodic Green's function has a strong field at the sources: $\rho = 0, 1.56\lambda_0$. Between the sources, the Green's function is dominated by the surface wave that increases in magnitude with increased dielectric constant and increased substrate thickness h/λ_0. The magnitude of the scalar po-

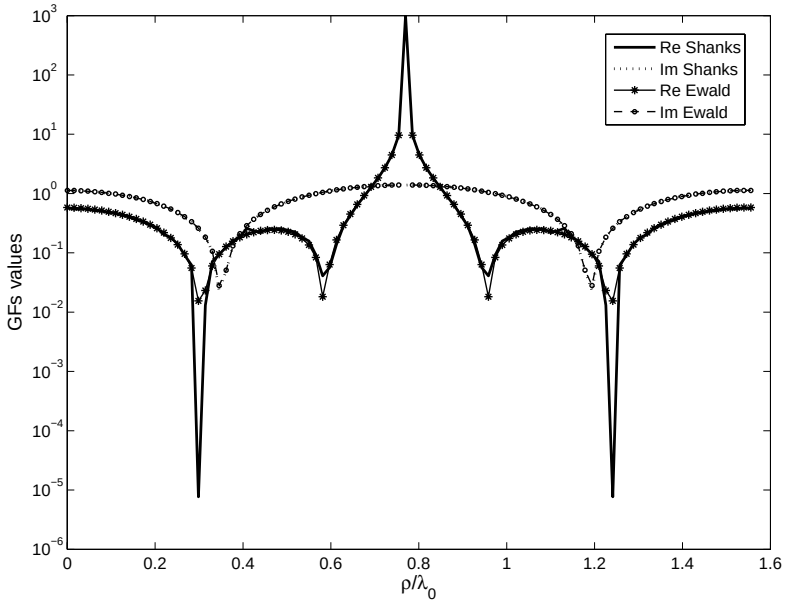

Figure 3.21: Real and imaginary part of image sum - periodic Green's function for the vector potential vs. the normalized transverse distance ρ/λ_0.

tential periodic Green's function calculated using modal sums and the sum of images for the grounded slab of thickness $h/\lambda_0 = 0.04$ with the relative dielectric constant equal to that of the free-space $\varepsilon_\mathrm{r} = 1$ is shown in Fig. 3.25. The good agreement between the approximations of periodic Green's function obtained by the modal sums and the sum of images is observed. On the contrary, the results for the scalar potential periodic Green's function, presented in Fig. 3.26 and Fig. 3.27 that are for $\varepsilon_\mathrm{r} = 9.8$ and for the substrate thickness $h/\lambda_0 = 0.04$ and $h/\lambda_0 = 0.046$, respectively, justify the choice of the modal sums' formulation to proceed further. The sums in both, (3.49) and (3.50), were truncated after 78 partial sums that gives in total $(2 \cdot 78 + 1)^2 = 24639$ terms. It is obvious that for the same number of terms in the double sums the smooth and stable Green's function approximation is obtained by the modal sums while for the same number of partial sums the sum of images shows an oscillatory behavior.

This can be explained by the fact that every term in the image sum is numerically obtained by evaluation of the Sommerfeld integral. A lot of terms need to be taken in the image sum to converge. In other terms, it means large distances in Sommerfeld integral (the more terms we take to sum up the 2-D periodic Green's function the more distant will be the source and image). For large distances high accuracy in Sommerfeld integral evaluation can not be achieved and therefore special Taylor series for integration along imaginary axis should be implemented [25, 27].

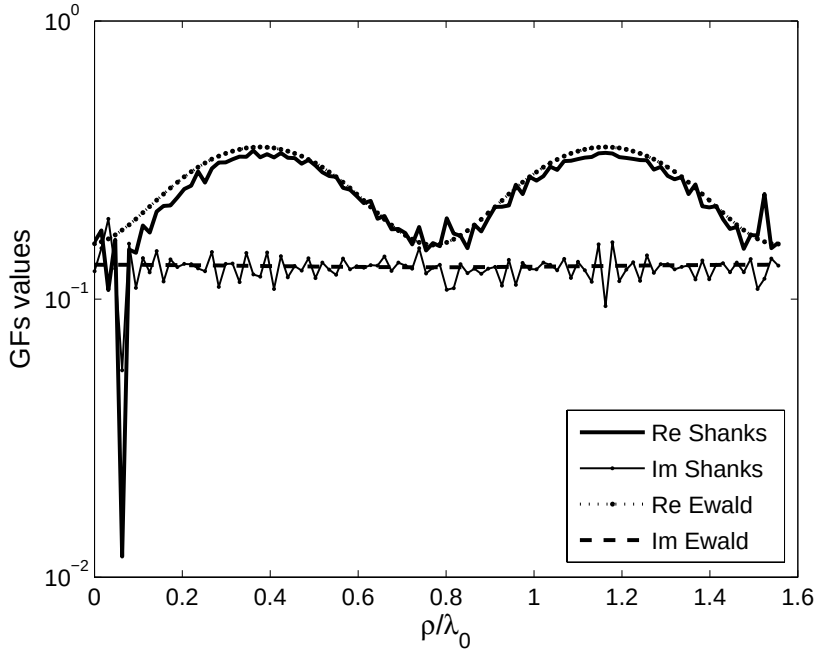

Figure 3.22: Real and imaginary part of image sum - periodic Green's function for the vector potential vs. the normalized transverse distance ρ/λ_0.

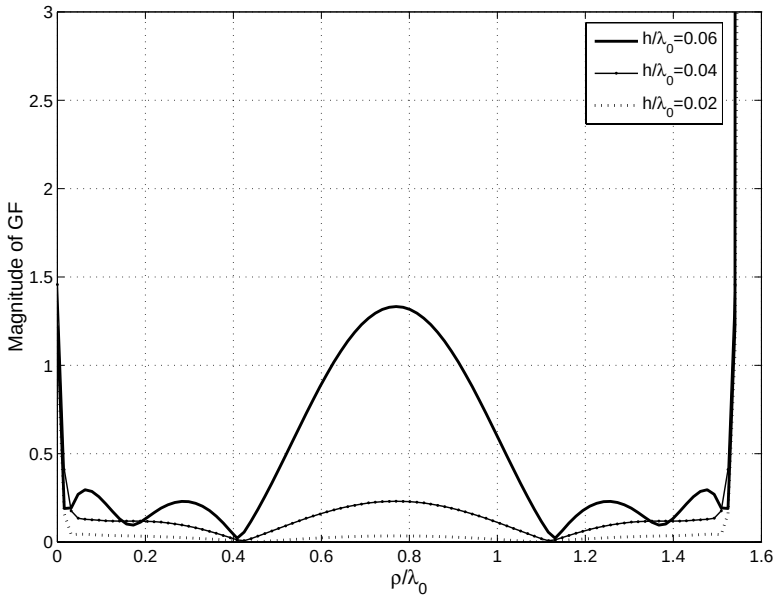

Figure 3.23: Magnitude of modal sum - periodic Green's function G_p for the charge scalar potential calculated using the Shanks' transform vs. normalized transverse distance ρ/λ_0 for $\varepsilon_\mathrm{r} = 9.8$.

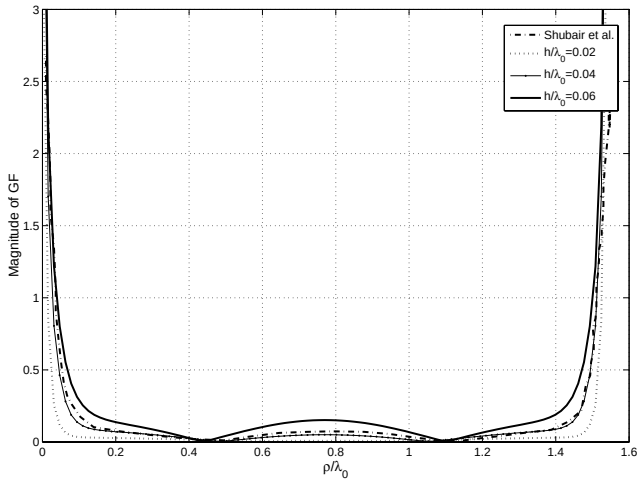

Figure 3.24: Magnitude of modal sum - periodic Green's function G_p for the charge scalar potential calculated using the Shanks' transform vs. normalized transverse distance ρ/λ_0 for $\varepsilon_{\mathrm{r}} = 2.55$; for the value of $h/\lambda_0 = 0.04$ results are compared to those obtained in [60].

Error study

An error study for the modal sums is done i.e. the relative error is calculated versus the number of terms (partial sums) in two different ways for a single grounded dielectric substrate with $\varepsilon_{\mathrm{r}} = 2.55$ and $h/\lambda = 0.04$. One way is given by (3.48). Another way is given by

$$\zeta_{\mathrm{r}} = \left| \frac{S_{n+1} - S_n}{S_n} \right| \tag{3.51}$$

Without any loss of generality the source is taken to be at the origin $(x_0, y_0) = (0, 0)$ and the observer is placed at the different locations in the reference cell of dimensions $a = b = 1.1\lambda_0$. The results for the different observer positions: $(x_0, y_0) = (0.1a, 0.1b)$, $(x_0, y_0) = (0.5a, 0.5b)$, $(x_0, y_0) = (0.95a, 0.6b)$ and $(x_0, y_0) = (0.95a, 0.05b)$ are shown in Fig. 3.28–Fig. 3.31 respectively. The best error is achieved for the case in the Fig. 3.29 what is expected, since the observer point is in the center of the cell and far away from the source and its replicas. The worst results are achieved for observer positions that are close to the source as shown inFig. 3.28 and Fig. 3.31. The different means of calculating the relative error are applied in order to get insight into the difference of evaluating the relative error with the reference value as shown in (3.48) or evaluating the relative difference of the two successive partial sums, i.e. how fast the difference between partial sums vanishes.

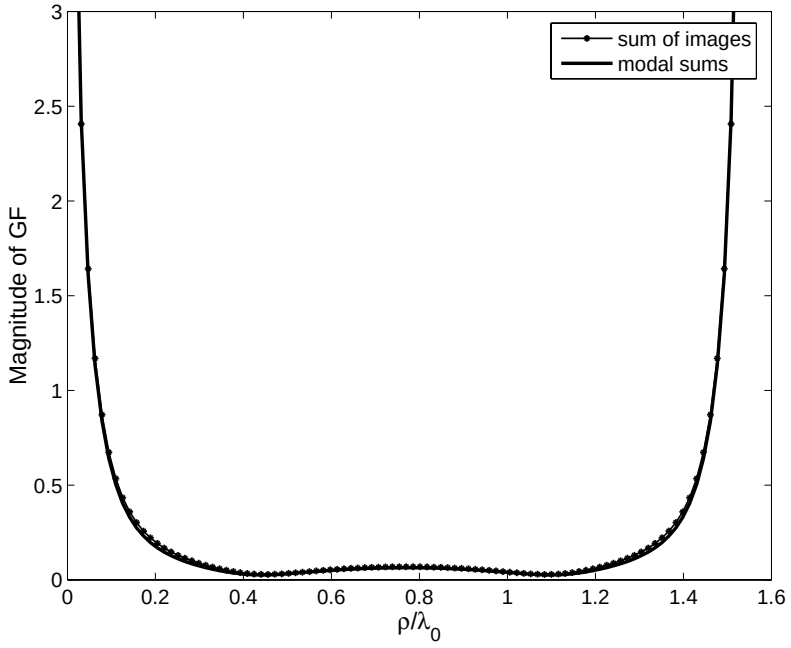

Figure 3.25: Magnitude of the periodic Green's function G_p for the charge scalar potential calculated using the Shanks' transform applied to the sum of images and the modal sums vs. normalized transverse distance ρ/λ_0 for $\varepsilon_\mathrm{r} = 1$; for the value of $h/\lambda_0 = 0.04$.

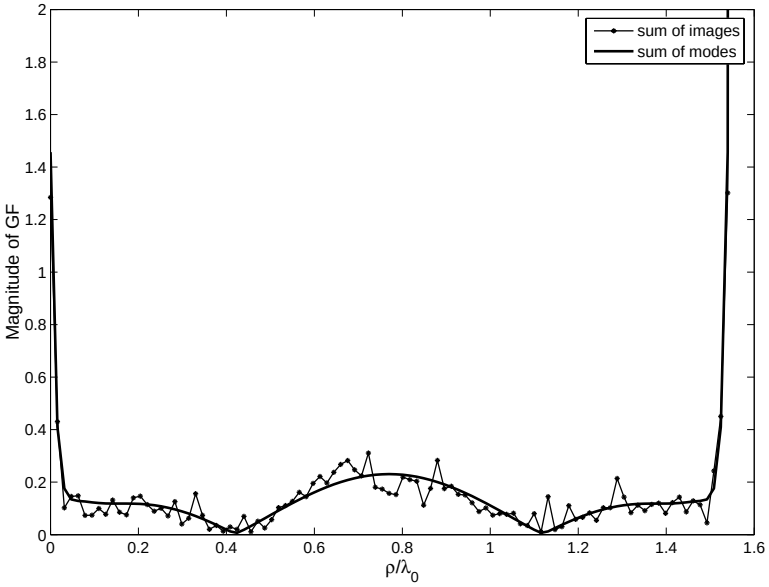

Figure 3.26: Magnitude of the periodic Green's function G_p for the charge scalar potential calculated using the Shanks' transform applied to the sum of images and the modal sums vs. normalized transverse distance ρ/λ_0 for $\varepsilon_{\mathrm{r}} = 9.8$; for the value of $h/\lambda_0 = 0.04$.

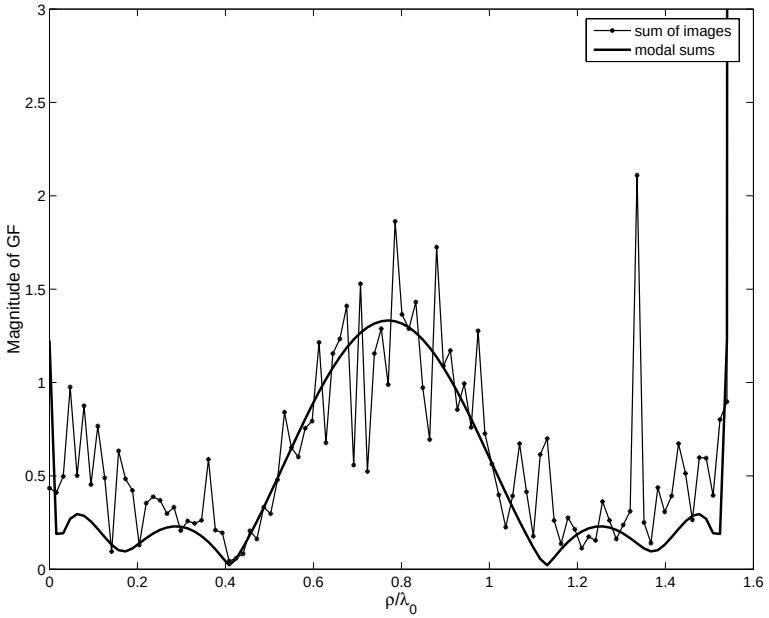

Figure 3.27: Magnitude of the periodic Green's function G_p for the charge scalar potential calculated using the Shanks' transform applied to the sum of images and the modal sums vs. normalized transverse distance ρ/λ_0 for $\varepsilon_{\mathrm{r}} = 9.8$; for the value of $h/\lambda_0 = 0.06$.

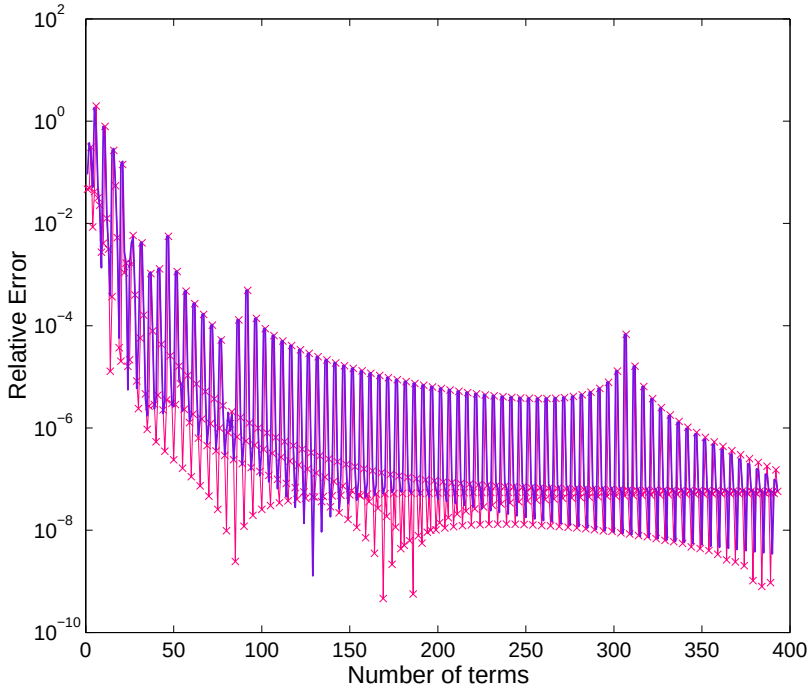

Figure 3.28: Relative error vs. number of partial sums; solid line - relative error calculated with successive terms, cross - relative error calculated with reference value; observer position $(x_0, y_0) = (0.1a, 0.1b)$.

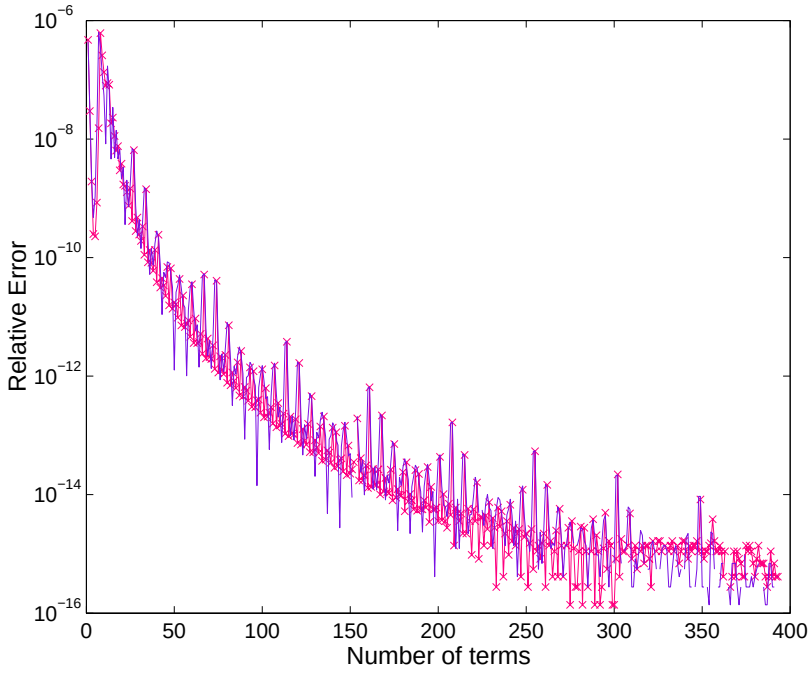

Figure 3.29: Relative error vs. number of partial sums; solid line - relative error calculated with successive terms, cross - relative error calculated with reference value; observer position $(x_0, y_0) = (0.5a, 0.5b)$.

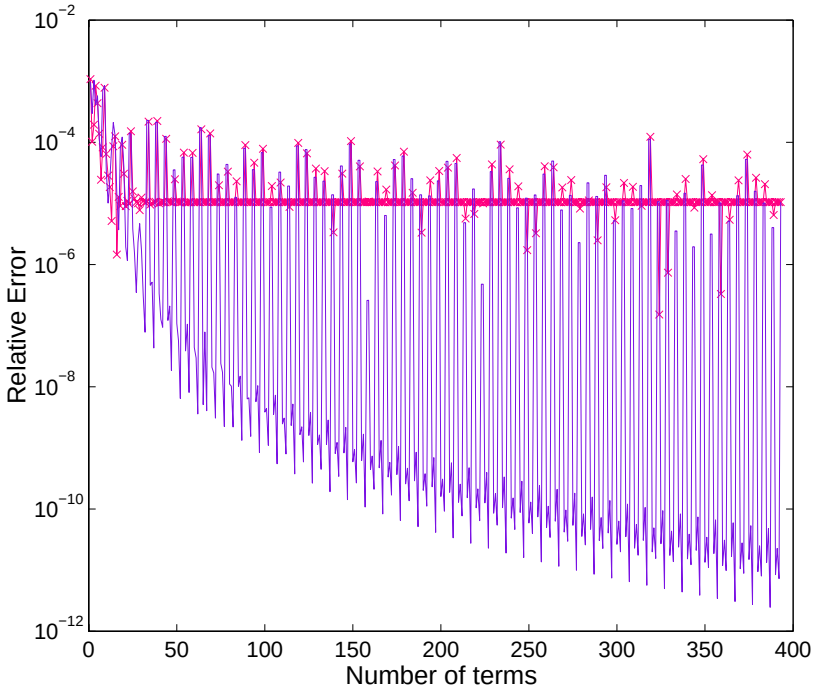

Figure 3.30: Relative error vs. number of partial sums; solid line - relative error calculated with successive terms, cross - relative error calculated with reference value; observer position $(x_0, y_0) = (0.95a, 0.6b)$.

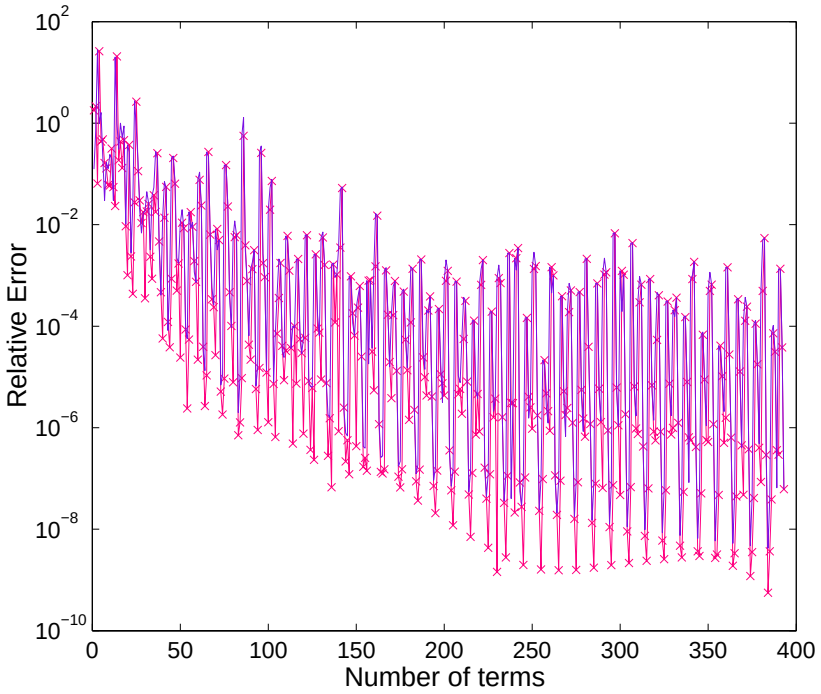

Figure 3.31: Relative error vs. number of partial sums; solid line - relative error calculated with successive terms, cross - relative error calculated with reference value; observer position $(x_0, y_0) = (0.95a, 0.05b)$.

3.4 Application of Accelerating Techniques to FSSs Canonical Case

In this section, a practical application of acceleration techniques to the evaluation of the MoM matrix is presented. An an example FSSs having unit cell in the shape of a cross is taken. The current distribution on the unit cell of periodic structure, for x-directed plane wave excitation, is obtained by three different means:

- ✓ Brute force to perform the summation in the periodic Green's functions, and truncated the sum after 151 terms in each direction.
- ✓ Shanks' transform in 2-D to speed up the convergence of the sum, and needed only 40 terms in each direction. The computation time needed for the second method is 15 times less than for the brute force approach to obtain the same precision.
- ✓ Ewald's transform used to evaluate the periodic GFs

The current distribution of the FSSs obtained by Shanks' transform is given in Fig. 3.32. The currents distributions are then evaluated by direct sum and by Ewald's transform and compared to that obtained by Shanks' transform. The difference between Shanks' transform and the direct sum evaluation is presented in Fig. 3.33(a) and the difference between Shanks' and Ewald's transform is presented in Fig. 3.33(b). It can be noted that Shanks' and Ewald's transform give the results that are closer for the order of magnitude compared to the difference of Shanks' transform and the direct sum.

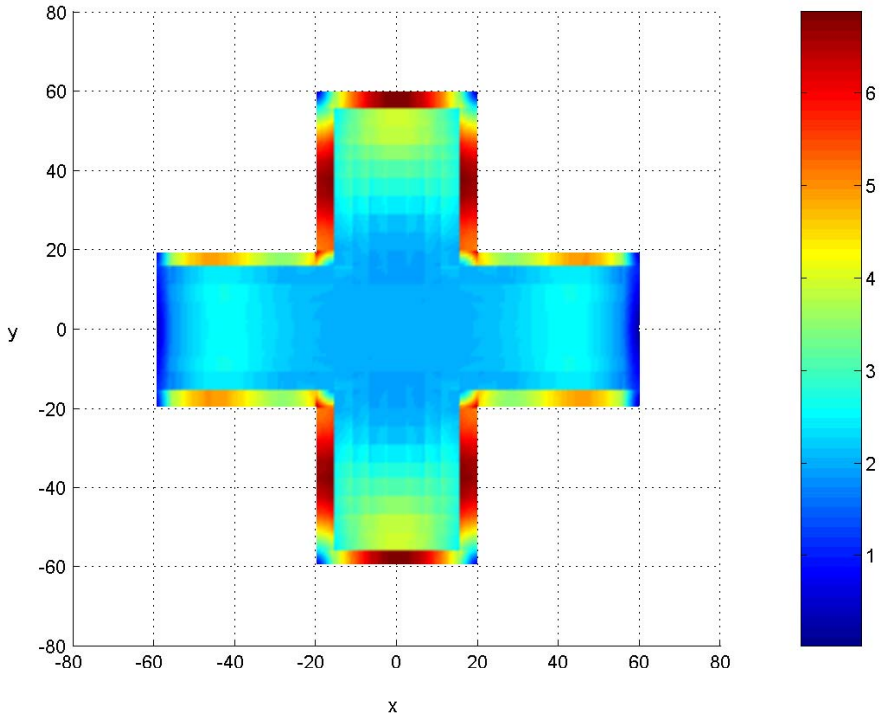

Figure 3.32: Current distribution for the free space periodic structure, with the unit cell in the shape of a cross; $\lambda = 80\text{mm}$, $f = 3747.4\text{MHz}$; periodicity of the structure given by $a = b = 128\text{mm} = 8/5\lambda$; applied accelerating technique Shanks' transform in 2-D.

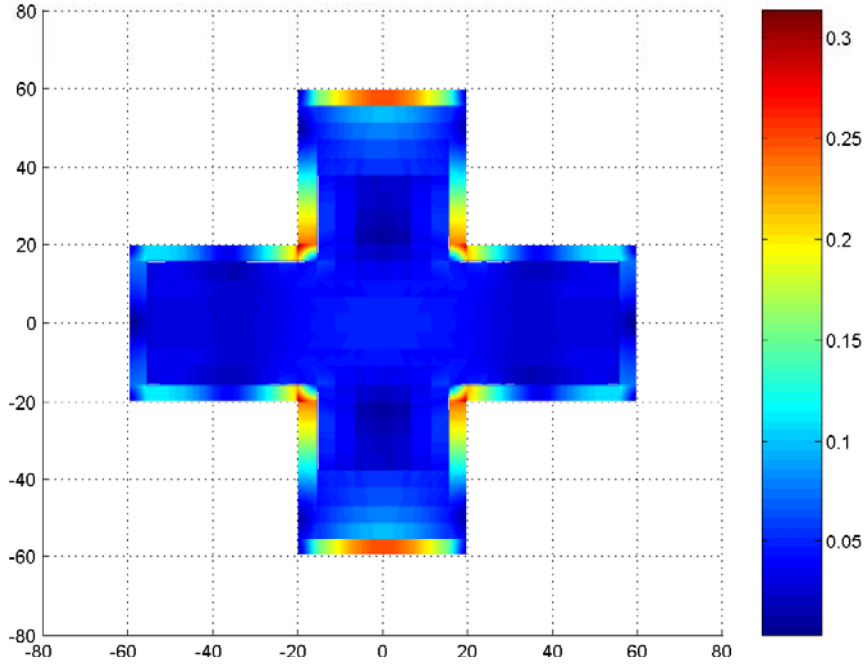

(a) Difference of the current distribution for Shanks' transform in 2-D and direct sum.

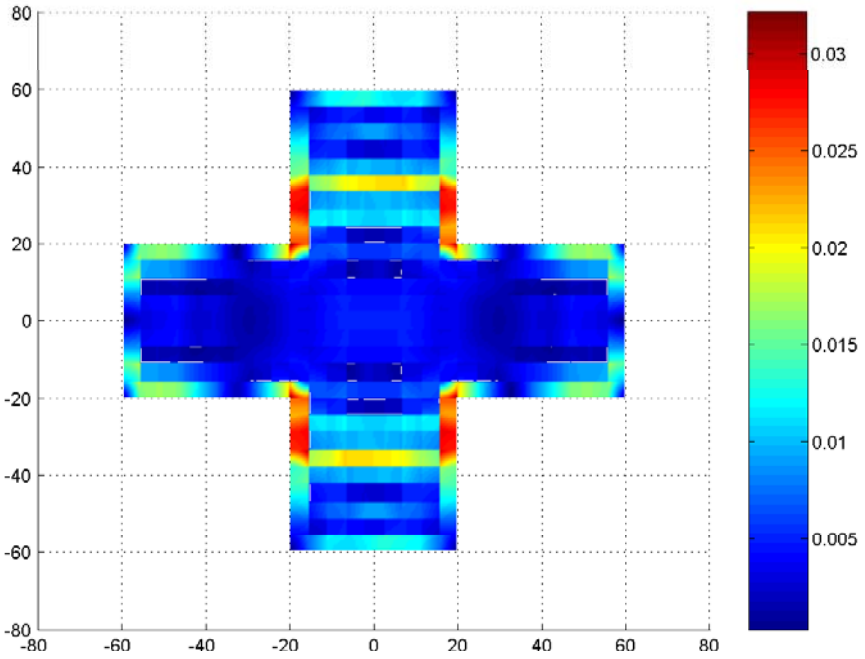

(b) Difference of the current distribution for Shanks' transform in 2-D and Ewald's transform.

Figure 3.33: Differences of currents distributions obtained by different means

3.5 Conclusions

The investigations done so far have brought significant conclusions. Results presented in 3.2.1 reveal that among all the general techniques only Shanks' transform can answer to all the variety of input parameters. Numerical simulations, without any loss of generality, are done for the same unit cell's size (i.e. periodicity) putting the point to the ability of the accelerating algorithms to approximate well the sums for the case of arbitrary plane wave incidence and arbitrary source-observer distances. It is assumed that we are not dealing with large periodic spacings of the structure that exceed few wavelengths λ. Further Shanks' transform has been applied to 2-D structures by two means:

- the double infinite sum transformed to a single 1-D infinite sum accelerated by Shanks' but did not give expected results
- Shanks' transform applied twice to the double infinite sum of the free space GF's (once in each dimension)

After a good agreement between the GF's approximations for the free-space case, obtained by Shanks algorithm and by Ewald's transform was observed, the next step was to accelerate the periodic Green's function for multilayered media. The study was done for both formulations of multilayered periodic GFs, sum of images and modal sums.

As a numerical example, a single grounded dielectric slab is taken. The simulations are performed for the dielectric permittivity $\varepsilon_{\mathrm{r}} = 9.8$ and for two different substrate thickness $h/\lambda_0 = 0.04$ and $h/\lambda_0 = 0.06$ for the last index in both partial sums equal sums equal $n = 36$. It is obvious that under the same conditions the modal sum is giving a smooth approximation of the periodic GF compared to that approximated by the sum of images. The oscillations in the sum of images, already explained in 3.3.1 by the evaluation of Sommerfeld integrals, leave the choice of modal sums to proceed further.

4 New Method for Acceleration of Multilayered Periodic Green's Function Using Shanks' and Ewald's transform

4.1 Theory basis

For developing this method the starting point is the kernel of the infinite periodic GFs calculated by the means of transmission line model [25]. First the modal sum is separated into two parts, dynamic and static part, method already known as Kummer's method [50]. Initially the dynamic sum is accelerated by the improved version of Shanks' transform while the static part being only transformed by Poisson's sum formula. The precision and gain in CPU time was still improved by the Ewald's transform applied to the static term. The MPOF could be avoided since the static term keeps the form of the free-space periodic Green's function and allows the Ewald's transform to be applied in the same manner. In the following, all the steps will be explained in details.

A single grounded dielectric slab Fig. 4.1, is taken as a numerical example. The structure

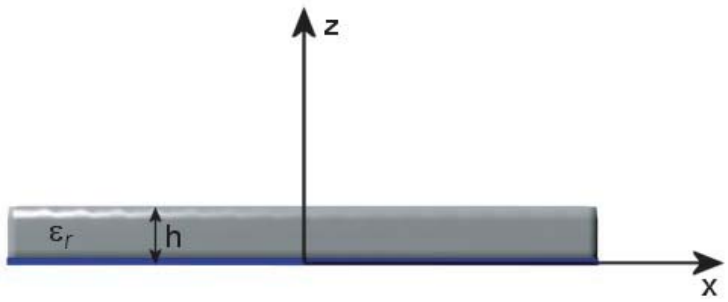

Figure 4.1: Side view of a single grounded dielectric slab.

can be represented by an equivalent transmission line model Fig. 4.2. Depending on the presence of the ground plane, the load impedance Z_{L} will be replaced with the intrinsic impedance of free space, $\eta_0 = 376.7 \approx 120\pi\,\Omega$, if the dielectric slab is not grounded or by zero in the case of a perfect ground plane below the dielectric layer. From the circuit theory we know that the voltages and currents at the end points of a transmission line can be related by the following equation written in a matrix form:

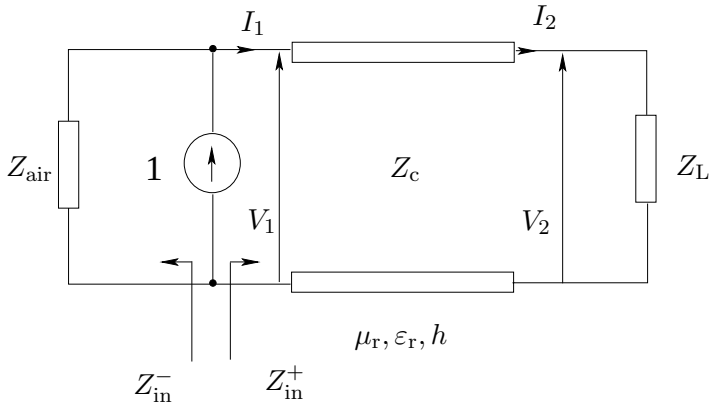

Figure 4.2: Equivalent circuit model for the structure in Fig. 4.1.

$$\begin{bmatrix} V_1 \\ I_1 \end{bmatrix} = \begin{bmatrix} \cos(uh) & \mathrm{j}Z_{\text{c}}\sin(uh) \\ \frac{1}{Z_{\text{c}}}\mathrm{j}\sin(uh) & \cos(uh) \end{bmatrix} \cdot \begin{bmatrix} V_2 \\ I_2 \end{bmatrix}$$

$$\tilde{G}_A^{xx} = \frac{V^{\text{TE}}}{\mathrm{j}\omega} \tag{4.1}$$

$$\tilde{G}_{\text{V}} = \frac{\omega}{k_\varrho^2}\left(\mathrm{j}V^{\text{TM}} + \frac{V^{\text{TE}}}{\mathrm{j}}\right) \tag{4.2}$$

where the transverse spectral variable of the periodic structure is given by

$$k_\varrho^2 = k_{xm}^2 + k_{yn}^2 = \left(k_x^{\text{i}} + \frac{2\pi m}{a_x}\right)^2 + \left(k_y^{\text{i}} + \frac{2\pi n}{b_y}\right)^2 \tag{4.3}$$

and

$$V^{\text{TE/TM}} = \frac{Z_{\text{air}}^{\text{TE/TM}} \cdot \mathrm{j}Z_{\text{c}}^{\text{TE/TM}} \tan(-\mathrm{j}uh)}{Z_{\text{air}}^{\text{TE/TM}} + \mathrm{j}Z_{\text{c}}^{\text{TE/TM}} \tan(-\mathrm{j}uh)} \tag{4.4}$$

In the previous equations the characteristic impedances for air/dielectric are given by

$$Z_{\text{c}}^{\text{TE}} = \frac{\omega\mu_{\text{r}}\mu_0}{-\mathrm{j}u} \qquad Z_{\text{air}}^{\text{TE}} = \frac{\omega\mu_0}{-\mathrm{j}u_0} \tag{4.5}$$

$$Z_{\text{c}}^{\text{TM}} = \frac{-\mathrm{j}u}{\omega\varepsilon_{\text{r}}\varepsilon_0} \qquad Z_{\text{air}}^{\text{TM}} = \frac{-\mathrm{j}u_0}{\omega\varepsilon_0} \tag{4.6}$$

and we have defined

$$u^2 = k_\varrho^2 - \varepsilon_{\text{r}}k_0^2 \qquad u_0^2 = k_\varrho^2 - k_0^2 \tag{4.7}$$

For indices $m = n = 0$ the scalar potential GF, G_V takes the form of:

$$\tilde{G}_v = M \cdot \frac{\mu_0}{\varepsilon_0^2} \cdot \frac{\mathrm{j}u_0 - u}{\varepsilon_r u u_0} \cdot \frac{1}{\left(Z_{\mathrm{air}}^{\mathrm{TM}} + \mathrm{j}Z_{\mathrm{c}}^{\mathrm{TM}} \cdot M\right)\left(Z_{\mathrm{air}}^{\mathrm{TE}} + \mathrm{j}Z_{\mathrm{c}}^{\mathrm{TE}} \cdot M\right)} \tag{4.8}$$

where $M = \tan(\mathrm{j}uh)$. In a general case, function tanh should be used but since no losses are assumed function tan is used (remark: $k_0 = \omega\sqrt{\mu_0\varepsilon_0}$). The expression for the voltage V_1 used in the expressions for the potential GF of the single layered slab without the ground plane is given by:

$$V_1^{\mathrm{TE/TM}} = \frac{Z_{\mathrm{air}}^{\mathrm{TE/TM}} \cdot Z_{\mathrm{c}}^{\mathrm{TE/TM}}\left(Z_{\mathrm{air}}^{\mathrm{TE/TM}} + \mathrm{j}Z_{\mathrm{c}}^{\mathrm{TE/TM}} \tan(-\mathrm{j}uh)\right)}{2Z_{\mathrm{air}}^{\mathrm{TE/TM}} Z_{\mathrm{c}}^{\mathrm{TE/TM}} + \mathrm{j}\tan(-\mathrm{j}uh) \cdot \left[(Z_{\mathrm{air}}^{\mathrm{TE/TM}})^2 + (Z_{\mathrm{c}}^{\mathrm{TE/TM}})^2\right]} \tag{4.9}$$

and for the grounded dielectric slab:

$$V_1 = \frac{Z_{\mathrm{air}}^{\mathrm{TE/TM}} \cdot \mathrm{j}Z_{\mathrm{c}}^{\mathrm{TE/TM}} \tan(-\mathrm{j}uh)}{Z_{\mathrm{air}}^{\mathrm{TE/TM}} + \mathrm{j}Z_{\mathrm{c}}^{\mathrm{TE/TM}} \tan(-\mathrm{j}uh)} \tag{4.10}$$

From the circuit theory it is known that the voltage V_1 can be found as $V_1 = I_1 \cdot Z_{\mathrm{in}}^{+} || Z_{\mathrm{in}}^{-}$ where the generator's impedance corresponds to that of free-space $Z_{\mathrm{in}}^{-} = 120\pi$ and the impedance Z_{in}^{+} is easily found as an input impedance of a transmission line with the load impedance $120\pi\,\Omega$ or $0\,\Omega$. After the Shanks' transform is applied to both, sum of images and modal sums, the aim was to explore a new technique that will be faster in terms of CPU time and fewer terms will be needed to achieve more accurate results. The idea was to separate singular and non-singular contributions to the total sum of the periodic GF, G_p and accelerate them separately. We must admit that the idea is not new and appears as the basis of the work of several different authors [53, 60, 61] and was effectively preceded by the Kummer's transform [50]. First step in our method was to reformulate the periodic GF as follows:

$$G_p = \frac{1}{ab} \sum_{m=-\infty}^{\infty} \sum_{n=-\infty}^{\infty} \underbrace{\left(\tilde{G}_{mn} - \tilde{G}_{mn}^{a}\right) \mathrm{e}^{-\mathrm{j}k_{xm}(x-x')} \mathrm{e}^{-\mathrm{j}k_{yn}(y-y')}}_{\text{dynamic}} + \frac{1}{ab} \sum_{m=-\infty}^{\infty} \sum_{n=-\infty}^{\infty} \underbrace{\tilde{G}_{mn}^{a} \mathrm{e}^{-\mathrm{j}k_{xm}(x-x')} \mathrm{e}^{-\mathrm{j}k_{yn}(y-y')}}_{\text{static}} \tag{4.11}$$

It is important to mention that all the further calculations are done for the case of vector potential periodic Green's function. The double infinite sum is transformed into the sum of "dynamic" part and the "static" part that contains the singular contribution. When the static part is determined it is subtracted from the original sum and added at once. The improved version of the Shanks' cross-rule is then applied to the dynamic part of the sum, and what is left is to accelerate the static part in terms of modal sums. This new double sum is further transformed to the spatial domain that provides the implementation of the Ewald's transform

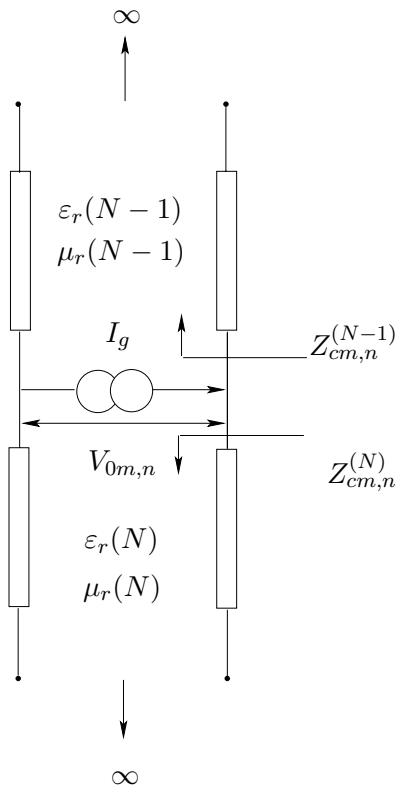

Figure 4.3: Transverse equivalent network representation used to obtain the static spectral domain GF [25].

in same way it was done before for the free-space periodic Green's function.

4.2 Calculation of the Static Part

We consider the case of a mode infinitely below the cut-off, it means that it cannot propagate along the transmission line. In such case, the mode is attenuated before it arrives to the first dielectric interface, so that the equivalent network for the static part of the spectral domain Green's function is composed of only two infinite transmission line sections, above and below the exciting generator [25]. The static voltage $V_{0m,n}$ can now be computed in the equivalent circuit Fig. 4.3 with current generator $I_g = 1\,A$ where $(N-1)$ and N denote the substrate layers above and below the source respectively. The source level is taken as a reference and $(N-1)$ and N are substrate layers above and below the source, respectively. The "static" voltage becomes now:

$$V_{0_{m,n}} = Z_{c_{m,n}}^{N-1} || Z_{c_{m,n}}^{N} = \frac{Z_{c_{m,n}}^{N-1} \cdot Z_{c_{m,n}}^{N}}{Z_{c_{m,n}}^{N-1} + Z_{c_{m,n}}^{N}} \tag{4.12}$$

In a further text the indices m, n as well as $N, N-1$ will be omitted to simplify the notation without any loss of generality.

$$Z_{\mathrm{c}}^{TE} = \frac{\omega\mu_0\mu_{\mathrm{r}}}{-\mathrm{j}u} \qquad Z_{\mathrm{c}}^{TM} = \frac{-\mathrm{j}u}{\omega\varepsilon_0\varepsilon_{\mathrm{r}}} \tag{4.13}$$

where u is given by $u^2 = k_\varrho^2 - \varepsilon_{\mathrm{r}}\mu_{\mathrm{r}}k_0^2$. Under these assumptions and after some algebraic manipulations [25], the static voltage coefficient take the following values for both TE and TM cases

$$V_{0_{m,n}}^{TE} = \frac{\mathrm{j}\mathrm{d}\omega^{\mathrm{TE}}}{k_{\varrho_{m,n}}} \qquad V_{0_{m,n}}^{\mathrm{TM}} = \frac{k_{\varrho_{m,n}}}{\mathrm{j}\mathrm{d}\omega^{\mathrm{TM}}} \qquad \text{where} \tag{4.14}$$

$$\mathrm{d}\omega^{\mathrm{TE}} = \omega\mu_0 M(s) \qquad \mathrm{d}\omega^{\mathrm{TM}} = \omega\varepsilon_0 E(s) \qquad \text{and} \tag{4.15}$$

$$M(s) = \frac{\mu_{\mathrm{r}}(N)\mu_{\mathrm{r}}(N-1)}{\mu_{\mathrm{r}}(N) + \mu_{\mathrm{r}}(N-1)} \qquad E(s) = \varepsilon_{\mathrm{r}}(N-1) + \varepsilon_{\mathrm{r}}(N). \tag{4.16}$$

where s being a corresponding generic layer in the transmission line. Knowing that

$$\tilde{G}_A^{xx} = \frac{V^{\mathrm{TE}}}{\mathrm{j}\omega} \qquad \text{and} \qquad V_0^{\mathrm{TE}} = \frac{\mathrm{j}\omega\mu_0 M(s)}{k_{\varrho_{m,n}}} \tag{4.17}$$

the following expression for the static term kernel is obtained

$$\tilde{G}_{A_0}^{xx} = \frac{V_0^{\mathrm{TE}}}{\mathrm{j}\omega} = \frac{\mu_0 M(s)}{k_{\varrho_{m,n}}} = \frac{\mu_0}{2k_{\varrho_{m,n}}} \tag{4.18}$$

Let us see the way $u = k_{\varrho_{m,n}}$ is computed: it is valid for $m, n \longrightarrow \infty$, that is, for the static case. Practically, it means that in the schema Fig. 4.3 input impedance $Z_{\mathrm{c}_{m,n}}$ sees an open line. In the expression

$$u^2 = k_{\varrho_{m,n}}^2 = k_\varrho^2 - \varepsilon_r\mu_r k_0^2 \tag{4.19}$$

nothing will change if the same term is added and subtracted on the right side as

$$u^2 = k_{\varrho_{m,n}}^2 = k_\varrho^2 + U^2 - (\varepsilon_{\mathrm{r}}\mu_{\mathrm{r}}k_0^2 + U^2) \tag{4.20}$$

and for the condition $m, n \longrightarrow \infty$ it is easy to observe that

$$k_{\varrho_{m,n}} \gg k_0 \tag{4.21}$$

and for that reason, the term $\varepsilon_r\mu_r k_0^2$ in the (4.19) can be omitted. Introducing the smoothing parameter U the problems that would occur for $m = n = 0$ and the normal plane wave incidence are avoided [50]. Finally, the denominator in (4.18) looks like

$$k_{\varrho_{m,n}}^2 \approx k_{xm}^2 + k_{yn}^2 + U^2 = k_\varrho^2 + U^2 \tag{4.22}$$

4.2.1 Applying Ewald's Transform to the Static GF

As already mentioned, our periodic infinite GF, G_p can be rewritten as a sum of two parts, the dynamic and the static parts. For the dynamic part of the sum the problem of convergence is treated applying the improved version of a cross-rule Shanks' algorithm. What is left is to explain the solution of the static sum convergence problem. Let us rewrite once more the sum that is now focus of our interest

$$\tilde{G}_{p0} = \frac{1}{ab} \sum_{m=-\infty}^{\infty} \sum_{n=-\infty}^{\infty} \frac{1}{2k_{\varrho mn}} \mathrm{e}^{-k_{\varrho mn}|z-z'|} \mathrm{e}^{-\mathrm{j}k_{xm}(x-x')} \mathrm{e}^{-\mathrm{j}k_{yn}(y-y')}. \tag{4.23}$$

The "on-plane" case, i.e. $z = z'$, will be assumed to simplify the mathematics. That will practically result in replacing the term $\mathrm{e}^{-k_{\varrho mn}|z-z'|}$ by 1. Applying the Poisson's sum transformation

$$\sum_{m,n} G(x - ma, y - nb) = \frac{1}{ab} \sum_{m,n} \tilde{G}\big(\frac{2m\pi}{a}, \frac{2n\pi}{b}\big) \mathrm{e}^{\mathrm{j}\frac{2m\pi}{a}x} \mathrm{e}^{\mathrm{j}\frac{2n\pi}{b}y} \tag{4.24}$$

to (4.23) yields

$$G_{p0} = \frac{1}{4\pi} \sum_{m=-\infty}^{+\infty} \sum_{n=-\infty}^{+\infty} \frac{\mathrm{e}^{-UR_{mn}}}{R_{mn}} \mathrm{e}^{\mathrm{j}2\pi ma} \mathrm{e}^{\mathrm{j}2\pi nb} \tag{4.25}$$

$$\text{where} \quad R_{mn} = \sqrt{(x - x' - ma)^2 + (y - y' - nb)^2} \tag{4.26}$$

So, finally (4.11) can be written as follows

$$G_p = \frac{1}{ab} \sum_{m=-\infty}^{+\infty} \sum_{n=-\infty}^{+\infty} \Big(\tilde{G}_A^{xx} - \tilde{G}_{A0}^{xx}\Big) \mathrm{e}^{-\mathrm{j}k_{xm}(x-x')} \mathrm{e}^{-\mathrm{j}k_{yn}(y-y')} + \frac{1}{4\pi} \sum_{m=-\infty}^{+\infty} \sum_{n=-\infty}^{+\infty} \mathrm{e}^{\mathrm{j}2\pi(ma+nb)} \frac{\mathrm{e}^{UR_{mn}}}{R_{mn}} \tag{4.27}$$

Equation (4.27) is derived form the equation (4.11) by adding and subtracting spatial and spectral representation, respectively, of the free-space GF for a medium with imaginary wave number $k = -\mathrm{j}U \quad (U = \mathrm{j}k)$. The U is a smoothing parameter and it will smooth the approximate of the series as a function of m and n. As a consequence, its Fourier transform (appearing in the last term of (4.27)) decays exponentially for large values of the transform variables. A reasonable choice for U which seems to ensure good convergence for both spatial and spectral sum in (4.27) is about half size of the maximum reciprocal lattice base vector $\frac{2\pi}{a}/2 = \frac{\pi}{a}$ [50]. One of the consequences of the acceleration techniques application is to isolate the proper singularity in the sum to the $m = 0, n = 0$ term of the last series in (4.27). The term is

$$\frac{\mathrm{e}^{UR_{00}}}{4\pi R_{00}} \quad \xrightarrow{R_{00} \to 0} \quad \frac{1}{4\pi R_{00}} \tag{4.28}$$

where R_{00} is the distance between the source point at the origin $(0, 0)$ of the unit cell and the observation point. In the MoM application it may be handled just as a free-space point source GF. This step is not necessary in our case since the Ewald transform is used to further enhance the convergence of the last series in (4.27). The double infinite sum whose convergence will

be enhanced further by Ewald's transform and is expressed as following

$$\tilde{G}_{p0} = \frac{1}{ab} \sum_{m=-\infty}^{+\infty} \sum_{n=-\infty}^{+\infty} \tilde{G}_{A0}^{xx} \mathrm{e}^{-k_{\varrho mn}|z-z'|} \mathrm{e}^{-\mathrm{j}k_{xm}(x-x')} \mathrm{e}^{-\mathrm{j}k_{yn}(y-y')} \tag{4.29}$$

where the kernel of the series (4.29) is given by

$$\tilde{G}_{A0}^{xx} = \frac{\mu_0}{2} \frac{1}{k_{\varrho mn}} \qquad \text{and} \qquad k_{\varrho mn}^2 = k_{xm}^2 + k_{yn}^2 + U^2 \tag{4.30}$$

Without loss of generality, we can drop μ_0, since it only suggests that we deal with the vector potential, and applying the Poisson's sum formula to the rest of the sum (4.30) we obtain

$$\frac{1}{4\pi} \sum_{m=-\infty}^{+\infty} \sum_{n=-\infty}^{+\infty} \mathrm{e}^{\mathrm{j}k_x^i ma} \mathrm{e}^{\mathrm{j}k_y^i nb} \quad \frac{\mathrm{e}^{-UR_{mn}}}{R_{mn}} \tag{4.31}$$

Without loosing generality the indices m, n can be replaced by $-m, -n$ since in both sums they are taking all the integer values from $-\infty$ till ∞ . Now the equation (4.31) is the same as

$$\Psi = \frac{1}{4\pi} \sum_{m,n} \frac{\mathrm{e}^{-\mathrm{j}kR_{mn}}}{R_{mn}} \quad \mathrm{e}^{-\mathrm{j}mk_x^i a} \mathrm{e}^{-\mathrm{j}nk_y^i b} \tag{4.32}$$

used as a starting point in Ewald's transform calculation in a free-space case, save for the $\mathrm{j}k$ that becomes a smoothing parameter U in the case of the static sum. We can proceed with Ewald's transform in a similar manner as in the case of free-space GFs. An assumption $z = z'$ is introduced to simplify the expression for R_{mn} since our calculations will be performed for source and observer being on the same z level. Furthermore, in the identity

$$\frac{\mathrm{e}^{-\mathrm{j}kR}}{R} = \frac{2}{\sqrt{\pi}} \int_0^\infty \mathrm{e}^{-R^2 s^2 + \frac{k^2}{4s^2}} \mathrm{d}s \tag{4.33}$$

replacing $\mathrm{j}k$ by U becomes

$$\frac{\mathrm{e}^{-UR}}{R} = \frac{2}{\sqrt{\pi}} \int_0^\infty \mathrm{e}^{-R^2 s^2 - \frac{U^2}{4s^2}} \mathrm{d}s \tag{4.34}$$

introducing the parameter $E = \sqrt{\pi/ab}$ to split the integral path one obtains $\Psi = \Psi_1 + \Psi_2$

$$\Psi_1 = \frac{1}{4\pi} \sum_{m,n} \mathrm{e}^{-\mathrm{j}mk_x^i a} \mathrm{e}^{-\mathrm{j}nk_y^i b} \frac{2}{\sqrt{\pi}} \int_0^E \mathrm{e}^{-R^2 s^2 - \frac{U^2}{4s^2}} \mathrm{d}s \tag{4.35}$$

$$\Psi_2 = \frac{1}{4\pi} \sum_{m,n} \mathrm{e}^{-\mathrm{j}mk_x^i a} \mathrm{e}^{-\mathrm{j}nk_y^i b} \frac{2}{\sqrt{\pi}} \int_E^\infty \mathrm{e}^{-R^2 s^2 - \frac{U^2}{4s^2}} \mathrm{d}s \tag{4.36}$$

Let us see what we obtain for Ψ_2. Taking into account the identity

$$\frac{2}{\sqrt{\pi}}\int_r^\infty \mathrm{e}^{-p^2s^2+\frac{q^2}{4s^2}}\mathrm{d}s = \frac{1}{2p}\Big(\mathrm{e}^{-\mathrm{j}pq}\mathrm{erfc}\big(pr-\frac{\mathrm{j}q}{2r}\big)+\mathrm{e}^{-\mathrm{j}pq}\mathrm{erfc}\big(pr+\frac{\mathrm{j}q}{2r}\big)\Big) \tag{4.37}$$

and replacing $p = R_{mn} > 0$, $q = k = -\mathrm{j}U$, $r = E$ equation (4.36) becomes

$$\Psi_2 = \frac{1}{8\pi}\sum_{m,n}\frac{\mathrm{e}^{-\mathrm{j}k_x^i ma}\mathrm{e}^{-\mathrm{j}k_y^i nb}}{R_{mn}}\Big[\mathrm{e}^{-UR_{mn}}\mathrm{erfc}\big(R_{mn}E-\frac{U}{2E}\big)+\mathrm{e}^{UR_{mn}}\mathrm{erfc}\big(R_{mn}E+\frac{U}{2E}\big)\Big] \tag{4.38}$$

which rewritten in a more compact form gives

$$\Psi_2 = \frac{1}{8\pi}\sum_{m,n}\frac{\mathrm{e}^{-\mathrm{j}k_{xi} ma}\mathrm{e}^{-\mathrm{j}k_{yi} nb}}{R_{mn}}\sum_{\pm}\mathrm{e}^{\pm UR_{mn}}\mathrm{erfc}\big(R_{mn}E\pm\frac{U}{2E}\big) \tag{4.39}$$

The calculation of Ψ_1 is less trivial. The equation (4.36) can be rewritten in the following form

$$\Psi_1 = \frac{1}{4\pi}\int_0^E \frac{2}{\pi}\mathrm{e}^{-\frac{U^2}{4s^2}}\mathrm{d}s\sum_{m,n}\mathrm{e}^{-R^2s^2-\mathrm{j}mk_{xi}a-\mathrm{j}nk_{yi}b} \tag{4.40}$$

that allows the application of the Poisson's sum formula

$$\sum_{m,n} f(x-x'-ma, y-y-nb, z-z')\mathrm{e}^{-\mathrm{j}mk_x^i a}\mathrm{e}^{-\mathrm{j}nk_y^i b} = \frac{1}{ab}\sum_{m,n}\tilde{f}(k_{xm},k_{yn})\mathrm{e}^{\mathrm{j}k_{xm}(x-x')}\mathrm{e}^{\mathrm{j}k_{yn}(y-y')} \tag{4.41}$$

to be easily implemented for the sum in (4.40)

$$\sum_{m,n}\mathrm{e}^{-R_{mn}^2s^2}\mathrm{e}^{-\mathrm{j}mk_x^i a}\mathrm{e}^{-\mathrm{j}nk_y^i b} \tag{4.42}$$

After some algebra, Ψ_1 can be presented as follows

$$\Psi_1 = \frac{1}{8ab}\sum_{m,n}\frac{\mathrm{e}^{\mathrm{j}k_{xm}(x-x')}\mathrm{e}^{\mathrm{j}k_{yn}(y-y')}}{\alpha_{mn}}\sum_{\pm}\mathrm{e}^{\pm\alpha_{mn}(z-z')}\mathrm{erfc}\big(\frac{\alpha_{mn}}{E}\pm(z-z')E\big) \tag{4.43}$$

As previously mentioned, the source and the observer being on the same level implies $z-z'=0$ and therefore $\mathrm{e}^{\pm 2\alpha_{mn}(z-z')}=1$. For the static sum α_{mn} reduces to

$$\alpha_{mn}^2 = \frac{1}{4}\big(k_{xm}^2+k_{yn}^2-k^2\big) = \frac{1}{4}\big(k_{xm}^2+k_{yn}^2+U^2\big) \tag{4.44}$$

$$\alpha_{mn} = \frac{1}{2}\sqrt{k_{xm}^2+k_{yn}^2+U^2} \Longrightarrow \alpha_{mn} = \frac{k_{\varrho_{mn}}}{2} \tag{4.45}$$

Finally Ψ_1 can be reformulated in more compact form that will used in our application

$$\Psi_1 = \frac{1}{2\Omega} \sum_{m,n=-\infty}^{\infty} \frac{\mathrm{e}^{\mathrm{j}k_{xm}(x-x')} \mathrm{e}^{\mathrm{j}k_{yn}(y-y')}}{k_{\varrho_{mn}}} \mathrm{erfc}\big(\frac{k_{\varrho_{mn}}}{2E}\big) \tag{4.46}$$

4.2.2 Calculation of the Residuum

One way to check the validity of our method is to compare the value of the residuum obtained analytically and numerically. Effectively it is easy to calculate its value analytically, since it is obtained as a product of the absolute value of the source-observer distance when the same is reaching an infinitesimal small value and the GF which tends to ∞. Analytical observations show that the "responsible" for the residuum is the sum Ψ_2 (4.39), of the Ewald's treated static part of the total sum G_p. Assuming $m = n = 0$ in (4.39), and multiplying Ψ_2 with ϱ when $\varrho \longrightarrow 0$ we end up with

$$Res = \lim_{\varrho \to 0} \varrho \Psi_2 \Big|_{m=n=0} = \frac{1}{8\pi} \varrho \cdot \frac{\mathrm{e}^{-\mathrm{j}k_x^i ma} \mathrm{e}^{-\mathrm{j}k_y^i nb}}{R_{00}} \Big(\mathrm{erfc}\big(\frac{U}{E}\big) + \mathrm{erfc}\big(-\frac{U}{E}\big) \Big) \tag{4.47}$$

$$\text{where} \quad \varrho = \sqrt{(x-x')^2 + (y-y')^2} = R_{00} \tag{4.48}$$

and the concrete value $Res = 0.0796$ and for periodicity $a = b = 1.1\lambda$. The same value is obtained numerically when the values $m = n = 0$ are passed in G_p and our Green's function is multiplied with $\varrho \to 0$, Fig. 4.4. This step was done to confirm agreement between the theory and the numerical code.

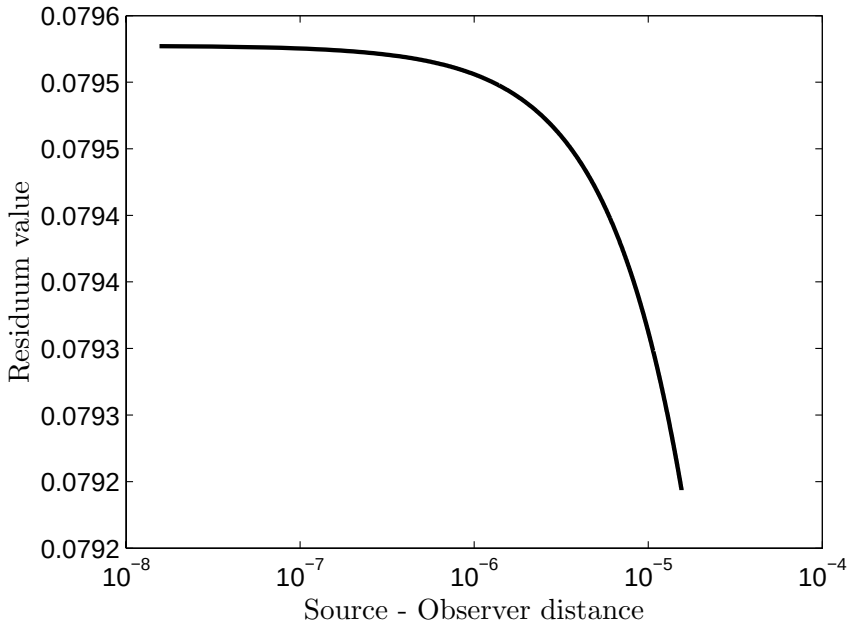

Figure 4.4: Residuum via Shanks' and Ewald's transform.

4.2.3 Ewald's Transform vs. Modal Static Term

The usefulness of applying Ewald's transform on the static part of the sum G_p that is initially given in terms of modal sums, is simply illustrated in Fig. 4.5. The sum of modes will at $\varrho = 0$ converge very slow, while the Ewald's transform takes into account this singularity perfectly. The experiments are done for a single dielectric grounded structure with the permittivity $\varepsilon_r = 9.8$, slab thickness $h = 0.06\lambda_0$, periodicity $a = b = 1.1\lambda_0$ at frequency $f = 30$GHz. The source is placed at the origin $(0, 0)$ and the observer is changing the position along the cell's diagonal. The number of terms taken in the direct sum is $(2 \cdot 76 + 1)^2 = 23409$ while for Ewald's transform the number is $(2 \cdot 2 + 1)^2 = 25$. It is important to underline that under these circumstances smooth function is obtained only in Ewald's case, Fig. 4.6.

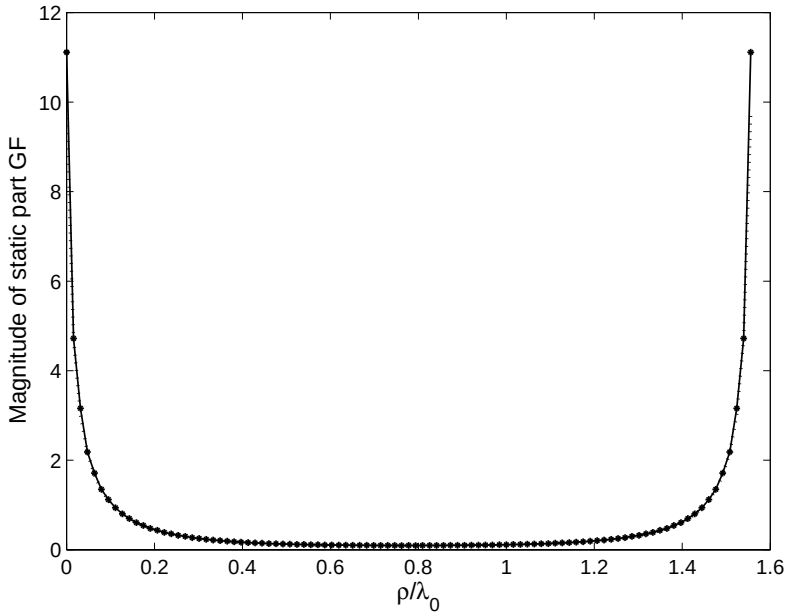

Figure 4.5: Quasi Static part calculated as sum of modes - solid line with asterisk; by the means of Ewald - dotted line.

4.2.4 Ewald vs. Poisson's Transform

The next study was done to demonstrate the advantages of the Ewald's transform over the often applied Poisson's summation formula to the extracted part of the series (4.11), specially in terms of accuracy. The relative error is calculated versus the number of terms taken in partial sums and the curves are plotted for two different positions of the observer, the source being placed at the origin $(0, 0)$. The other parameters are the same as in subsection 4.2.1. The solid line presents results for the observer being at a distance $0.5\sqrt{2}a\lambda$ on the unit cell's diagonal, from the source. In terms of concrete values approximate the (4.29) means that,

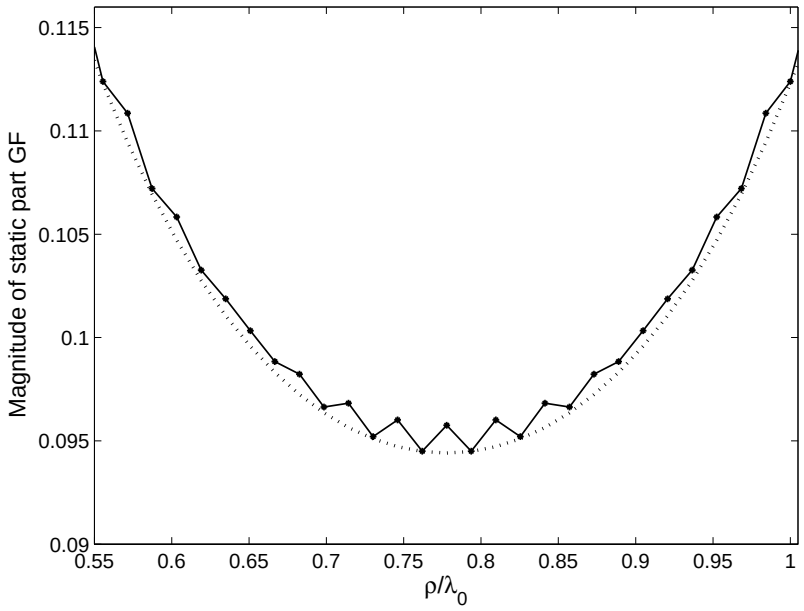

Figure 4.6: Quasi Static part calculated as sum of modes - solid line with asteriks; by the means of Ewald - dotted line (same as Fig. 4.5 just zoomed).

for example with the Poisson's summation formula $(2 \cdot 5 + 1)^2 = 121$ terms need to be taken in order to achieve accuracy in a first 6 digits, while in a case of the Ewald's transform even taking only $(2 \cdot 2 + 1)^2 = 25$ terms the two neighboring sums do agree in 8 significant digits. The dotted line with asteriks gives the data for the observer being close to the source at the distance $0.001\sqrt{2}a\lambda$ on the cell's diagonal i.e. close to the singularity Fig. 4.7. The same analysis gives that in Posson's sum to obtain accuracy in 8 first digits $(2 \cdot 4 + 1)^2 = 81$ terms must be taken, while with the Ewald's transform taking only the first partial sum will do the sums equal in 7 significant digits while taking only one more partial sum the successive sums are completely equal (15 digits after decimal point!).

4.3 Discussion of Results

A small numerical experiment is provided to show the behavior of the GF versus the number of partial sums/terms to approximate the dynamic part (Shanks' transformation applied), static part (Ewald's transformation applied) and complete sum G_p (Shanks' transformation applied). The dynamic and the static sum together give contribution to the final value of the periodic GF. It is evident that even taking hundreds of the partial sums will not be enough in case of Shanks' transformation applied to the total sum G_p to stop oscillating while in case of static and dynamic part roughly speaking not more that 30 partial sums in the dynamic part will be needed to achieve "smooth" approximation, while for the static part only one terms

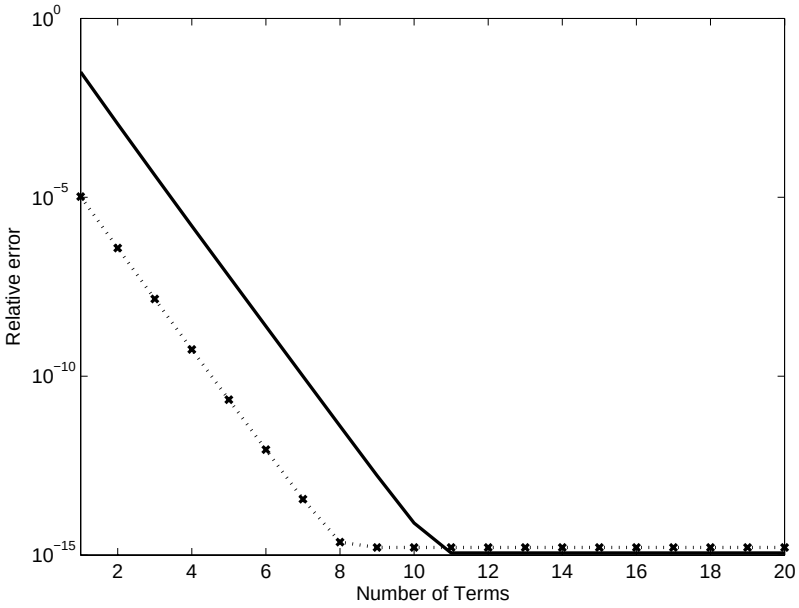

Figure 4.7: Relative error versus number of terms in the Poisson transform of the series (4.29) where solid line means observer position in the middle of the unit cell and dotted line means observer position close to source.

is enough. Time study reveals that taking 76 partial sums in case of Shanks' transformation alone, what is shown to be about a minimum terms to obtain acceptable approximations, the CPU time needed is about 25 more than in case of our method where 2 partial sums were taken in Ewald's transform and 16 in the Shanks' transform applied to the dynamic sum.

4.4 Terms and Time Study

This study and the accompanying figures are done with the intention to demonstrate how the number of terms affects the periodic Green's function behavior when the Shanks' transformation is applied to the complete GF, to the dynamic part only, the Ewald's transform applied to the static part and our method which combines the Shanks' and the Ewald's transformation. In Fig. 4.8–Fig. 4.11 the same colors are used to designate different curves that correspond to different source-observer distances. Red - $\varrho = 0.001a_x\lambda_0\sqrt{2}$; black - $\varrho = 0.01a_x\lambda_0\sqrt{2}$; pink - $\varrho = 0.5a_x\lambda_0\sqrt{2}$; blue - $\varrho = 0.4a_x\lambda_0\sqrt{2}$; green - $\varrho = 0.25a_x\lambda_0\sqrt{2}$; orange - $\varrho = 0.1a_x\lambda_0\sqrt{2}$.

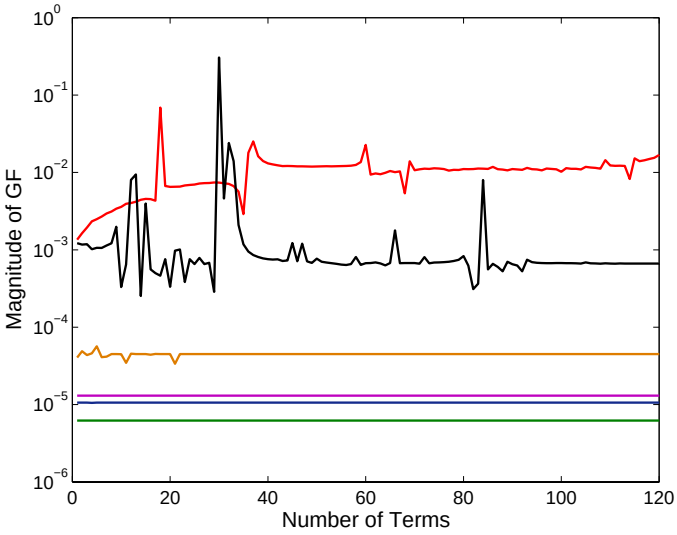

Figure 4.8: Magnitude of Green's function versus number of partial sums when Shanks' cross rule applied to the entire double sum Red - $\varrho = 0.001a_x\lambda_0\sqrt{2}$; black - $\varrho = 0.01a_x\lambda_0\sqrt{2}$; pink - $\varrho = 0.5a_x\lambda_0\sqrt{2}$; blue - $\varrho = 0.4a_x\lambda_0\sqrt{2}$; green - $\varrho = 0.25a_x\lambda_0\sqrt{2}$; orange - $\varrho = 0.1a_x\lambda_0\sqrt{2}$.

The CPU time is calculated for both, Shanks cross rule applied to the entire periodic GF and for our method, and compared. Numerical experiments are done for the source placed at the origin $(0, 0)$ without loss of generality and the observer moving along the unit cell's diagonal. The GF values were calculated in 100 different points along the diagonal. We find this time study more reliable than those of [61] since calculating the time only for a specific source-observer distance will vary depending on the proximity of the source, while in our case the source-observer distance sweep all the values that would appear in the calculations of the complete GF over the whole cell where the number of terms should be taken

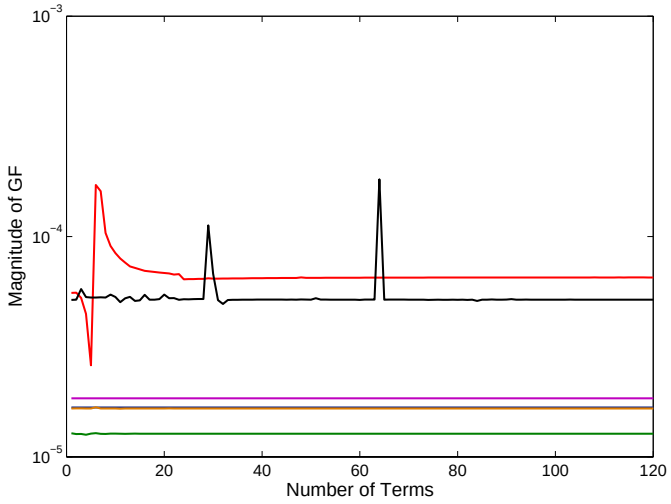

Figure 4.9: Magnitude of Green's function versus number of partial sums when Shanks' cross rule applied to the dynamic part of the double sum Red - $\varrho = 0.001a_x\lambda_0\sqrt{2}$; black - $\varrho = 0.01a_x\lambda_0\sqrt{2}$; pink - $\varrho = 0.5a_x\lambda_0\sqrt{2}$; blue - $\varrho = 0.4a_x\lambda_0\sqrt{2}$; green - $\varrho = 0.25a_x\lambda_0\sqrt{2}$; orange - $\varrho = 0.1a_x\lambda_0\sqrt{2}$.

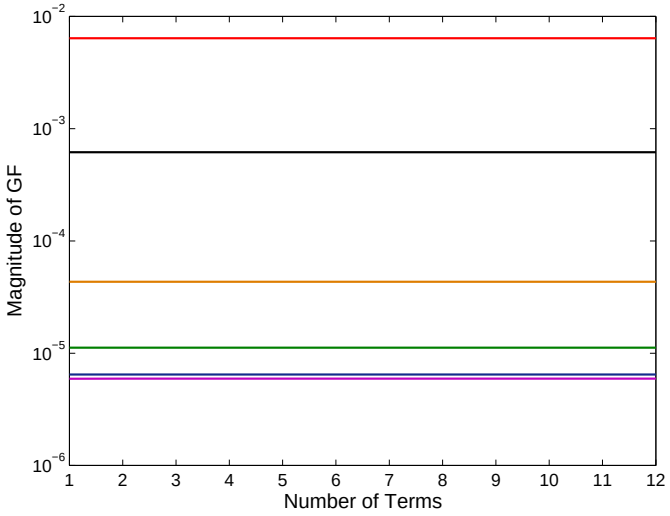

Figure 4.10: Magnitude of Green's function versus number of partial sums when Ewald's transform applied to the static part of the double sum Red - $\varrho = 0.001a_x\lambda_0\sqrt{2}$; black - $\varrho = 0.01a_x\lambda_0\sqrt{2}$; pink - $\varrho = 0.5a_x\lambda_0\sqrt{2}$; blue - $\varrho = 0.4a_x\lambda_0\sqrt{2}$; green - $\varrho = 0.25a_x\lambda_0\sqrt{2}$; orange - $\varrho = 0.1a_x\lambda_0\sqrt{2}$.

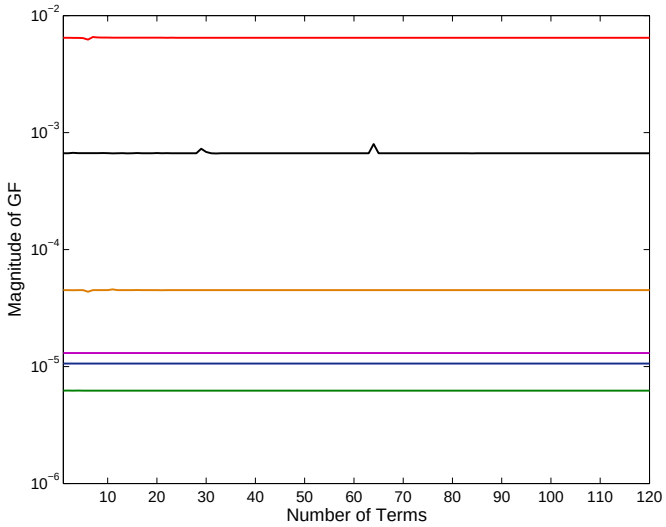

Figure 4.11: Magnitude of Green's function versus number of partial sums when our method applied to the entire double sum Red - $\varrho = 0.001 a_x \lambda_0 \sqrt{2}$; black - $\varrho = 0.01 a_x \lambda_0 \sqrt{2}$; pink - $\varrho = 0.5 a_x \lambda_0 \sqrt{2}$; blue - $\varrho = 0.4 a_x \lambda_0 \sqrt{2}$; green - $\varrho = 0.25 a_x \lambda_0 \sqrt{2}$; orange - $\varrho = 0.1 a_x \lambda_0 \sqrt{2}$.

according to the worst case scenario (singularity case). Time needed for our method was 50 times less than the time needed for Shanks' transform. In a case of our method 70 partial sums were taken in a dynamic sum and 2 for the static sum, while in Shanks' transform 350 partial sums were taken. In both methods the worst case is considered and for that reason the maximum number of partial sums taken to ensure good convergence in a singular region. On a Pentium (R) 3.2GHz and 1.99GB RAM time needed for the Shanks' transformation was $337.3125s$, and for our method $6.656250s$. Keeping the same parameters $\varepsilon_{\mathrm{r}} = 2.1, f = 30\mathrm{GHz}, \lambda = 10\mathrm{mm}, a = b = 11\mathrm{mm} = 1.1\lambda$ the time was compared for 2 different source-observer distances $\varrho_1 = 0.78\lambda$ and $\varrho_2 = 1.54\lambda$ that correspond to the scenario source-observer far-away and close, respectively, and for the observer moving along the diagonal as well. For the source and observer being close ,$\varrho_2 = 1.54\lambda$, 30 terms are needed to ensure error smaller than 10^{-4}, and 3 terms are to be taken in a case $\varrho_1 = 0.78\lambda$ to achieve error rate 10^{-6}, while for the infinite periodic G_p accelerated only with Shanks' transform needs at least 180 partial sums to achieve error smaller than 10^{-2} in a singular case. Again, time needed for the Shanks' transform is 35 times bigger than for those needed with our method $55.83028s$ versus $1.552232s$. These results are graphically presented in Fig. 4.12–Fig. 4.15. In Fig. 4.16–Fig. 4.19 the GFs magnitude values of scalar and vector potentials, for different slab thicknesses and different values of the relative permittivity ε_{r}, obtained by our method, are presented. In Fig. 4.20 and Fig. 4.21 it is demonstrated, in a simple manner, the advantage of our method over the Shanks' transformation. The accuracies obtained for the different source-observer distances and a minimum number of terms needed to achieve desired accuracy are shown. Fig. 4.22 gives magnitude distribution of the scalar potential periodic GFs for "on

plane" case when the convergence of the series is extremely slow.

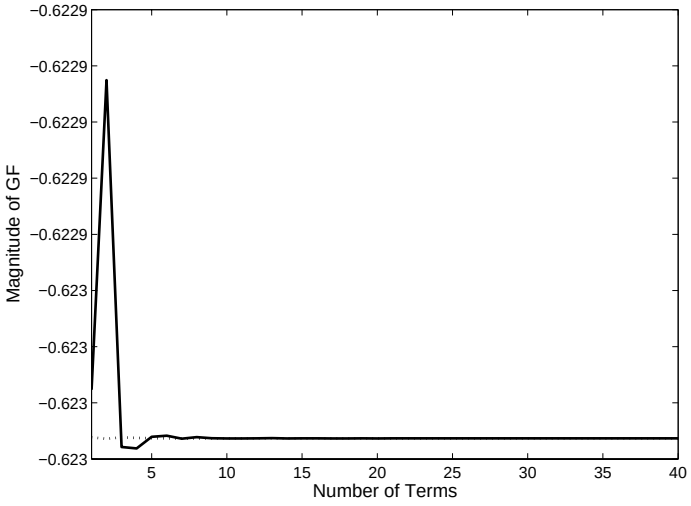

Figure 4.12: Magnitude of Green's function versus number of partial sums when Shanks method applied - solid line and our method - dotted line.

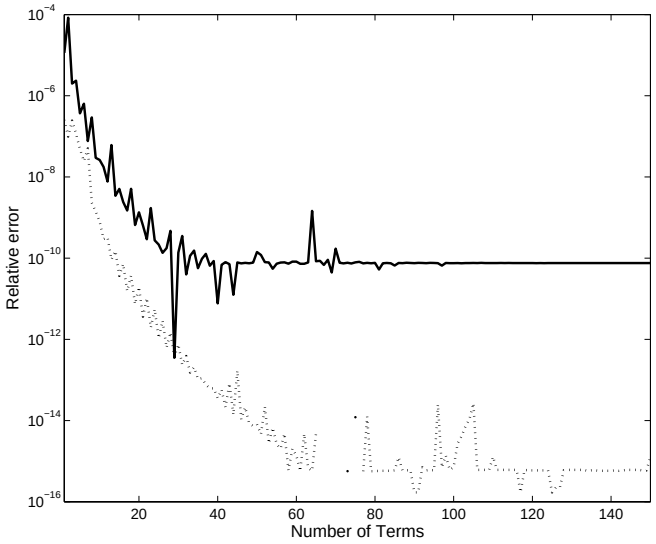

Figure 4.13: Relative error versus number of partial sums when Shanks method applied - solid line and our method - dotted line.

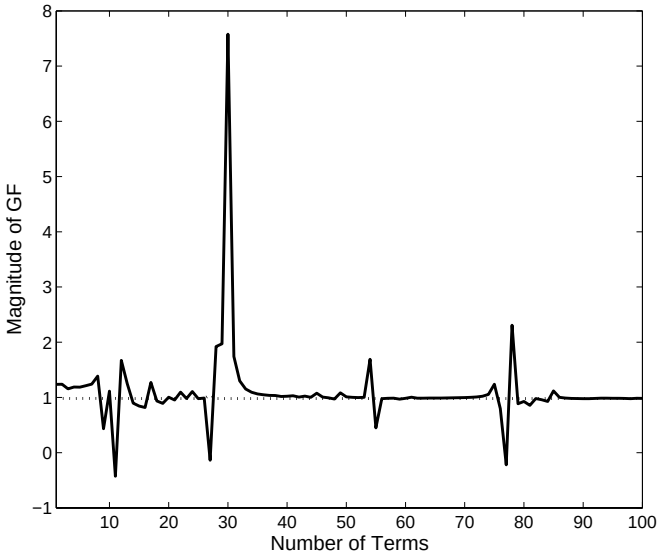

Figure 4.14: Magnitude of Green's function versus number of partial sums when Shanks method applied - solid line and our method - dotted line.

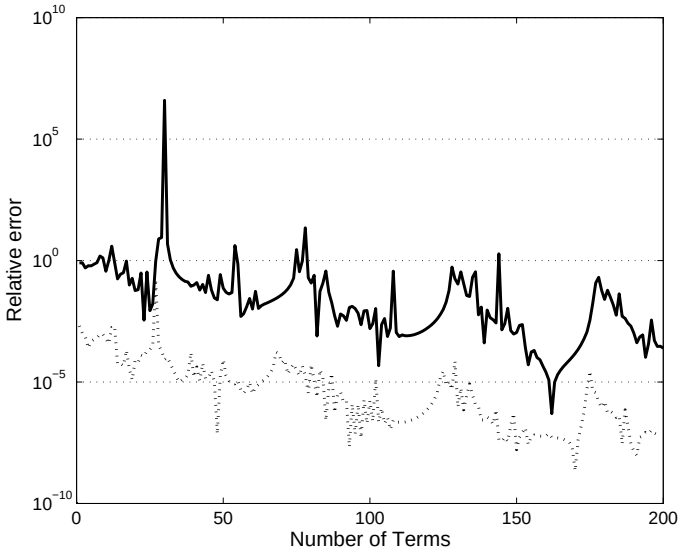

Figure 4.15: Relative error versus number of partial sums when Shanks method applied - solid line and our method - dotted line.

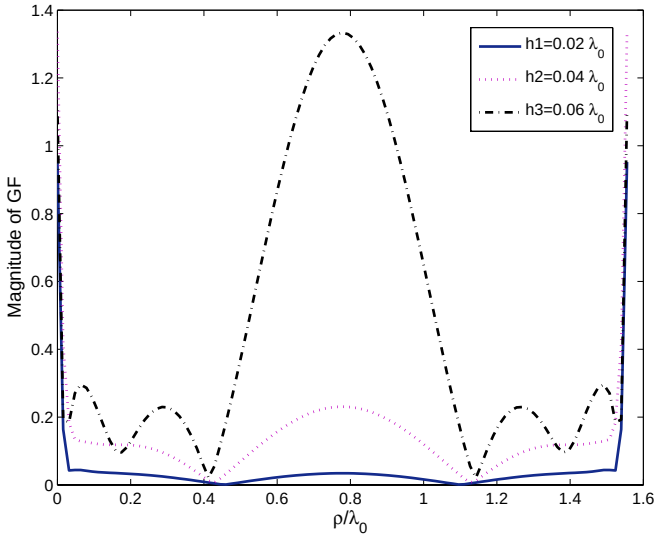

Figure 4.16: Magnitude of scalar potential periodic Green's function for different slab thickness; $\varepsilon_r = 9.8$.

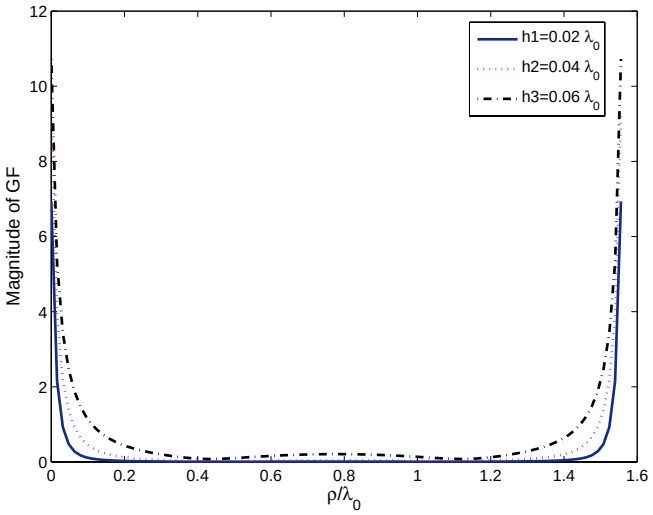

Figure 4.17: Magnitude of vector potential periodic Green's function for three different slab thickness; $\varepsilon_r = 9.8$.

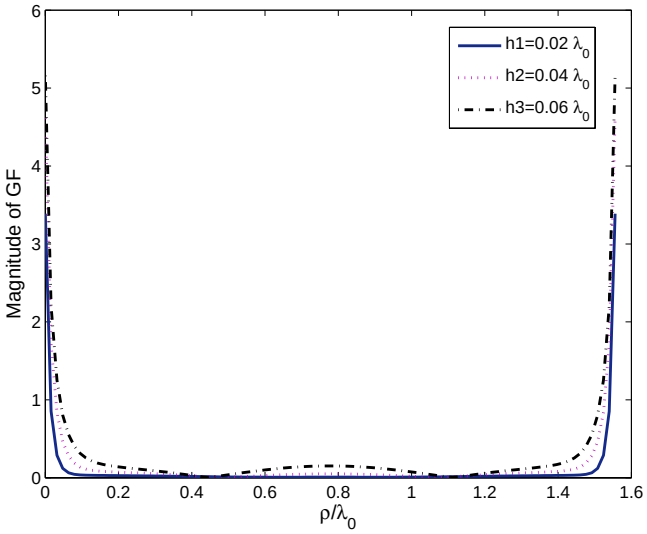

Figure 4.18: Magnitude of scalar potential periodic Green's function for different slab thickness; $\varepsilon_r = 2.55$.

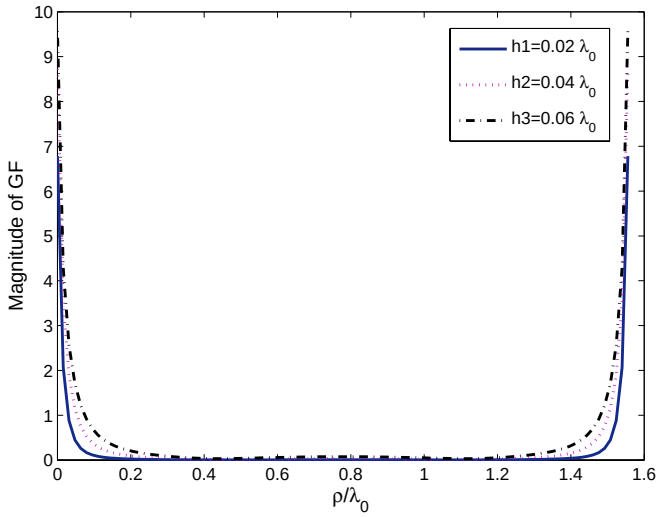

Figure 4.19: Magnitude of vector potential periodic Green's function for three different slab thickness; $\varepsilon_r = 2.55$.

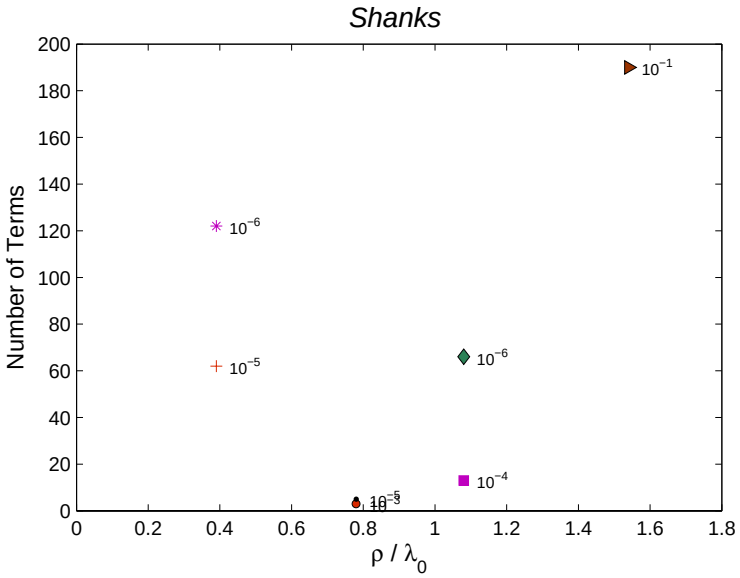

Figure 4.20: Number of terms needed in Shanks' transform for a given source observer distance to certain accuracy - e.g. blue triangle with 10^{-3} means that after 4 terms for a given normalized distance two successive terms differ in only first 3 digits.

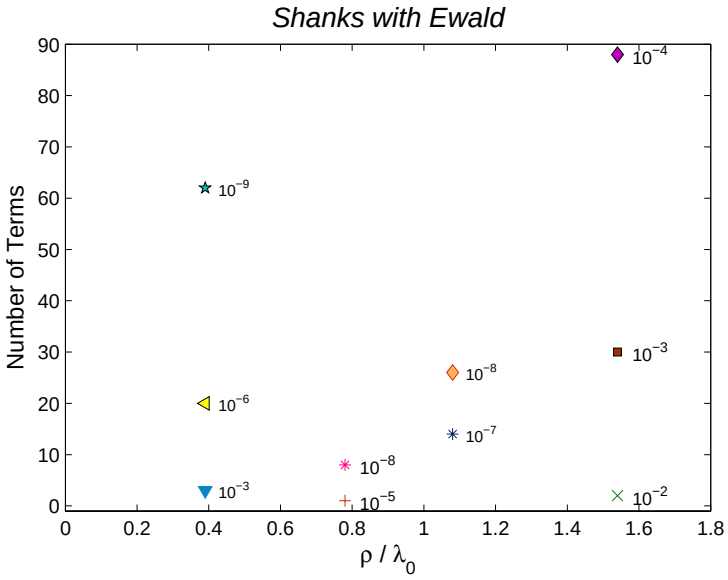

Figure 4.21: Number of terms needed in our approach for a given source observer distance to certain accuracy.

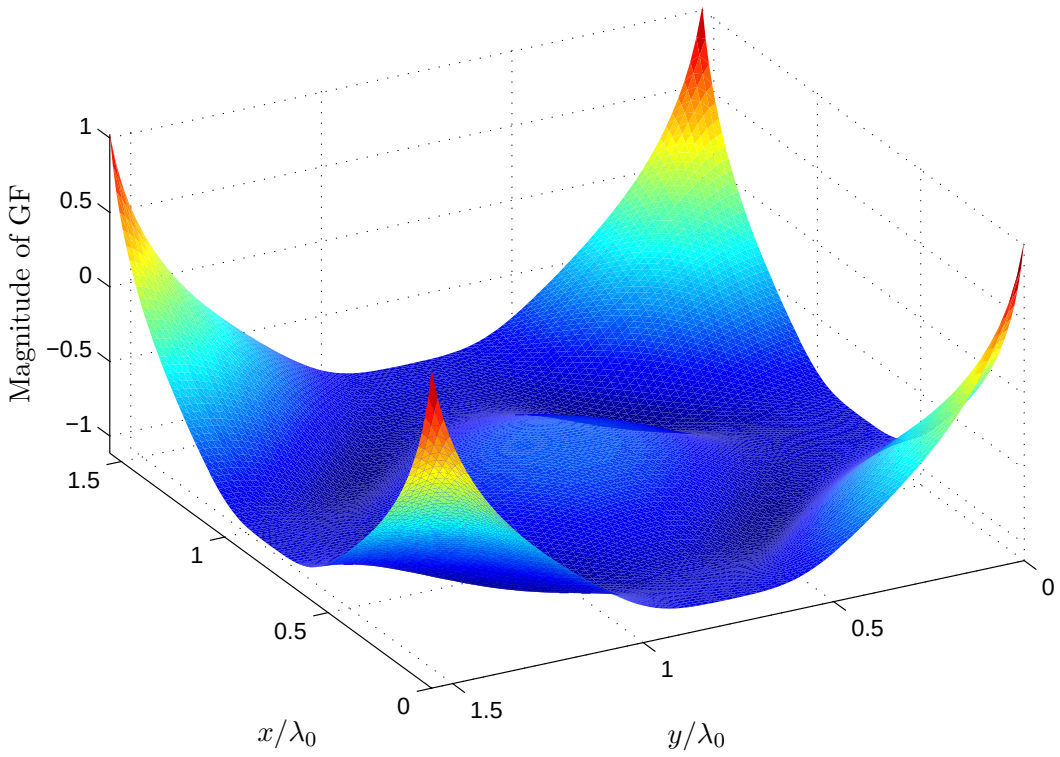

Figure 4.22: Magnitude distribution of scalar potential of the Green's function on the unit cell with periodicity $a = b = 1.1\lambda$, $f = 30\,\mathrm{GHz}$ and $\varepsilon_\mathrm{r} = 2.1$.

4.5 Conclusions

In this chapter we present a new approach for the fast and efficient calculation of multilayered GFs for the planar periodic structures. A new acceleration method combines successfully the two approaches that we have found to be the most convenient ones for our applications: Shanks' - good convergence in general but encounters difficulties in a source close region, and Ewald's transformation - provides very fast convergence in a case of free space GF. We have tried to benefit of the advantages that offer both techniques, first splitting the sum into two parts, dynamic and static part. Further, Shanks' has been successfully applied to the dynamic part of modal sums, whereas Ewald's transform has been applied to the remaining static part of the sum, transformed into an image series by means of Poisson's summation formula. An interesting convenience here was the possibility to implement Ewald's in the same way as it was done for the free-space GFs, skipping the use of more complicated techniques like Generalized Pencil Of Function (GPOF) that is required in case when Ewald's transform is used for acceleration of the multilayered periodic GFs. The approach elaborated in [61] can be used to calculate scalar potential GFs values. Our technique was applied in this work only to the vector potential GFs. It can be applied to the scalar potential GFs as well, but it requires first the static part to be transformed in a form suitable to the application of Ewald's transform to the free-space GFs.

5 Numerical Analysis of Scattering by Periodic Apertures in Conducting Screens of Finite Thickness

5.1 Introduction

The scattering of an EM plane wave by a periodically perforated ground plane is a classical problem in electromagnetic theory that finds numerous practical applications such as FSSs, PBG, self-standing ground planes, thick conducting films in microwave and mm-wave band, to mention only a few.

The EM scattering from a screen perforated by apertures has been studied more than centuries ago. Following papers reveal some interesting applications e.g. Bethe's theorem [62], metal-coated probe in a near-field optical microscope [63] and the extraordinary optical transmission through sub-wavelength hole arrays [64]. More "classic" EM applications are found in [65] where EM scattering from a rectangular aperture in a thin conducting plane has been studied with an operator equation. Finite-element method is used in [66, 67] to analyze scattering from a rectangular cavity and aperture in a thick conducting plane. A conducting screen perforated with multiple apertures is widely used as microwave FSSs. The scattering from infinite number of apertures in thick conducting screen is studied using MoM and the Floquet space harmonics that have been applied to solve the IE by Chen [32]. In [68, 69] the MoM has been used to compute the magnetic current on the finite number of apertures in an infinitely thin conducting plate. The Fourier transform and mode matching are used in [70] to study radiation from a rectangular waveguide with a lossy flange. The same numerical tools are used in [71] to provide a formulation for electromagnetic scattering from multiple rectangular apertures in a thick conducting screen. Electrostatic penetration into a rectangular aperture and a slit in a conducting plane were also studied by the Fourier transform and mode-matching method in [72, 73]. In this chapter we present a new approach to the numerical analysis of the periodically perforated ground plane with finite thickness (Fig. 5.1).

The problem of scattering can be divided, using the equivalence theorem and introducing magnetic currents, into two problems that are treated separately. The outer problem is treated applying the MPIE. Ewald's transform is used to accelerate the calculation of the MoM which is more time consuming in the case of periodic problem due to the slow convergence of the free space Green's function. Thus, the slowly convergent Green's function is converted into the sum of two rapidly converging series which are written in terms of the complementary error function. For more details see Chapter 3.

The inner problem (region inside the aperture) is treated with two different approaches. One way is to treat the aperture volume as a cavity (full-wave analysis), and solve it using

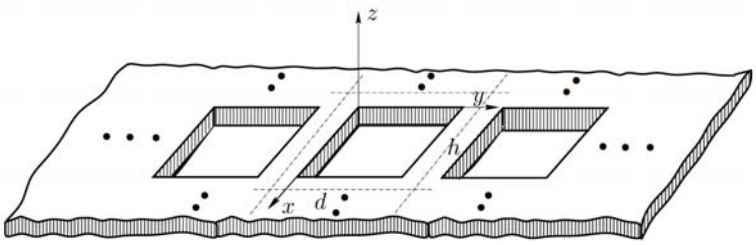

Figure 5.1: Periodically perforated thick conducting screen.

a modal expansion of the Green's functions. Although this model provides very accurate results, the number of unknowns is twice the number in the corresponding infinitely thin case. Moreover, this strategy becomes very hard to implement for arbitrary slot cross-sections.

Another way to solve the inner problem is to replace the cavity by a 2-D object that has the same geometry as the cross-section of the cavity and then apply the new approximate strategy reported in [6]. Then the aperture's thickness appears as a modification in the corresponding Green's function. This strategy has been already successfully applied for the efficient electromagnetic analysis of line-fed aperture antennas in thick conducting screens [74] and for thick irises in rectangular waveguides [35]. In this chapter we apply the approximate approach to efficiently solve the problem of scattering from thick periodic apertures. It combines successfully periodic GFs and approximate IE model and can be applied to apertures of arbitrary shape where modal GFs become difficult to compute for an arbitrary cross sections.

This chapter is organized as follows. In the first part we present a new approach for solving periodically perforated ground plane with finite thickness. Then, we explain two possible ways for calculating the correction term that takes into account screen's thickness. Finally, some numerical examples are given to validate the theory and compare either to full-wave approach or commercial software.

5.2 Scattering by Periodic Apertures in Conducting Screens with Finite Thickness

In the introduction of the chapter we briefly discuss how to solve the problem of scattering by periodically perforated conducting screen. The basic idea is, as already mentioned, to divide the problem into two problems as sketched in Fig. 5.2 that can be treated separately.

The outer problem is treated applying the MPIE. Ewald's transform is used as a powerful means to efficiently evaluate periodic GFs in the MoM matrix.

For solving the inner problem a better way is try to keep a numerical complexity (and a number of unknowns) identical to the zero thickness formulation and yet include in the model the effect of the screen's thickness. In the framework of integral equation formulations this can be achieved by making the thickness appear as a modification of the Green's functions [6]. The integral equation remains the same as in the zero-thickness case, save for the correction

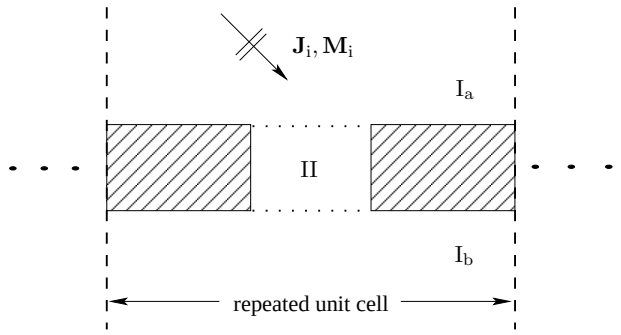

Figure 5.2: Unit cell of a periodically perforated ground screen where the outer problems (I_a and I_b) separated from the inner problem, (II) with the interfaces supporting equivalent magnetic currents.

term, which provides a smooth transition from the thick aperture case to the zero-thickness case. In the following subsections we will give more detailed explanation of tools used to solve the problem of scattering by periodic apertures in thick conducting screen.

5.2.1 The Outer Problems

The periodic GFs and Ewald's transform are elaborated in details in Chapter 3 provided with explanations of particular variables. For the sake of completeness the compact formulas of the periodic GFs and Ewald's transform are mentioned below. The two outer problems (half

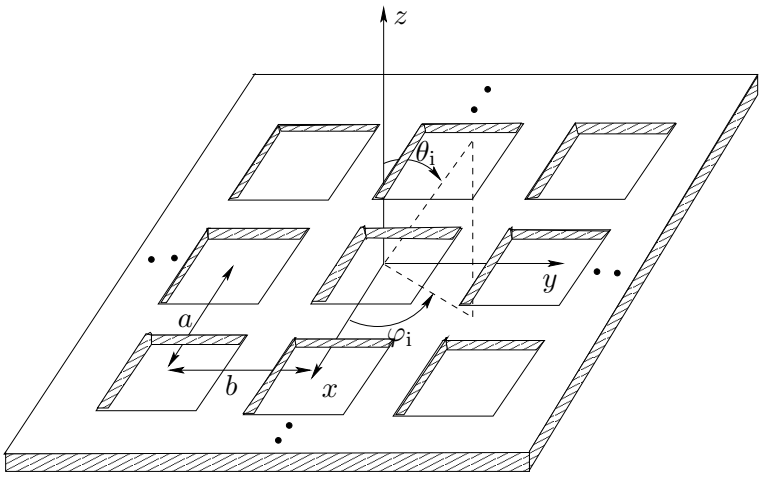

Figure 5.3: Thick conducting screen periodically perforated with square apertures and illuminated by plane wave.

spaces above and below the thick screen, see Fig. 5.2 are treated with the MPIE where the infinite periodic GFs, for the semi-infinite free space case are used as a kernel. The incident

field is a plane wave with a propagation direction given by the spherical coordinates $(\theta_\mathrm{i}, \varphi_\mathrm{i})$. The periodic Green's function in space domain is given by:

$$G_p(\mathbf{r}|\mathbf{r}') = 2 \sum_{m=-\infty}^{\infty} \sum_{n=-\infty}^{\infty} \mathrm{e}^{-\mathrm{j}\mathbf{k}_0 \cdot \boldsymbol{\rho}_{mn}} \times \frac{\mathrm{e}^{-\mathrm{j}k_0\sqrt{|\rho-\rho_\prime-\rho_{mn}|^2+(z-z')^2}}}{4\pi\sqrt{|\rho-\rho_\prime-\rho_{mn}|^2+(z-z')^2}} \ , \tag{5.1}$$

where $k_0 = 2\pi/\lambda$ is the free space wave number and $\boldsymbol{\rho}_{mn}$ is the translation vector for the spatial lattice

$$\boldsymbol{\rho}_{mn} = ma\hat{x} + nb\hat{y} \tag{5.2}$$

and

$$\boldsymbol{\rho} = x\hat{x} + y\hat{y} \tag{5.3}$$

$$\boldsymbol{\rho}' = x'\hat{x} + y'\hat{y} \tag{5.4}$$

where primed and unprimed coordinates designate source and observer position vectors respectively.

The periodic Green's function, given by (5.1) is efficiently evaluated using Ewald's transformation. The series in (5.1) is expressed as a sum of two different doubly infinite series [51]:

$$G_p = G_1 + G_2 \ , \tag{5.5}$$

where G_1 and G_2 are given by

$$\begin{aligned} G_1 &= 2\tfrac{1}{8ab} \sum_{m,n=-\infty}^{+\infty} \frac{\mathrm{e}^{\mathrm{j}\alpha_{mn}\cdot(\boldsymbol{\rho}-\boldsymbol{\rho}')}}{\alpha_{mn}} \sum_{\pm} \mathrm{e}^{\pm 2(z-z')\alpha_{mn}} \mathrm{erfc}(\tfrac{\alpha_{mn}}{E} \pm (z-z')E) \ , \\ G_2 &= 2\tfrac{1}{8\pi} \sum_{m,n=-\infty}^{+\infty} \frac{\mathrm{e}^{-\mathrm{j}\mathbf{k}_0\cdot\boldsymbol{\rho}_{mn}}}{R_{mn}} \mathrm{e}^{-\mathrm{j}\mathbf{k}_0\cdot\rho_{mn}} \sum_{\pm} \mathrm{e}^{\pm \mathrm{j}k_0 R_{mn}} \mathrm{erfc}(R_{mn}E \pm \tfrac{\mathrm{j}k_0}{2E}) \ . \end{aligned} \tag{5.6}$$

E is a constant which has to be chosen in a way such that both of the series G_1 and G_2 have approximately the same convergence rate. Due to the asymptotical behavior of the complementary error function, that appears in Ewald's transformation [44, 59], the series in G_1 and G_2 converge both rapidly.

5.2.2 The Inner Problem

Consider a structure as it is shown in Fig. 5.4. Effectively, it is a side cut of a unit cell of periodic structure Fig. 5.3. The structure can be treated (inside the aperture volume) as a cavity using a modal expansion of the Green's functions (see [6]) or using the approximate approach for the apertures in thick conducting planes proposed in [6] as follows.

The equivalence theorem is used to ensure the continuity of the tangential components of

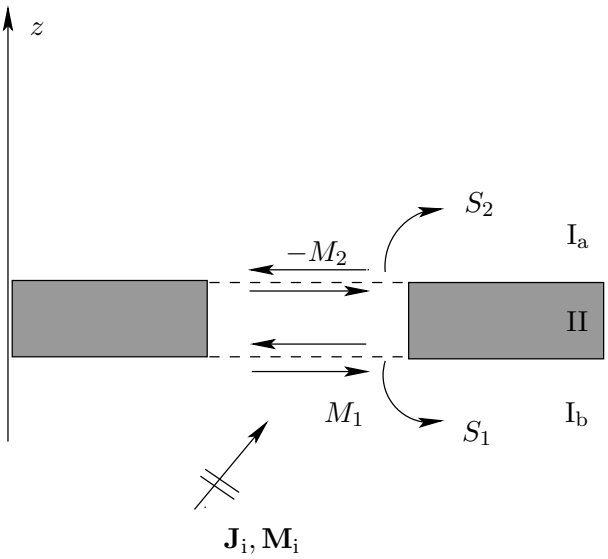

Figure 5.4: Aperture in conducting screen

the electric fields on aperture interfaces introducing the equivalent magnetic currents. The incident field $(\mathbf{E}^{\mathrm{i}}, \mathbf{H}^{\mathrm{i}})$ is assumed to be in the lower region of the aperture. The boundary conditions for magnetic field need also to be fulfilled and they are given by:

$$\hat{z} \times \left[\mathbf{H}^{+}(\mathbf{r}_1) - \mathbf{H}^{-}(\mathbf{r}_1)\right] = \hat{z} \times \mathbf{H}^{\mathrm{exc}} \quad \mathbf{r}_1 \in S_1 \tag{5.7}$$

$$\hat{z} \times \left[\mathbf{H}^{+}(\mathbf{r}_2) - \mathbf{H}^{-}(\mathrm{r}_2)\right] = 0 \quad \mathbf{r}_2 \in S_2 \tag{5.8}$$

Following the procedure outlined in [6], all the scattered fields are expressed as convolutions between the corresponding sources and Green's functions (linearity and superposition of IE):

$$\mathbf{H}_{\mathrm{s}}(\mathbf{r}) = \int_{S'} \overleftrightarrow{\mathbf{G}}(\mathbf{r}|\mathbf{r}')\mathbf{M}(\mathbf{r}')\,\mathrm{d}S' = \overleftrightarrow{\mathbf{G}} \otimes \mathbf{M}. \tag{5.9}$$

Moreover, in the closed aperture region, taking into account the symmetry and reciprocity [75], we only need two different Green's functions of the magnetic-magnetic (HM) type, namely, $\overleftrightarrow{\mathbf{G}}_{HM}^{(\mathrm{c})=}$ (the cavity Green's function with source and observer at the same horizontal interface) and $\overleftrightarrow{\mathbf{G}}_{HM}^{\mathrm{c}\times}$ (the cavity Green's function with source and observer at different horizontal interfaces). Then, according to [6], we define the sum and the difference cavity Green's functions as:

$$\overleftrightarrow{\mathbf{G}}^{\Sigma} = \overleftrightarrow{\mathbf{G}}^{=} + \overleftrightarrow{\mathbf{G}}^{\times} \tag{5.10}$$

$$\overleftrightarrow{\mathbf{G}}^{\Delta} = \overleftrightarrow{\mathbf{G}}^{=} - \overleftrightarrow{\mathbf{G}}^{\times} \tag{5.11}$$

where the first term in both equations corresponds to the cavity GFs being on the same

aperture interface and the second term to the cavity GFs being on the opposite aperture interfaces.

Following this logic and using the strategy suggested in [6] we introduce new pair of unknowns:

$$\mathbf{M}_\Sigma = \frac{\mathbf{M}_1 + \mathbf{M}_2}{2} \tag{5.12}$$

$$\mathbf{M}_\Delta = \frac{\mathbf{M}_1 - \mathbf{M}_2}{2} \tag{5.13}$$

that are a half sum and a half difference of the magnetic currents appearing on the aperture interfaces.
Introducing this new pair of unknowns into the boundary conditions (5.7) and (5.8) we obtain the following new set of integral equations:

$$\mathbf{H}^{\text{exc}} + (\overleftrightarrow{\mathbf{G}}^{(1)} + \overleftrightarrow{\mathbf{G}}^{(2)} + 2\overleftrightarrow{\mathbf{G}}^{\Delta}) \otimes \mathbf{M}_\Sigma + (\overleftrightarrow{\mathbf{G}}^{(1)} - \overleftrightarrow{\mathbf{G}}^{(2)}) \otimes \mathbf{M}_\Delta = 0 \tag{5.14}$$

$$(\overleftrightarrow{\mathbf{G}}^{(2)} + \overleftrightarrow{\mathbf{G}}^{\Delta}) \otimes \mathbf{M}_\Sigma = (\overleftrightarrow{\mathbf{G}}^{(2)} + \overleftrightarrow{\mathbf{G}}^{\Sigma}) \otimes \mathbf{M}_\Delta \tag{5.15}$$

And if we take as a first approximation

$$\mathbf{M}_\Delta \approx 0 \tag{5.16}$$

the system of equations (5.14) and (5.15) is transformed into

$$\mathbf{H}^{\text{exc}} + (\overleftrightarrow{\mathbf{G}}^{(1)} + \overleftrightarrow{\mathbf{G}}^{(2)} + 2\overleftrightarrow{\mathbf{G}}^{\Delta}) \otimes \mathbf{M}_\Sigma = 0 \tag{5.17}$$

that is effectively equation in the form of zero-thickness case save for the correction term $2\overleftrightarrow{\mathbf{G}}^{\Delta}$. In the section that follows the way how to calculate the correction term will be explained.

5.3 Correction Term Calculated Using Parallel-plate Approximation

The theory given here follows closely the part concerning the calculation of the cavity Green's functions explained in [74]. The cavity Green's functions can be expanded in terms of the eigenfunctions that depend on the shape of the cavity cross-section. However, if the lateral dimensions of the cavity are big enough compared to its length (large aperture), the guiding properties of the corresponding shallow cavity will be weak. And with the problem discretized into a number of subsectional basis functions, the appropriate currents in the center of the aperture will be only slightly affected by the cavity borders. Therefore, the problem can be treated as a parallel plate problem. The approximation will not be very accurate for the current coefficients belonging to the basis functions near the cavity borders. However, the form of the cavity is taken into account by the lateral distribution of the basis functions. Approximating the rigorous cavity formulation we avoid at the same time the summation of slowly convergent modal series [49, 76], and, maybe even more advantageous, the evaluation of the modal eigenfunctions for cavities with cross-sections of arbitrary shapes. It should be

noted however that this approximation will remain valid for all shapes of the aperture as long as the aperture thickness is sufficiently small compared to its minimal lateral dimension.

For a parallel plate problem, the equivalent transmission line network given in Fig. 5.5 is valid. The excitation with a voltage generator corresponds to a magnetic surface current on the interface and yields the two currents

$$I_1^{\mathrm{TM/TE}} = \frac{1}{2\pi} \frac{1}{\mathrm{j} Z_{\mathrm{c}}^{\mathrm{TM/TE}} \tan \beta t}, \tag{5.18a}$$

$$I_2^{\mathrm{TM/TE}} = \frac{1}{2\pi} \frac{1}{\mathrm{j} Z_{\mathrm{c}}^{\mathrm{TM/TE}} \sin \beta t}, \tag{5.18b}$$

where $Z_{\mathrm{c}}^{\mathrm{TM/TE}}$ is the characteristic impedance of the respective mode, namely $\beta/(\omega\varepsilon)$ for the TM mode and $\omega\mu/\beta$ for the TE mode, and t is the thickness of the considered aperture. The

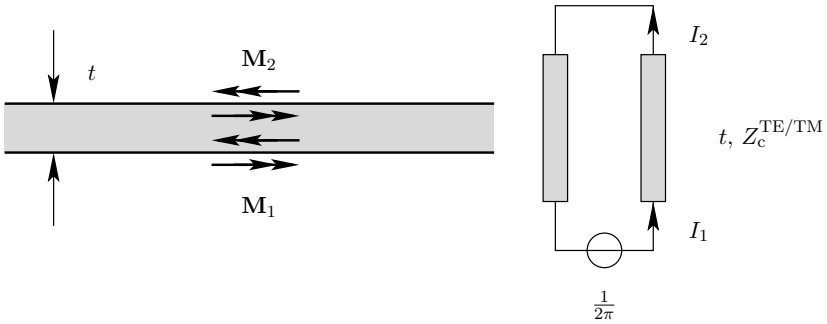

Figure 5.5: Equivalent TL network for a parallel plate problem [74].

correction terms of the potential Green's functions are then obtained applying the zero order inverse Sommerfeld transformation [27]

$$G_F^{(\mathrm{c})\Delta\, xx} = G_F^{(\mathrm{c})\Delta\, yy} = \mathcal{S}_0 \left[\frac{1}{\mathrm{j}\omega} (I_1^{\mathrm{TM}} - I_2^{\mathrm{TM}}) \right], \tag{5.19a}$$

$$G_W^{(\mathrm{c})\Delta} = \mathcal{S}_0 \left[\frac{\mathrm{j}\omega}{k_\rho^2} \left(I_1^{\mathrm{TE}} - I_2^{\mathrm{TE}} - (I_1^{\mathrm{TM}} - I_2^{\mathrm{TM}}) \right) \right]. \tag{5.19b}$$

It should be noted that both currents $I_{1,2}^{\mathrm{TM/TE}}$ go to infinity when the thickness of the aperture t approaches zero. However, their difference $I_1^{\mathrm{TM/TE}} - I_2^{\mathrm{TM/TE}}$, proportional to $\tan \frac{\beta t}{2}$, converges to zero when $t \to 0$, ensuring this way a smooth transition to the zero thickness case.

5.4 Correction Term Calculated using Ewald's Transform

One approach in efficient computing of the correction term is to neglect the lateral cavity walls and use a parallel plate Green's function when computing the correction term (see Section 5.3).

Another one, more accurate, is to use cavity potential Green's functions.

Any potential Green's function inside a rectangular cavity has in its expression the infinite sum of the basic image sets periodically translated along the x, y and z axes

$$\Psi = \frac{1}{4\pi} \sum_{m,n,p=-\infty}^{+\infty} \sum_{i=0}^{7} S_i \frac{\mathrm{e}^{-\mathrm{j}kR_{i,mnp}}}{R_{i,mnp}}, \tag{5.20}$$

where $S_i \in \{A_i^{ss}, F_i^{ss}, V_i, W_i\}$ represent the signs of the images in the basic image sets for the corresponding potential Green's function. In the same expression, $R_{i,mnp}$ is given by

$$R_{i,mnp} = \sqrt{(X_i + 2ma)^2 + (Y_i + 2nb)^2 + (Z_i + 2pc)^2}, \tag{5.21}$$

where X_i, Y_i and Z_i are the distances between the observer and images in basic image set and their values are defined for every image in a basic image set as following [37]:

$$X_i = \begin{cases} x - x', & i = 0,\ 1,\ 2,\ 3 \\ x + x', & i = 4,\ 5,\ 6,\ 7 \end{cases} \tag{5.22a}$$

$$Y_i = \begin{cases} y - y', & i = 0,\ 1,\ 4,\ 5 \\ y + y', & i = 2,\ 3,\ 6,\ 7 \end{cases} \tag{5.22b}$$

$$Z_i = \begin{cases} z - z', & i = 0,\ 2,\ 4,\ 6 \\ z + z', & i = 1,\ 3,\ 5,\ 7 \end{cases} \tag{5.22c}$$

$$R_{i,mnp} = \sqrt{(X_i + 2ma)^2 + (Y_i + 2nb)^2 + (Z_i + 2pc)^2} \tag{5.22d}$$

Variables X_i, Y_i and Z_i depend on the position of the image in the basic image set.

Using Ewald's transformation, the potential Green's functions in rectangular cavity can be summarized by the following equations

$$G = \kappa\Psi \tag{5.23a}$$

$$\Psi = \Psi_1 + \Psi_2, \tag{5.23b}$$

$$\Psi_1 = \frac{1}{abc} \sum_{m,n,p=0}^{+\infty} \varepsilon_m \varepsilon_n \varepsilon_p k_{mnp} f(k_{x_m} x, k_{x_m} x') g(k_{y_n} y, k_{y_n} y') h(k_{z_p} z, k_{z_p} z') \tag{5.23c}$$

where

$$k_{mnp} = \frac{\mathrm{e}^{-\frac{\alpha_{mnp}^2}{4E^2}}}{\alpha_{mnp}^2}, \tag{5.23d}$$

$$\alpha_{mnp} = \left(\frac{m\pi}{a}\right)^2 + \left(\frac{n\pi}{b}\right)^2 + \left(\frac{p\pi}{c}\right)^2 - k^2 \tag{5.23e}$$

$$\varepsilon_\nu = \begin{cases} 1, & \nu = 0 \\ 2, & \nu > 0 \end{cases} \tag{5.23f}$$

$$\Psi_2 = \sum_{m,n,p} \sum_{i=0}^{7} \frac{S_i}{8\pi R_{i,mnp}} \left(\mathrm{e}^{-\mathrm{j}kR_{i,mnp}} \operatorname{erfc}(R_{i,mnp}E - \mathrm{j}\frac{k}{2E}) + \mathrm{e}^{\mathrm{j}kR_{i,mnp}} \operatorname{erfc}(R_{i,mnp}E + \mathrm{j}\frac{k}{2E}) \right) \tag{5.23g}$$

The complementary error function which appears in both series Ψ_1 and Ψ_2 makes these series

G	κ	$f(x,x')$	$g(y,y')$	$h(z,z')$	S_i
G_A^{xx}	μ	$\cos x \cos x'$	$\sin y \sin y'$	$\sin z \sin z'$	A_i^{xx}
G_A^{yy}	μ	$\sin x \sin x'$	$\cos y \cos y'$	$\sin z \sin z'$	A_i^{yy}
G_A^{zz}	μ	$\sin x \sin x'$	$\sin y \sin y'$	$\cos z \cos z'$	A_i^{zz}
G_V	$\frac{1}{\varepsilon}$	$\sin x \sin x'$	$\sin y \sin y'$	$\sin z \sin z'$	V_i
G_F^{xx}	ε	$\sin x \sin x'$	$\cos y \cos y'$	$\cos z \cos z'$	F_i^{xx}
G_F^{yy}	ε	$\cos x \cos x'$	$\sin y \sin y'$	$\cos z \cos z'$	F_i^{yy}
G_F^{zz}	ε	$\cos x \cos x'$	$\cos y \cos y'$	$\sin z \sin z'$	F_i^{zz}
G_W	$\frac{1}{\mu}$	$\cos x \cos x'$	$\cos y \cos y'$	$\cos z \cos z'$	W_i

Table 5.1: The parameters for the potential Green's functions in rectangular cavity, computed using Ewald transformation.

converge rapidly. The best choice for the splitting parameter E is the one that balances the rate of decay of the two series, making Ψ_1 and Ψ_2 contribute an equal number of terms to the final value Ψ. The approximation of the optimal value of E for 2-D series (rectangular waveguide Green's functions or 2-D periodic Green's functions [51]), is given by

$$E = \sqrt{\frac{\pi}{ab}}.$$

In the case of 3-D sums, the optimal parameter is given by [77]

$$E = \left(\pi^2 \frac{\frac{1}{a^2} + \frac{1}{b^2} + \frac{1}{c^2}}{a^2 + b^2 + c^2} \right)^{1/4}.$$

The correction factor is defined as (5.11, 5.10)

$$\overleftrightarrow{\mathbf{G}}_F^{\Delta\, xx} = \overleftrightarrow{\mathbf{G}}_F^{=\, xx} - \overleftrightarrow{\mathbf{G}}_F^{\times\, xx}, \tag{5.24a}$$

$$\overleftrightarrow{\mathbf{G}}_F^{\Delta\, yy} = \overleftrightarrow{\mathbf{G}}_F^{=\, yy} - \overleftrightarrow{\mathbf{G}}_F^{\times\, yy}, \tag{5.24b}$$

$$G_W^{\Delta} = G_W^{=} - G_W^{\times}. \tag{5.24c}$$

so in general for any potential GFs we can write

$$\Psi^{\Delta} = \Psi^{=} - \Psi^{\times} \tag{5.25}$$

where

$$\Psi^{=} = \Psi(z = 0, z' = 0) \tag{5.26}$$

$$\Psi^{\times} = \Psi(z = c, z' = 0) \tag{5.27}$$

as it is shown in Fig. 5.6 We will use cavity GFs to derive the new correction factor. In the

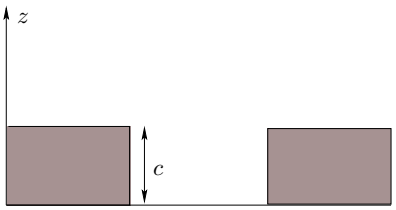

Figure 5.6: Lateral view of the cavity

case of cavity GFs we have to chose optimum value of the splitting parameter E for 3-D sums [77] that is given by:

$$E = \left(\pi^2 \frac{\frac{1}{a^2} + \frac{1}{b^2} + \frac{1}{c^2}}{a^2 + b^2 + c^2} \right)^{1/4}.$$

where a, b and c are the dimensions of the cavity. First, we will take c very small and at the same time $a, b \gg c$. As a consequence that gives large values for the splitting parameter E. This means that in the equation:

$$\Psi = \Psi_1 + \Psi_2, \tag{5.28}$$

large values of E will imply $\Psi_2 \longrightarrow 0$ and $\Psi_1 \approx 0$.

Let us look at the definition of Ψ_1

$$\Psi_1 = \frac{1}{abc} \sum_{m,n,p=0}^{+\infty} \varepsilon_m \varepsilon_n \varepsilon_p k_{mnp} f(k_{x_m} x, k_{x_m} x') g(k_{y_n} y, k_{y_n} y') h(k_{z_p} z, k_{z_p} z') \tag{5.29}$$

where

$$k_{mnp} = \frac{\mathrm{e}^{-\frac{\alpha_{mnp}^2}{4E^2}}}{\alpha_{mnp}^2}, \tag{5.30}$$

$$\alpha_{mnp} = \left(\frac{m\pi}{a}\right)^2 + \left(\frac{n\pi}{b}\right)^2 + \left(\frac{p\pi}{c}\right)^2 - k^2 \tag{5.31}$$

$$\varepsilon_\nu = \begin{cases} 1, & \nu = 0 \\ 2, & \nu > 0 \end{cases} \tag{5.32}$$

where three indices m, n, p can not be all at the same time equal 0.
For large values of E, k_{mnp} from (5.30) becomes

$$k_{mnp} \approx \frac{1}{\alpha_{mnp}^2} \tag{5.33}$$

Now for $\Psi^{=}$, $\Psi^{\times}$ and Ψ^{Δ} one can write

$$\Psi_1^{=} = \frac{1}{abc} \sum_{m,n,p} \frac{\varepsilon_m \varepsilon_n \varepsilon_p}{\alpha_{mnp}^2} fgh(0,0) \tag{5.34}$$

$$\Psi_1^{\times} = \frac{1}{abc} \sum_{m,n,p} \frac{\varepsilon_m \varepsilon_n \varepsilon_p}{\alpha_{mnp}^2} fgh(c,0) \tag{5.35}$$

and

$$\Psi^{\Delta} = \Psi_1^{=} - \Psi_1^{\times} = \frac{1}{abc} \sum_{m,n,p} \frac{\varepsilon_m \varepsilon_n \varepsilon_p}{\alpha_{mnp}^2} fg(h(0,0) - h(c,0)) \tag{5.36}$$

Since for all G_F^{xx}, G_F^{yy} and G_W (see Table 5.1)

$$h(z, z') = \cos(k_{zp} z) \cos(k_{zp} z') \tag{5.37}$$

we have

$$\begin{aligned} h(0,0) - h(c,0) &= 1 - \cos(k_{zp} c) \\ &= 1 - \cos(\frac{p\pi}{c} c) \\ &= 1 - (-1)^p \end{aligned} \tag{5.38}$$

Finally for Ψ^{Δ} we obtain following

$$\Psi^{\Delta} = \frac{1}{abc} \sum_{m,n,p} \frac{\varepsilon_m \varepsilon_n \varepsilon_p}{\alpha_{mnp}^2} fg[1 - (-1)^p]. \tag{5.39}$$

We also see the following

$$\frac{1}{c} \cdot \frac{1}{\alpha_{mnp}^2} = \frac{c}{c^2 \alpha_{mnp}^2} = \frac{c}{\left(\frac{m\pi}{a} c\right)^2 + \left(\frac{n\pi}{b} c\right)^2 + (p\pi)^2 - k^2 c^2} \tag{5.40}$$

When $c \to 0$ then denominator of (5.40) goes to $(p\pi)^2$ i.e. finite value what is important in terms of numerical simulations and nominator of (5.40) goes to 0, so we have

$$\lim_{c \to 0} \Psi^{\Delta} = 0 \tag{5.41}$$

In other terms the smooth transition to the zero thickness case is provided as well.

5.5 Results

In order to show till which extent the "delta" model of Green's function [6] can be applied to our case of thick periodic apertures, some numerical results are presented below.

5.5.1 Current distribution

The unit cell of the periodic structure is a $\lambda \times \lambda$ square of thickness $\lambda/10$. Cell periodicity is given by $a = b = 1.2\lambda$. The periodic structure is excited with a normally incident plane wave having its electric field along the y-coordinate. Logically the most interesting component in this case is the magnetic current along the x-axis. This component was considered in two planes, the longitudinal one $x = \lambda/2$ and the transversal one $y = \lambda/2$. The results are presented in Fig. 5.7–Fig. 5.9. The exact results are obtained applying the cavity method, giving the value of the currents on both sides of the aperture. The approximation yields the values of the current that are almost the exact arithmetic average of the currents obtained by the cavity model. The values obtained by the zero-thickness model match better the current values in the excitation side of the aperture but provide a poor representation of the phenomena arising in the aperture side opposite to the excitation. The approximation in [6] is less time consuming compared to the cavity model and invariant to the aperture shape, in which case the cavity model gets very complicated.

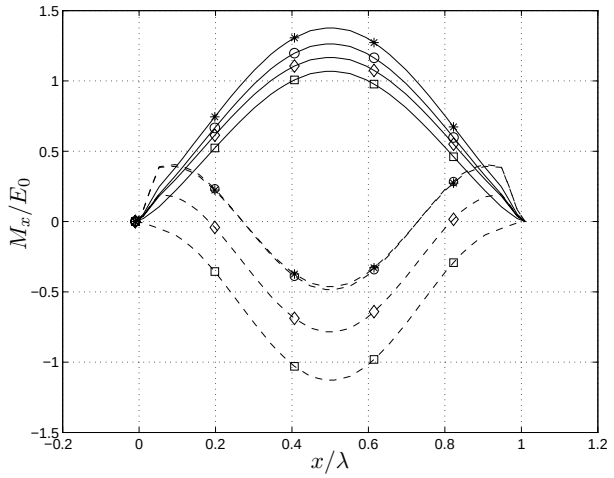

Figure 5.7: Normalized x–component of the magnetic current along the line $y = \lambda/2$ over a square $\lambda \times \lambda$ aperture of thickness $\lambda/10$. Normal incidence. Plane wave illumination. Periodicity of the structure $a = b = 1.2\lambda$. $\circ$ – M_1, $\square$ – M_2, $\diamond$ – M_Σ, $*$ – zero-thickness slot. Solid line – real part, dashed line – imaginary part.

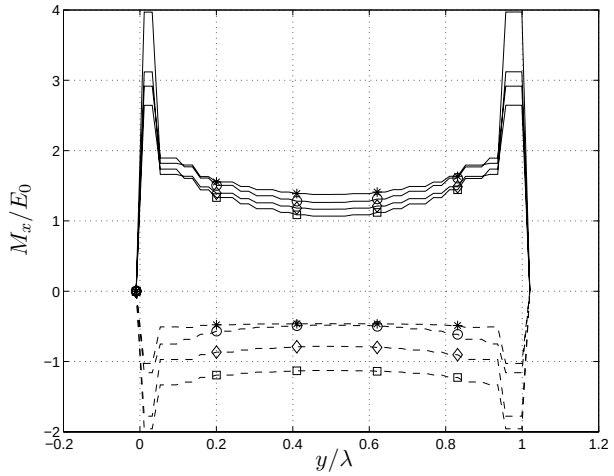

Figure 5.8: Normalized y–component of the magnetic current along the line $x = \lambda/2$ over a square $\lambda \times \lambda$ aperture of thickness $\lambda/10$. Normal incidence. Plane wave illumination. Periodicity of the structure $a = b = 1.2\lambda$. $\circ$ – M_1, $\square$ – M_2, $\diamond$ – M_Σ, $*$ – zero-thickness slot. Solid line – real part, dashed line – imaginary part.

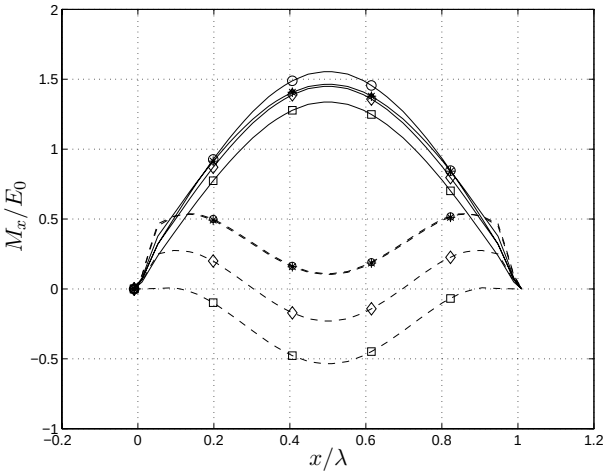

(a) Normalized x–component of the magnetic current along the line $y = \lambda/2$ over a square $\lambda \times \lambda$ aperture of thickness $\lambda/10$.

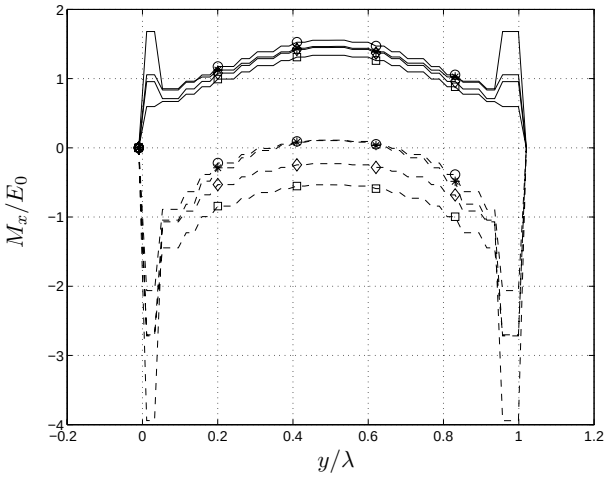

(b) Normalized y–component of the magnetic current along the line $x = \lambda/2$ over a square $\lambda \times \lambda$ aperture of thickness $\lambda/10$.

Figure 5.9: Normal incidence. Plane wave illumination. Periodicity of the structure $a = b = 1.6\lambda$. $\circ$ – M_1, $\square$ – M_2, $\diamond$ – M_Σ, $*$ – zero-thickness slot. Solid line – real part, dashed line – imaginary part.

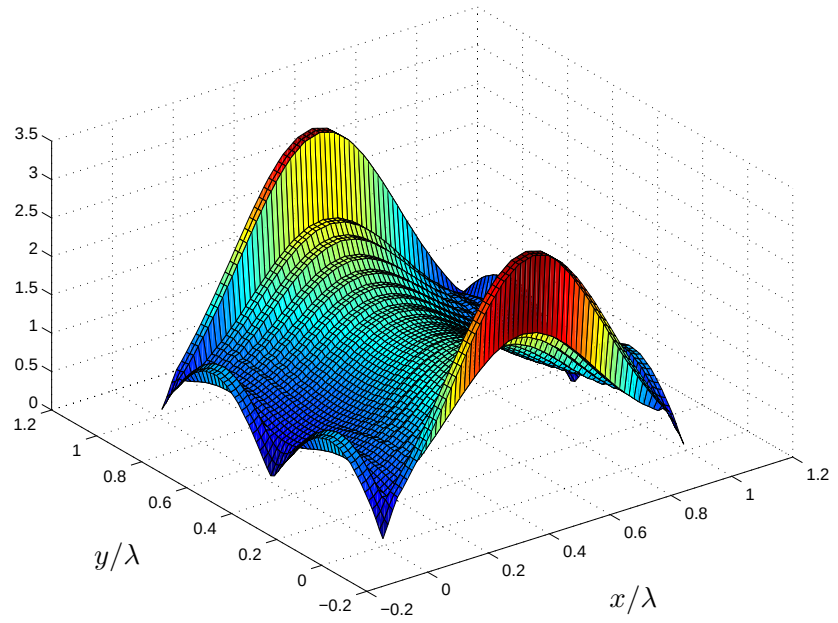

(a) Component M_1 of normalized magnitude of the x-component of magnetic current over a $\lambda \times \lambda$ aperture of thickness $\lambda/10$ - lower aperture interface (full cavity approach).

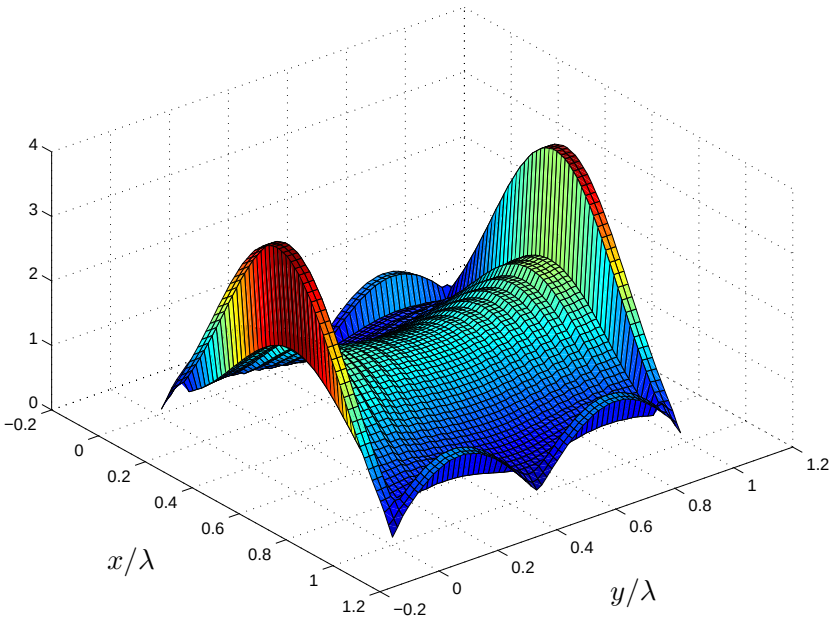

(b) Component M_Σ of normalized magnitude of the x-component of magnetic current over a $\lambda \times \lambda$ aperture of thickness $\lambda/10$ - average value using the approach in [6].

Figure 5.10

5.5.2 Time study

In Figure 5.11 the computational time versus the number of the unknowns is presented. A periodic structure with the periodicity 1.7λ formed by square apertures size $3\lambda/2 \times 3\lambda/2$ of thickness $\lambda/10$ was taken as an example. The structure is illuminated by a normal incidence plane wave from below having the magnetic field polarized in the x-direction. Both the full-wave cavity and the approximate approach (Section 5.3) have been tested. The delta approach remains simpler and faster although here the gain in computer time is not so impressive. This is due to the overhead introduced in periodic problems by the Green's function computation, even when Ewald's acceleration is used.

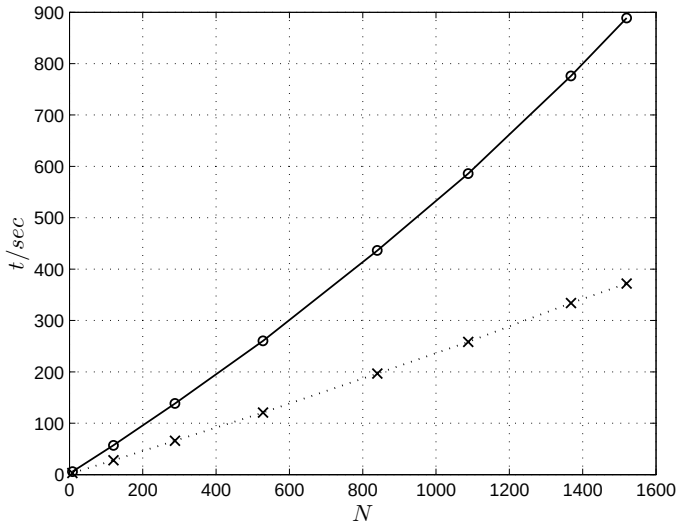

Figure 5.11: Computational time versus the number of unknowns for the full-wave method ($\circ$) and the delta approach ($\times$) for the periodic structure of the thickness $\lambda/10$.

5.5.3 Radiation pattern

The scattering by a finite periodic structure of apertures is simulated in order to examine the influence of the screen thickness on the 'far-field' parameters. The infinite periodic GFs is taken as a first approximation for the structure consisted of 3×3 apertures of length 10λ and width $\lambda/10$. The infinite sum in GFs is truncated after first three partial sums. The radiation pattern for the unit cell of a structure Fig. 5.12 is given in Fig. 5.13. In fact, the "infinite approach" gives better approximate solution for the cells that are in the same environment as if they would be in an infinite array i.e. unit cell than for those that are on the edge and having different environment. Although the difference between the three presented approaches is not remarkable it shows that the presented approach and full-wave method agree well (especially in the side-lobe levels).

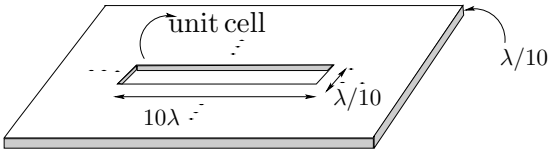

Figure 5.12: Aperture $10\lambda \times \lambda/10$ taken as unit cell of periodic structure of the thickness $\lambda/10$. Plane wave impinging from below the perforated screen with incidence angle $\theta_i = 45°$

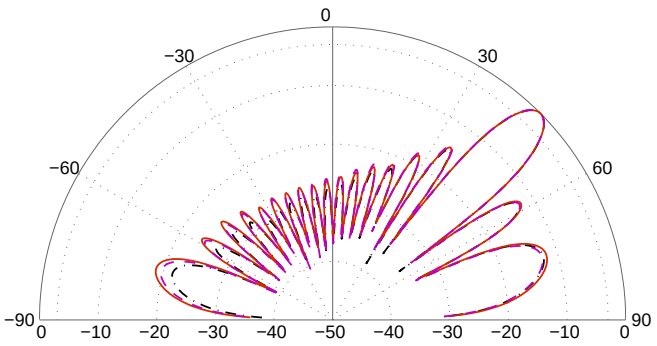

Figure 5.13: Radiation pattern of the unit cell of finite periodic structure consisted of 3×3 elements-slot $10\lambda \times \lambda/10$ taken as unit cell of periodic structure of the thickness $\lambda/10$. Plane wave impinging from below the perforated screen with incidence angle $\theta_i = 45$. Solid line – approach, dashed line – full wave method, dashed dot – zero thickness method.

5.5.4 Reflection/Transmission coefficients

Although good for evaluating the current distribution and radiation pattern the approach in Section 5.3 did not give results accurate enough for calculating the transmission and reflection coefficients for periodically perforated conducting screen. Thus, following the approach explained in 5.4 the reflection and transmission coefficients for the test-structure in Fig. 5.14 are evaluated. The simulations were carried out for the zero thickness screen and for the screen's thickness of $c = 0.1$mm and compared to the results obtained using the commercial software HFSS.

The dimensions of the unit cell - test-structure are given by $a = 22.86, b = 10.16, a_1 = 11.43, b_1 = 5.08$; all the dimensions are given in mm. For the central frequency $f = 15$GHz we have that the finite screen thickness is $c = 0.1\text{mm} = \lambda/200$ which is of practical interest (in [4] states that all the screen thicknesses greater than $\lambda/1000$ cannot be neglected). In Fig. 5.15 and Fig. 5.16 we show the results of simulations obtained with our approach and with HFSS. The good agreement can be observed between the two approaches.

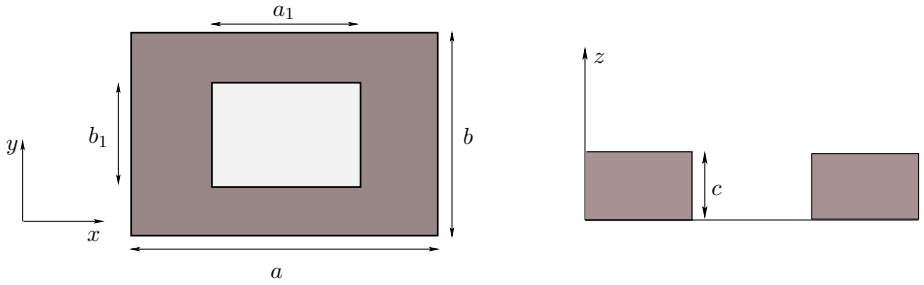

(a) Top view. (b) Side view.

Figure 5.14: Unit cell of the periodically perforated conducting screen.

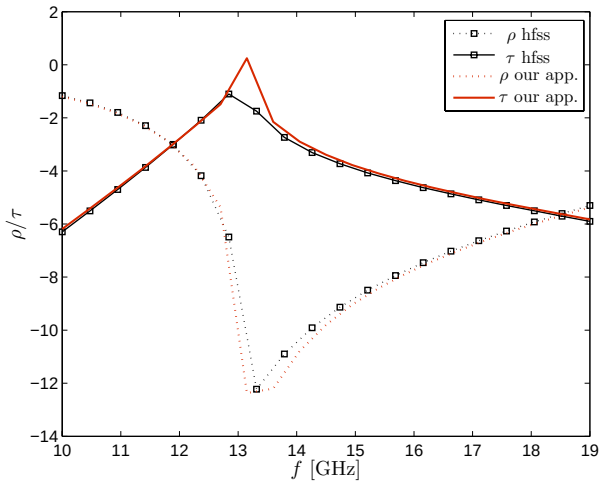

Figure 5.15: Reflection and transmission coefficients for the zero thickness screen.

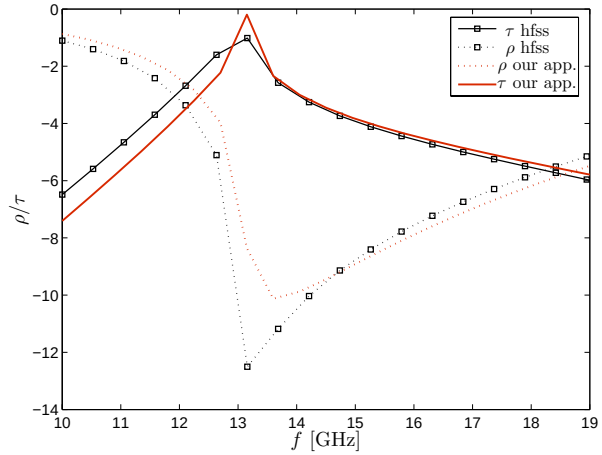

Figure 5.16: Reflection and transmission coefficients for the screen thickness $c = 0.1mm$.

5.6 Conclusions

This chapter presents an approximate and efficient IE approach that can be applied to EM analysis of conducting screens of finite thickness, periodically perforated by apertures of arbitrary shape. In this way the accurate and reliable results for important parameters in solving such structures, in particular calculation of the transmission and reflection coefficients, are provided. To emphasize, the complexity is in the range of zero-thickness approach and a good agreement with full-wave cavity approach is observed.

It is important to mention that the modeling of periodically perforated screens gives accurate results as far as the thickness of the aperture in the screen remains an order of magnitude smaller than its lateral dimensions.

In addition, we have performed a systematic study of computer time gain when the delta approach is used. It must be said that for the same accuracy the delta models halves the number of unknowns and this is an essential advantage only partially dimmed in the periodic case by the complexity of the associated GFs.

Moreover, a new original way of calculating the correction term in the approximate approach has been shown. It uses Ewald method applied to rectangular cavity potential GFs.

6 Conclusions and Perspectives

6.1 Thesis assessment

The present work has focused on numerical modeling of planar periodic structures in electromagnetics.

A commonly used numerical procedure for solving Maxwell's equations in planar micro- and millimeter wave structures consists of the application of Integral Equations in combination with the Method of Moments (IE/MoM). Although electromagnetic analysis based on Maxwell's equations is rigorous, to model periodic structures in microwave and millimetar wave range, it needs to be transformed into computer-convenient form. To do so, some approximations need to be adopted.

In science and engineering, numerical modeling of real-life structures, independently of the chosen technique (MoM, FEM, FDTD, ...) the problem i.e. structure needs to be discretized. In other terms structure surface/volume should be discretized into smaller pieces of surface or volume. In this work we have used the Method of Moments that is particularly well-suited for planar surface problems, and in combination with the Mixed Potential Integral Equation (MPIE), offers a possibility to treat planar periodic problems. The periodic Green's functions are incorporated in the IE/MoM solution for planar periodic structures and therefore we have used them in their image (spatial) and modal (spectral) formulation or both. Periodic structures (FSSs, PBG) are filters for microwaves, allowing the propagation for a certain frequency range and/or prohibiting the propagation for other frequencies. A complete study of periodic structures (FSSs, PBGs) includes always the reflection and transmission coefficients evaluation. They provide the most important information for periodic structures, their behavior in a certain frequency range is further used in design of such devices. All this theoretical issues have been elaborated in Chapter 2.

The periodic Green's functions are involved in the EM analysis of planar periodic structures and, depending on the application, are either free-space GFs or multilayered GFs. Free-space GFs are suitable for the analysis of self-supporting metallic patches, or conducting films in millimeter and submillimeter wave bands. Planar periodic structures are, in printed planar circuit technologies, often deposited on dielectrics and in that case the multilayered GFs are needed. Although the Green's functions in the EM community have been studied for a long time the reason why we still speak about them are the slow convergence problems that appear in case of infinite sums of GFs affiliated to the periodic problems. These issues have been discussed in Chapter 3. We have explored the efficiency of different accelerating techniques of general and specific types and applied them, first to 1-D sums that are of the

same nature as periodic GFs. Then, after having found Shanks' transform to be the most appropriate general technique, we proceeded to the acceleration of 2-D GFs involved in real planar structures' modeling. We have faced different problems arising in the acceleration of periodic GFs with Shanks' transform in terms of different ways of summing up the infinite series that we proposed, numerical instabilities and different problem formulations, such as modal and image formulation.

In the next chapter, we have proposed a new method for the acceleration of vector potential GFs for multilayered structures, combining successfully the two approaches that we have found to be the most convenient ones for our applications: Shanks' and Ewald's transform. We have tried to benefit of the advantages that offer both techniques, first splitting the sum into two parts, dynamic and static part. Further, Shanks' has been successfully applied to the dynamic part of modal sums, whereas Ewald's transform has been applied to the remaining static part of the sum, transformed into an image sum by means of Poisson's summation formula. An interesting convenience here was the possibility to implement Ewald's in the same way as it was done for the free-space GFs, skipping the use of more complicated techniques like Generalized Pencil Of Function (GPOF) that is required in case when Ewald's transform is used for accelerating the multilayered periodic GFs.

Numerous radiating structures, in particular those including periodic apertures, have been analyzed considering a classic problem of scattering by apertures in infinitely thin screen (zero-thickness screen). However, for higher operating frequencies and for self-supporting metallic structures, the thickness of metallic screens must be taken into account.

In Chapter 5 a new approach for the efficient analysis of periodically perforated ground planes with finite thickness has been proposed. The problem of scattering by a screen of finite thickness can be separated into two problems that are treated separately. One is a periodic problem and related to the outer problem that is efficiently evaluated by means of Ewald's transform. The another one is a cavity problem and linked with the inner problem. Moreover, we proposed two approximations that take into account the finite thickness of the aperture cavity. The proposed approximation allows the thick conducting screen to be modeled as zero-thickness screen, and the thickness appears only as a modification in the Green's function of the problem. The correction factor is computed using two approaches: the parallel plate GFs and Ewald's transform applied to rectangular cavity potential GFs. In the first technique the lateral aperture walls are neglected. The parallel plate GFs approach is advantageous in terms of CPU time, but its main advantage is its simplicity that is a consequence of the zero-thickness case. When higher accuracies are desired it is more suitable to compute the correction term using the second approach. The results have been compared to commercial software and a good agreement could be observed.

6.2 Perspectives

Although there are surely many ways left to be explored in "infinite periodic structures" in my humble opinion this work has opened some problems that might suggest interesting

phenomena to explore in the direction of finite periodic structures.

Not just that in real life all planar structures are of finite extent, but from the mathematical point of view the finite structures are more challenging. It is known that finite structures in many aspects behave like infinite periodic structures but this usually concerns the "inner part of the structure" while current distributions and scattering for those cells that do not "see" an infinite environment deviate significantly from those of an infinite structure.

Therefore, it would be interesting to find out the reflection and transmission coefficients of such structures and for example taking into account the finite thickness of conducting screen and furthermore to introduce losses in perfectly conducting screens.

Those who use the method of moments for modeling know that besides the subsectional basis functions certain structures can be modeled using the entire domain basis functions. Moreover, in our laboratory the technique of so called Macro Basis Functions (MBFs) that has proven to be efficient in modeling the large printed antenna arrays, has been developed. The basic idea of the method is to break a given geometry of the structure into smaller regions (subdomains) and perform numerical solutions for them. The set of isolated solutions on the individual subsectional basis functions belonging to a given subdomain is merged into so-called macro-basis functions (MBFs). Thus, it would be interesting to combine MBFs and the infinite structure approach. For example, divide the periodic structure into parts that can be solved via an "infinite approach" and those that cannot. Then, to the part that cannot be treated by an infinite approach apply MBFs. Another example are finite by infinite structures. This type of structures, that are in one dimension larger than in the other one might be solved by an hybrid approach that combines MBFs with infinite approach. The infinite approach for 1-D array could be applied along the large (infinite) dimension. Then the solution of each of 1-D arrays becomes new cell for MBFs approach. Then in the small direction we have finite number of cells on which the MBFs approach could be applied. The potential application of such structures might be in radar design.

Bibliography

[1] T. Itoh, ed., *Numerical Techniques for Microwave and Millimeter-Wave Passive Structures*. New York: Wiley, 1989.

[2] P. P. Silvester and R. L. Ferrari, *Finite Elements for Electrical Engineers*. Cambridge, UK: Cambridge Univ. Press, 2 ed., 1990.

[3] A. Taflove, *Computational Electrodynamics: The Finite-Difference Time-Domain Method*. Boston, MA: Artech House, 1995.

[4] B. A. Munk, *Frequency Selective Surfaces - Theory and Design*. New York, USA: Wiley, 2000.

[5] R. Mittra, C. H. Chan, and T. Cwik, "Techniques for analyzing frequency selective surfaces - a review," *Proc. IEEE*, vol. 76, pp. 1593–1615, Dec. 1988.

[6] J. R. Mosig, "Scattering by arbitrarily-shaped slots on thick metallic screens: An approximate solution," *IEEE Trans. Antennas Propagat.*, vol. 52, pp. 2109–2117, Aug 2004.

[7] J. B. Pendry, A. J. Holden, D. J. Robbins, and W. J. Stewart, "Magnetism from conductors and enhanced nonlinear phenomena," *IEEE Trans. Microwave Theory Tech.*, vol. 47, pp. 2075–2084, Nov. 1999.

[8] D. R. Smith, W. J. Padilla, D. C. Vier, S. C. Nemat-Nasser, and S. Schultz, "Composite medium with simultaneously negative permeability and permittivity," *Phys. Rev. Lett.*, vol. 84, pp. 4184–4187, May 2000.

[9] A. Boag, Y. Leviatan, and A. Boag, "Analysis of diffraction from doubly periodic arrays of perfectly conducting bodies by using a patch-current model," *J. Opt. Soc. Am. A*, vol. 7, pp. 1712–1718, Sept. 1990.

[10] N.-W. Chen, B. Shanker, and E. Michielssen, "Integral-equation-based analysis of transient scattering from periodic perfectly conducting structures," *IEE Proc.-Microw. Antennas Propag.*, vol. 150, pp. 120–124, Apr. 2003.

[11] I. Bardi, R. Remski, D. Perry, and Z. Cendes, "Plane wave scattering from frequency-selective surfaces by the finite-element method," *IEEE Trans. Magn.*, vol. 47, pp. 843–850, May 1999.

[12] S. D. Gedney, J. F. Lee, and R. Mittra, "A combined FEM/MoM approach to analyze the plane wave diffraction by arbitrary gratings," *IEEE Trans. Microwave Theory Tech.*, vol. 40, pp. 363–370, Feb. 1992.

[13] T. F. Eibert, J. L. Volakis, D. R. Wilton, and D. R. Jackson, "Hybrid FE/BI modeling of 3-D doubly periodic structures utilizing triangular prismatic elements and an MPIE formulation accelerated by the Ewald transformation," *IEEE Trans. Antennas Propagat.*, vol. 47, pp. 843–850, May 1999.

[14] I. Stevanović, P. Crespo-Valero, K. Blagović, F. Bongard, and J. R. Mosig, "Integral-equation analysis of 3-d metallic objects arranged in 2-d lattices using the ewald transformation," *IEEE Trans. Microwave Theory Tech.*, to be published in October 2006.

[15] R. Pous and D. M. Pozar, "A frequency-selective surface using aperture-coupled microstrip patches," *IEEE Trans. Antennas Propagat.*, vol. 39, pp. 1763–1769, Dec. 1991.

[16] C. Wan and J. A. Encinar, "Efficient computation of generalized scattering matrix for analyzing multilayered periodic structures," *IEEE Trans. Antennas Propagat.*, vol. 43, pp. 1233–1242, Nov. 1995.

[17] M. Bozzi, L. Perregrini, J. Weinzierl, and C. Winnewisser, "Efficient analysis of quasi-optical filters by a hybrid MoM/BI-RME method," *IEEE Trans. Antennas Propagat.*, vol. 49, pp. 1054–1064, July 2001.

[18] J. Callaway, *Quantum Theory of Solid State*. New York: Academic, 1991.

[19] P. P. Ewald, "Die Berechnung Optischer und Elektrostatischer Gitterpotentiale," *Ann. Phys.*, vol. 64, pp. 253–287, 1921.

[20] M. G. Silveirinha and C. A. Fernandes, "A new acceleration technique with exponential convergence rate to evaluate periodic Green's functions," *IEEE Trans. Antennas Propagat.*, vol. 53, pp. 347–355, Jan. 2005.

[21] R. F. Harrington, *Field Computation by Moment Methods*. New York: IEEE Press, second ed., 1993.

[22] http://gid.cimne.upc.es/.

[23] D. R. Wilton, S. M. Rao, A. W. Glisson, D. H. Schaubert, O. M. Al-Bundak, and C. M. Butler, "Potential integrals for uniform and linear source distributions on polygonal and polyhedral domains," *IEEE Trans. Antennas Propagat.*, vol. AP-32, pp. 276–281, Mar. 1984.

[24] N. Morita, N. Kumagai, and J. Mautz, *Integral Equation Methods for Electromagnetics*. Boston, USA: Artech House, 1990.

[25] A. A. Melcon, *Applications of the Integral Equation Technique to the Analysis and Synthesis of Multilayered Printed Shielded Microwave Circuits and Cavity Backed Antennas*.

PhD thesis, Ecole Polytechnique Fédérale de Lausanne, Switzerland, 1998. Thèse No. 1901.

[26] J. R. Mosig, "Arbitrarily shaped microstrip structures and their analysis with a mixed potential integral equation," *IEEE Trans. Microwave Theory Tech.*, vol. 36, pp. 314–323, Feb. 1988.

[27] J. R. Mosig, "Integral equation technique," in *Numerical Techniques for Microwave and Millimeter-Wave Passive Structures* (T. Itoh, ed.), ch. 3, pp. 133–213, New York: Wiley, 1989.

[28] S. M. Rao, D. R. Wilton, and A. W. Glisson, "Electromagnetic scattering by surfaces of arbitrary shape," *IEEE Trans. Antennas Propagat.*, vol. 30, pp. 409–418, May 1982.

[29] C.-C. Chen, "Transmission through a conducting screen perforated periodically with apertures," *IEEE Trans. Microwave Theory Tech.*, vol. MTT-18, pp. 627–632, Sept. 1970.

[30] C.-C. Chen, "Diffraction of electromagnetic waves by a conducting screen perforated periodically with circular holes," *IEEE Trans. Microwave Theory Tech.*, vol. MTT-19, pp. 475–481, May 1971.

[31] C.-C. Chen, "Scattering by a two-dimensional periodic array of conducting plates," *IEEE Trans. Antennas Propagat.*, vol. AP-18, no. 5, pp. 660–665, 1970.

[32] C.-C. Chen, "Transmission of microwave through perforated flat plates of finite thickness," *IEEE Trans. Microwave Theory Tech.*, vol. MTT-21, pp. 1–6, Jan. 1973.

[33] L. B. Felsen and N. Marcuvitz, *Radiation and Scattering of Waves.* Englewood Cliffs, NJ: Prentice-Hall, 1973.

[34] K. Kurokawa, "Power waves and the scattering matrix," *IEEE Trans. Microwave Theory Tech.*, vol. 10, pp. 314–320, Sept. 1965.

[35] I. Stevanović, P. Crespo-Valero, and J. R. Mosig, "An integral equation technique for solving thick irises in rectangular waveguides," *IEEE Trans. Microwave Theory Tech.*, vol. 54, pp. 189–197, Jan. 2006.

[36] A. Papoulis, *Systems and Transforms with Applications in Optics.* Malabar, FL: Kreiger, 1981.

[37] I. Stevanović, *Modeling Challenges in Computational Electromagnetics: Large Planar Multilayered Structures and Finite-Thickness Irises.* PhD thesis, Ecole Polytechnique Fédérale de Lausanne, Switzerland, 2005. Thèse No. 3212.

[38] K. A. Michalski and D. Zheng, "Electromagnetic scattering and radiation by surfaces of arbitrary shape in layered media, part I: Theory," *IEEE Trans. Antennas Propagat.*, vol. 38, pp. 335–344, Mar. 1990.

[39] K. A. Michalski and D. Zheng, "Electromagnetic scattering and radiation by surfaces of arbitrary shape in layered media, part II: Implementation and results for contigous half-spaces," *IEEE Trans. Antennas Propagat.*, vol. 38, pp. 345–352, Mar. 1990.

[40] N. Kinayman and M. I. Aksun, "Comparative study of acceleration techniques for integrals and series in electromagnetic problems," *Radio Sci.*, vol. 30, pp. 1713–1722, Nov.-Dec. 1995.

[41] Y. Brand, "Final Report For The Infinite Array Spatial Summation Green's Function." Final Report, 1995. Boulder, Colorado.

[42] C. Brezinski and M. R. Zaglia, *Extrapolation methods-theory and practice.* Elsevier Science Publishers, Amsterdam, 1991.

[43] S. Singh and R. Singh, "Efficient computation of the free-space periodic green's function," *IEEE Trans. Microwave Theory Tech.*, vol. 39, pp. 1226–1229, July 1991.

[44] N. Kinayman and M.I.Aksun, "Comparative study of acceleration techniques for integrals and series in electromagnetic problems," *Radio Science*, vol. 32, pp. 1713–1722, November-December 1984.

[45] S. Singh and R. Singh, "On the use of ρ-algorithm in series acceleration," *IEEE Trans. Antennas Propagat.*, vol. 39, pp. 1514–1517, October 1991.

[46] S. Singh and R. Singh, "A convergence acceleration procedure for computing slowly converging series," *IEEE Trans. Microwave Theory Tech.*, vol. 40, pp. 168–171, January 1992.

[47] S. Singh and R. Singh, "On the use of levin's t-transform in accelerating the summation of series representing the free-space periodic green's functions," *IEEE Trans. Microwave Theory Tech.*, vol. 41, pp. 884–886, May 1993.

[48] S. Singh and R. Singh, "On the use of chebyshev-toeplitz algorithm in accelerating the numerical convergence of infinite series," *IEEE Trans. Microwave Theory Tech.*, vol. 40, pp. 171–173, January 1992.

[49] J. Mosig and A. Alvarez-Melcon, "The summation-by-parts algorithm - a new efficient technique for the rapid calculation of certain series arising in shielded planar structures," *IEEE Trans. Microwave Theory Tech.*, vol. 50, pp. 215–218, January 2002.

[50] S. Singh, W. F. Richards, J. R. Zinecker, and D. R. Wilton, "Accelerating the convergence of series representing the free space periodic green's function," *IEEE Trans. Antennas Propagat.*, vol. 38, pp. 1958–1962, December 1990.

[51] K. E. Jordan, G. R. Richter, and P. Sheng, "An efficient numerical evaluation of the Green's function for the Helmholtz operator on periodic structures," *J. Comput. Phys.*, vol. 63, pp. 222–235, 1986.

[52] A. W. Mathis and A. F. Peterson, "Efficient electromagnetic analysis of a doubly infinite array of rectangular apertures," *IEEE Trans. Microwave Theory Tech.*, vol. 46, pp. 46–54, Jan. 1998.

[53] F. Capolino, D. R. Wilton, and W. A. Johnson, "Efficient computation of the 2-D Green's function for 1-D periodic structures using the Ewald method," *IEEE Trans. Antennas Propagat.*, vol. 53, pp. 2977–2984, Sept. 2005.

[54] M.-J. Park and S. Nam, "Efficient calculation of the Green's function for multilayered planar periodic structures," *IEEE Trans. Antennas Propagat.*, vol. 46, pp. 1582–1583, Oct. 1998.

[55] Y. Hua and T. K. Sarkar, "Generalized Pencil-of-Function method for extracting poles of an EM system from its transient response," *IEEE Trans. Antennas Propagat.*, vol. 37, pp. 229–234, Feb. 1989.

[56] N. Marcuvitz, *Waveguide Handbook*. McGraw-Hill, 1951.

[57] I. Stevanović, P. Crespo-Valero, and J. R. Mosig, "2-D Periodic Structure Modeling." Internal Report, 2005. LEMA, EPFL.

[58] D. Pozar and D. Schaubert, "Scan blindness in infinite phased arrays of printed dipoles," *IEEE Trans. Antennas Propagat.*, vol. 32, pp. 602–610, June 1984.

[59] K. Jordan, G. Richter, and P. Sheng, "An eficient numerical evaluation of the Green's function for the Helmholtz operator on periodic structures," *Journal of Computational Physics*, vol. 63, pp. 222–235, 1986.

[60] R. M. Shubair and Y. L. Chow, "Efficient computation of the periodic green's function in layered dielectric media," *IEEE Trans. Microwave Theory Tech.*, vol. 41, pp. 498–502, March 1993.

[61] D. Wang, E. K. N. Yung, R. Chen, D. Ding, and W. Tang, "On evaluation of the green function for periodic structures in layered media," *IEEE Antennas Wireless Propagat. Lett.*, vol. 3, pp. 133–136, 2004.

[62] H. A. Bethe, "Theory of diffraction by small holes," *Phys. Rev. Lett.*, vol. 66, pp. 163–182, Oct 1994.

[63] M. Ohtsu and H. Hori, *Near-field nano-optics: from basic principles to nano-fabrication and nano-photonics*. Kluwer Academic/Plenum Publishers, 1999.

[64] T. Ebbesen, H. Lezec, H. Ghaemi, T. Thio, and P. Wolff, "Extraordinary optical transmission through sub-wavelength hole arrays," *Nature*, no. 391, pp. 667–669, 1998.

[65] A. El-Hajj and K. Kabalan, "Characteristic modes of a rectangular aperture in a perfectly conducting plane," *IEEE Trans. Antennas Propagat.*, vol. 42, pp. 1447–1450, Oct 1994.

[66] K. Barkeshli and J. Volakis, "Electromagnetic scattering from an aperture formed by a rectangular cavity recessed in a ground plane," *J. Elect. Waves Appl.*, vol. 5, no. 7, pp. 715–735, 1991.

[67] J. Jin and J. Volakis, "Electromagnetic scattering by the transmission through a three-dimensional slot in a thick conducting plane," *IEEE Trans. Antennas Propagat.*, vol. 39, pp. 1544–1550, Apr 1991.

[68] T. Sarkar, M. Costa, C. I, and R. Harrington, "Electromagnetic transmission through mesh covered apertures and arrays of apertures in a conducting screen," *IEEE Trans. Antennas Propagat.*, vol. AP-32, pp. 908–913, 1984.

[69] T. Andersson, "Moment-method calculations on apertures using basis singular functions," *IEEE Trans. Antennas Propagat.*, vol. 41, pp. 1709–1716, 1993.

[70] K. Yoshitomi and H. Sharobim, "Radiation from a rectangular waveguide with a lossy flange," *IEEE Trans. Antennas Propagat.*, vol. 42, pp. 1398–1404, Oct. 1994.

[71] H. Park and H. Eom, "Electromagnetic scattering from multiple rectangular apertures in a thick conducting screen," *IEEE Trans. Antennas Propagat.*, vol. 47, no. 6, pp. 1056–1060, 1999.

[72] H. Park and H. Eom, "Electrostatic potential distribution through a rectangular aperture in a thick conducting plane," *IEEE Trans. Microwave Theory Tech.*, vol. 44, pp. 1745–1747, Oct. 1996.

[73] Y. Kim and H. Eom, "Fourier-transform analysis of electrostatic potential distribution through a thick slit," *IEEE Trans. Electromagn. Compat.*, vol. 38, pp. 77–79, Feb. 1996.

[74] I. Stevanović and J. R. Mosig, "Efficient electromagnetic analysis of line-fed aperture antennas in thick conducting screens," *IEEE Trans. Antennas Propagat.*, vol. 52, pp. 2896–2903, Nov 2004.

[75] R. Collin, *Field Theory of Guided Waves*. McGraw-Hill, New York, USA, 2nd ed., 1991.

[76] A. Alvarez-Melcon and J. Mosig, "Two techniques for the efficient numerical calculation of the green's function for planar shielded circuits and antennas," *IEEE Trans. Microwave Theory Tech.*, vol. 48, pp. 1492–1504, January 2000.

[77] A. Kustepeli and A. Q. Martin, "On the splitting parameter in the ewald method," *IEEE Microwave Guided Wave Lett.*, vol. 10, pp. 168–170, May 2000.

CV

Katarina Blagović was born in Sarajevo, Bosnia and Herzegovina, in 1976. She received the Dipl.Ing. degree in electrical engineering from the University of Zagreb, Zagreb, Croatia, in 2001, and is currently pursuing the Ph.D. degree at the Ecole Polytechnique Fédérale de Lausanne (EPFL), Lausanne, Switzerland.

In February 2002, she joined the Laboratory of Electromagnetics and Acoustics (LEMA), EPFL, where she is engaged as a Research and Teaching Assistant. She is involved in projects funded by the Swiss National Science Foundation (SNF). Her research interests include computational electromagnetics and frequency selective surfaces.

Ms. Blagović was the recipient of a scholarship presented by the Croatian Ministry of Science, Education and Sports (1996-2000) and a scholarship presented by the University of Zagreb (2000-2001).

List of Publications

REFEREED JOURNAL PAPERS

1. I. Stevanović, P. Crespo-Valero, K. Blagović, F. Bongard, and J. R. Mosig, "Integral Equation Analysis of 3-D Metallic Objects Arranged in 2-D Lattices Using the Ewald Transformation," *IEEE Transactions on Microwave Theory and Techniques*, accepted for publications (2006).

REFEREED CONFERENCE PAPERS

1. K. Blagović, I. Stevanović, J. R. Mosig, and A. K. Skrivervik, "New approach for the efficient analysis of the periodically perforated ground plane with finite thickness," *International Conference on Electomagnetics in Advanced Applications, ICEAA05*, Torino, Italy, September 12–16, 2005, pp. 431-434.

2. K. Blagović, I. Stevanović, J. R. Mosig, and A. K. Skrivervik, "Numerical analysis of scattering by periodic apertures in conducting screens with finite thickness," *IEEE AP-S International Symposium and USNC/URSI National Radio Science Meeting*, Washington DC, July 3–8, 2005, pp. 338-341.

3. K. Blagović, I. Stevanović, and A. K. Skrivervik, "Convergence of the infinite periodic Green's function with the application to canonical FSS structure case," *Journes Internationales de Nice sur les antennes (JINA'04)*, Nice, France, November 8–11, 2004, pp. 140-141.

4. K. Blagović, I. Stevanović, and A. K. Skrivervik, "Convergence of infinite periodic Green's functions for the mixed potential integral equation," in *Proc. 17th International Conference of Applied Electromagnetics and Communications, ICECom 2003*, Dubrovnik, Croatia, Oct. 1–3, 2003, pp. 423–426.

5. S. Skokić, Z. Sipus, K. Blagović, J. Bartolić, "Nondestructive Method for Measuring Complex Permittivity of Lossy Media," *Proceedings of the SoftCOM 2001, Vol. I*, Split-Bari-Dubrovnik, Croatia, Croatia, September. 12–16, 2001, pp. 263-270.